Universitat de València

DEPARTAMENTO DE FÍSICA ATÓMICA
MOLECULAR Y NUCLEAR

UNIVERSITAT DE VALÈNCIA

Characterization of two Photomultiplier Models and Study by Monte Carlo Simulation of several Calibration Systems based on Optical Beacons for the ANTARES Detector

TRABAJO DE INVESTIGACIÓN

JUAN DE DIOS ZORNOZA GÓMEZ

MARCH 2001

D. JUAN JOSÉ HERNÁNDEZ REY, Científico Titular del C.S.I.C.,
D. JUAN ZÚÑIGA ROMÁN, Profesor Titular de la Universidad de Valencia

CERTIFICAN :

Que la presente memoria "Characterization of two Photomultiplier Models and Study by Monte Carlo Simulation of several Calibration Systems based on Optical Beacons for the ANTARES Detector" ha sido realizada bajo nuestra dirección en el Departamento de Física Atómica, Molecular y Nuclear de la Universidad de Valencia por D. Juan de Dios Zornoza Gómez y constituye su Trabajo de Investigación del Tercer Ciclo que sigue en este Departamento para optar al grado de Doctor en Física.

Y para que conste, en cumplimiento de la legislación vigente, firmamos el presente Certificado en Burjassot a 13 de Marzo de 2001.

Juan José Hernández Rey   Juan Zúñiga Román

A mi familia

Agradecimientos

Mucha gente me ha ayudado de muy diversas maneras para que este trabajo sea una realidad. A través de estas líneas quiero expresarles mi sincero agradecimiento, aunque en algunos casos no basta con unas pocas palabras para condensar mi gratitud.

En primer lugar, quiero agradecer a D. Juan José Hernández la confianza que siempre ha depositado en mí. Nunca le faltará mi reconocimento a su apoyo en todo momento. Ha sido una fuente inagotable de buenos consejos y mucho es lo que he podido aprender de él.

Quiero también manifestar mi agradecimiento a D. Antonio Ferrer, quien me abrió la puerta a la investigación.

Agradecer la inestimable ayuda de Juan Zúñiga, que siempre ha estado dispuesto a orientarme. Su experiencia con la simulación Monte Carlo ha sido imprescindible. Además, sus atinados consejos han aumentado mucho el valor de este trabajo.

Agradecer a Emiliano los sólidos cimientos que su labor previa han supuesto para mi trabajo. Es un compañero excepcional a quien le debo gran parte de lo que he aprendido aquí. Su paciencia para escuchar mis preguntas ha sido incansable y sus conocimientos para responderlas, extraordinariamente profundos.

A Sergio deseo agradecerle su valiosísima ayuda con la simulación. Aprender una parte de su extensa experiencia ha hecho accesibles los problemas más complejos. Además, su entusiasmo y su carácter son para mí un ejemplo muy preciado.

También a Víctor, Gaëlle y Ramón quiero dar las gracias por colaborar siempre conmigo. Con ello, además de su ayuda, me han dado la satisfacción de poder trabajar en un ambiente inmejorable.

Quiero agradecer a Hervé Lafoux, Vincent Bertin y Stephane Basa el haber estado siempre dispuestos a aclararme las dudas que les he consultado.

A Víctor Olmos me gustaría manifestarle mi gratitud por la oportunidad que me brindó para iniciarme como científico. Aprendí mucho de su carácter generoso y valiente.

A Andrés, Rosario, Javier, Amparo, Manolo y Paco les agradezco la ayuda que me han prestado siempre que los he necesitado.

Quiero agradecer a Arantza y a Pablo haber compartido su casa conmigo cuando he estado en el CERN. Han sido unos perfectos anfitriones.

Agradecer también a César, Jose, Djalil, Jose Enrique, Paco, Santi, Juanba y toda la gente con la que he compartido no sólo el lugar de trabajo, sino también su amistad.

Finalmente, quiero agradecer muy especialmente a Ana y a su familia su cariño y apoyo. Sin ellos, estos años hubieran sido mucho más duros. Siempre estaré en deuda con ellos por haberme acogido, por tener una confianza absoluta en mí y por quererme como a uno más de su familia.

Contents

Introduction

Neutrinos are expected to be a new powerful tool to survey the sky in a complementary way to photons and cosmic rays, which have been up to now the only cosmic messengers used.

Neutrinos can help us to understand many open topics such as the ultra energetic cosmic rays, the gamma ray bursts or the nature and origin of dark matter.

Most of the knowledge we have about the Universe comes from photons, since they can be detected easily in a wide range of energies and are copiously produced. There are, however, limitations to the information that we can obtain from them. Because of their interaction at high energies with matter, the infrared radiation and the microwave background, high energy gamma rays produced in very dense or very far away sources will not reach us. Photons with energy $E > 10$ TeV coming from sources farther than 100 Mpc away are likely to be unobservable.

On the other hand, magnetic fields deflect charged cosmic rays, spoiling any directional information and hindering the knowledge of their source. Only protons above 10^{20} eV are energetic enough to travel straight, but the fluxes at these energies are very low.

Neutrons could be a good probe, since they are electrically neutral. However, they have a short lifetime and therefore cannot be used to study distant objects. Even at very high energies ($> EeV$) they cannot travel more than 10 kpc, i.e. roughly the radius of our Galaxy.

On the contrary, neutrinos are stable and interact weakly, so that they can escape from very dense regions and travel long distances. They are therefore a unique candidate to study the Universe in the high energy domain. Nevertheless, their advantage is also their main drawback: the detection of neutrinos is a very difficult task that implies the use of very large detectors.

The best option is probably the use of underwater/ice telescopes, proposed by Markov in 1960 [1]. The detection principle is based on the Cherenkov emission from the muon produced after a charged current interaction of the neutrino with the matter surrounding the detector. Given the low νN interaction cross-sections and the expected neutrino fluxes the natural size of these detectors is of the order of $\sim$km^2.

The ANTARES collaboration aims to show the feasibility of the detection of high energy neutrinos with an underwater telescope in the Mediterranean sea [2]. This project, which includes astronomers, oceanographers and particle physicists from France, Spain, the United Kingdom, the Netherlands, Russia and Italy, has started the construction of a 0.1 km^2 detector which will be completely deployed in 2004.

One of the crucial preliminary tasks in the experiment is the study and selection of the photomultipliers that will be used for the detection of the Cherenkov light. Due to the nature of the experiment, the photomultipliers must have a very large photocathode area and very good timing properties. The first part of this work deals with the study and the results of the tests performed in Valencia on two possible candidate photomultipliers. This study continues and completes the work done at IFIC on this subject during the last years and whose results were presented elsewhere [3].

The second part of this work concerns the results obtained in the simulation of several schemes for the *in situ* time calibration system of the detector using external light sources. The muon track reconstruction efficiency and the angular resolution of the experiment will strongly depend on the time resolution of the detector. The knowledge of the relative time offsets between the different optical modules will therefore be of paramount importance in the performance of the detector. These offsets can be estimated using artificial sources installed in the detector that can emit well-controlled short light pulses. Several configurations with different light sources at different locations have been simulated in this work and the results compared in order to asses the advantages and drawbacks of each configuration.

This report has the following structure. The experiment is explained in the first chapter. It includes an introduction to the scientific motivations and a description of the ANTARES detector.

The general characteristics of the photomultipliers and the experimental setup are described in the second chapter. The results of the tests performed are presented in the third chapter. Their most relevant parameters have been measured: gain, peak to valley ratio, energy resolution, transit time spread, dark noise and afterpulse rate.

The fourth and fifth chapters are devoted to the timing calibration with optical beacons. First, the aims and the features of the simulation are presented. The influence of the water optical properties are commented in detail. In the last chapter the results are analyzed. Several configurations have been studied: LED cylinders along the strings, individual LEDs in each optical module and a laser at the bottom of an external instrumentation line.

Finally, the main conclusions of this work are summarized.

Chapter 1

High energy neutrino astronomy with the ANTARES detector

In this chapter, an introduction to the ANTARES detector is made. After explaining the motivations for such an experiment, the main expected high energy neutrino sources are presented. As it will be seen, there are mainly three interesting research topics in ANTARES: astrophysics, neutrino oscillations and dark matter. Finally, the detection principle and the telescope are described.

1.1 Scientific motivations

1.1.1 Cosmic rays

Cosmic rays are charged particles that arrive to the Earth from the sky. They are composed of protons and heavy nuclei. Their fluxes and energies are an indirect hint of the existence of high energy neutrino sources.

As it can be seen in Figure 1.1 the cosmic ray spectrum follows a power-law behaviour:

$$dI = kE^{-\gamma}dE \tag{1.1}$$

The slope of this spectrum changes at two points: at $E_{primary} \simeq 4 \times 10^{15}$ eV (*knee*) and at 10^{19} eV (*ankle*). The power-law index up to the knee is $\gamma = 2.7$. Then, the slope of the spectrum becomes steeper: $\gamma = 3.1$ and after the ankle, is almost flat.

It is believed that cosmic rays up to the knee can be explained by diffusive shock acceleration mechanisms [5, 6]. Particles of the interstellar medium can gain energy from the expanding shock wave produced in supernovae explosions (first order Fermi mechanism). The standard model of this acceleration mechanism predicts a spectrum close to $E^{-2.1}$, which is flatter than the observed data. However, an analysis of the abundance of fragmentation nuclei indicate that the lifetime varies as $E^{-0.6}$. This would explain the observed value $\gamma = 2.7$. However, the maximum energy reached in the shocks produced by supernovae is predicted to be $Z \times 10^{14}$ eV. Some additional mechanisms such X-ray binaries have been proposed to explain the rest of the spectrum.

Both Fly's Eye (atmospheric fluorescence detector) and AGASA (air shower array) have shown that cosmic rays with energies larger than $5{\times}10^{19}$ eV exist [7,8], as it is shown in Figure 1.1. These ultra-high energy cosmic rays are expected to interact with the microwave background (Greisen-Zatsepin-Kuz'min (GZK) cutoff [9, 10]) and therefore cannot travel long distances. However, the

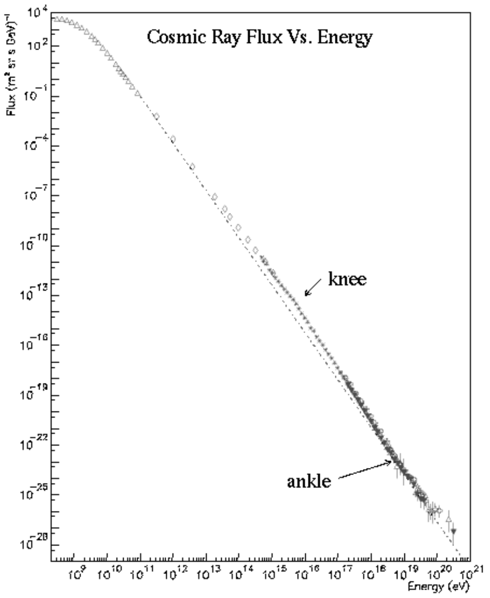

Figure 1.1: Cosmic ray spectrum [4]. Both knee and ankle positions are indicated.

angular distribution of these cosmic rays is isotropic, which would indicate an extra galactic origin. Possible explanations are discussed in Section 1.2.

1.1.2 High energy photons

Experimental results [11–13] evidence the existence of high energy photons. They are expected to be produced by non hadronic mechanisms (synchrotron radiation, bremsstrahlung and Compton inverse scattering). However, high energy photons can also be generated by means of the strong interaction of charged particles with matter. The subsequent neutral pions will decay to photons. In this case, neutrino production has to occur, from the charged pion disintegration.

If photons with energies larger than 100 TeV exist, they can only be explained by the hadronic mechanism. However, as in the case of the cosmic rays, it is not possible to detect them because of the GZK effect which supresses any possibility of exploring the Universe over distances greater than 100 Mpc with high energy ($>$ 10 TeV) gamma rays. This could explain why the only two extragalactic sources discovered at the level of $\sim$ TeVs are Markarian 421 and Markarian 501 [14,15], which are at 125 Mpc and 135 Mpc respectively. Other stronger sources could emit photons with higher energy but they are too far so that we can detect them [16]. However, we could detect the high energy neutrinos also produced there.

1.2 High energy neutrino sources

There are several mechanisms which are expected to produce measurable neutrino fluxes. The main candidates are described in this section. As it is explained here, many interesting fields can be studied by means of the ANTARES telescope: astrophysical objects (AGNs, supernova remnants, GRBs, etc.), neutrino oscillations, neutralinos, monopoles ...

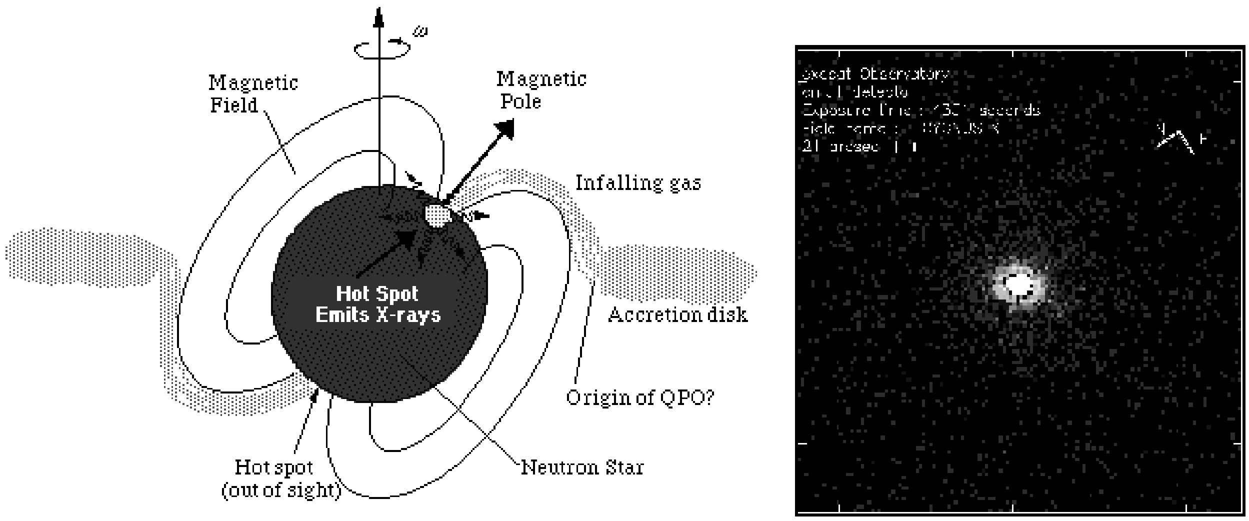

Figure 1.2: Left: Scheme of X-ray binary with a neutron star. Right: X-ray image of the black hole candidate Cignus X-1, obtained by the Chandra telescope.

1.2.1 Astrophysical sources

Astrophysical sources are expected to be the main mechanism to produce high energy neutrinos. The leptonic decay of mesons produced in the interaction of protons with matter or radiation can generate these neutrinos. In this subsection, the most interesting astrophysical objects from the ANTARES point of view are presented.

- **X-ray binaries**
  A X-ray binary is a stellar system composed of a compact object (neutron star or black hole) and a non-compact star (Figure 1.2). Matter is accreted to the compact object from its companion. This process gives rise to stochastic acceleration of protons. Moreover, the strong magnetic field present in many neutron star is another effective acceleration mechanism. These high energy protons interact with the accreting matter and neutrinos are produced.

- **Supernova remnants**
  High neutrino fluxes can be produced after a supernova explosion (Figure 1.3). The expanding shell of material accelerates high energy particles (Fermi mechanism). Since in many cases, a neutron star is formed after this explosion, there would be an additional accelerating mechanism due to its strong magnetic field [17]. In particular, the ion doped wind model predicts a high neutrino flux. According to this model, ions drift along the magnetic field of the neutron star with speed 10 times larger than the hydrodynamic expansion velocity. The subsequent interaction produces pions which give rise to neutrinos. However, these events have to occur nearby to be detectable, and this is not likely.

- **Active galactic nuclei**
  The standard model to explain active galactic nuclei (AGN) is a galaxy with a massive black hole (10^6-10^9 solar masses) to which matter is accreted at a rate of at least a few solar masses per year (Figure 1.4). This would explain the high emission power observed in these objects (10^{35}-10^{41} W). In some AGNs, two axial relativistic jets are produced. These jets

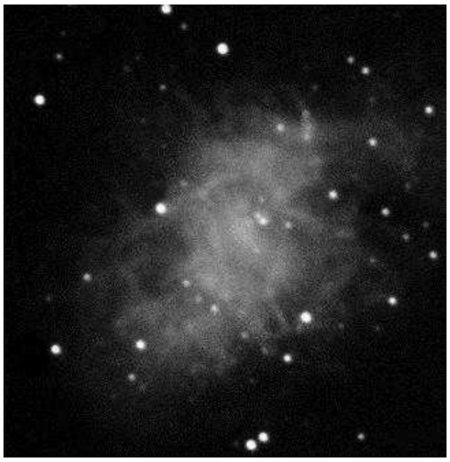

Figure 1.3: Supernova remnant: Crab Nebula, from National Optical Astronomy Observatories.

are observable by the radio component coming from the synchrotron emitting electrons up to 1 Mpc distances. Blazars are supposed to be AGNs whose jets are pointing towards us, so its observed emission, boosted by Doppler effect, is higher. The jet production mechanism is under debate. An important high energy neutrino flux is expected from the acceleration of protons in the inner regions of the jets [18]. Neutrino production is also expected from the accreting disk [19]. Up to now, experimental results from EGRET [11] and atmospheric detectors have shown that many blazars emit γ rays with energies up to 10^{10} eV and 10^{12} eV, respectively, which confirm them as candidates to high energy neutrino sources.

- **Gamma ray bursts**
  Gamma ray bursts are one of the phenomena in which there is most scientific interest nowadays. They are the most violent events ever detected. After a spectacular explosion, an afterglow can be observed (Figure 1.5). The duration of the explosion is very short, only few seconds, but the γ emission is of the order of 10^{51}-10^{54} erg if the explosion is assumed to be isotropic. If the explosion is beamed, as recent observations suggest, this energy has to be lowered by a factor of several hundred. The two main models proposed to explain them are the so called *fireball* [21] and *cannonball* [22] models. In the first case, the energy is produced in the formation of a black hole from a binary system or two neutron stars. As result, a solar mass of energy concentrates in a 100 km region. A fireball expands ultra-relativistically with a Lorenz factor $\gamma > 300$ and the subsequent internal shocks between the expanding shells produce the GRB. On the other hand, the cannonball model assumes that after a supernova explosion, a fraction of the parent star falls back and produce a thick accretion disk. The consequence is that relativistic cannonballs are ejected and collide with the external shell produced in the SN explosion. In both cases, an hadronic component is expected, but the predicted fluxes ($\sim$20/km^2/year in 4π) are low for ANTARES. However, a higher event rate can be obtained by lowering the energy threshold to $\sim$100 GeV and requiring a spatial and temporal coincidence.

- **Relic sources**
  A solution to explain the violation of the GZK cutoff, mentioned in Section 1.1 could be topological defects formed in the early Universe [23]. They would decay to massive gauge

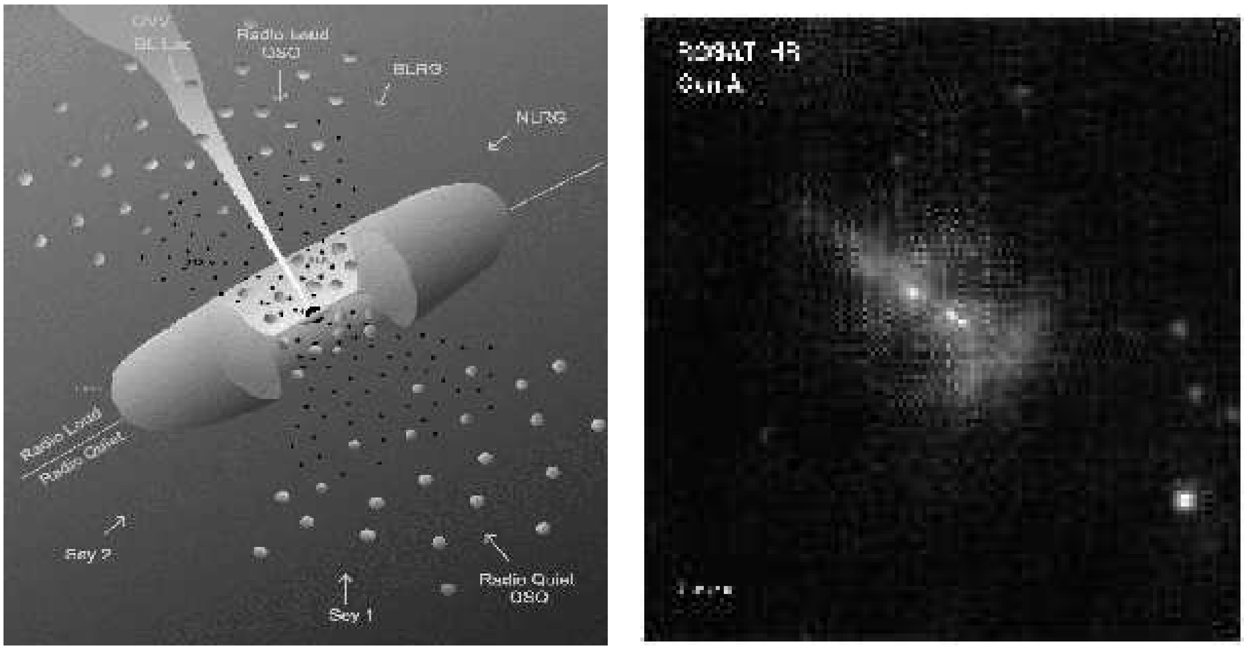

Figure 1.4: Left: Scheme of AGN [20]. Right: Active galactic nucleus Centaurus A (NGC5128), obtained by ROSAT satellite.

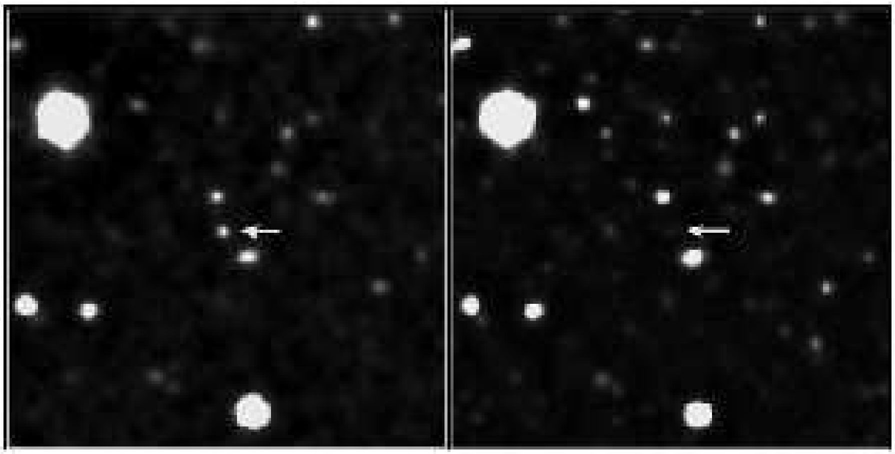

Figure 1.5: Images of the GRB 971214 field, obtained with the W.M. Keck 10-meter telescope. The image on the left shows the visible-light afterglow of the burst (marked with an arrow), obtained about two days after the burst, while it was still relatively bright. The image on the right shows the same field as seen about two months later, after the burst afterglow has faded away, revealing a faint galaxy at its position (also marked with an arrow).

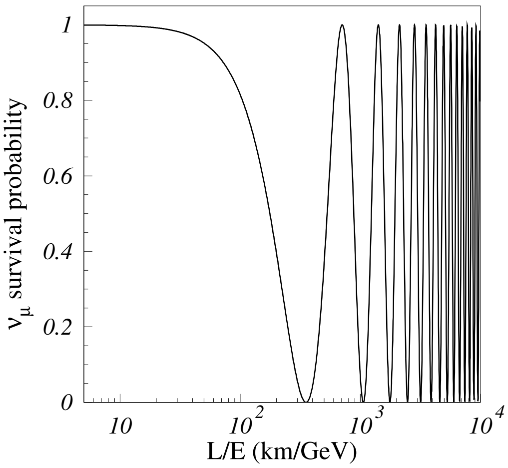

Figure 1.6: Variation of the neutrino survival probability as a function of L/E for $\Delta m^2 = 3.5 \times 10^{-3}$ eV^2 and maximal mixing.

and Higgs bosons with masses $\sim 10^{25}$ eV. Subsequent decays would produce high energy protons, γ-rays and neutrinos. It has also been suggested the ultra-energetic cosmic rays could be produced in the decays of metastable relics with masses larger than $\sim 10^{21}$ eV. These particles, created in the re-heating following inflation, would be a fraction of the cold dark matter and would be clustered in the Galactic halo. The energy in the cascade is mostly converted into neutrinos and these should be well correlated in both time and arrival direction with the ultra-high energy cosmic rays. The crucial point is that whatever is the process which produces the ultra-energy cosmic rays, an important production of very high energy neutrinos is expected.

1.2.2 Neutrino oscillations

Neutrino oscillation can also be studied with the ANTARES detector. An oscillation mechanism has been proposed in order to explain the observed deficit [24,25], in the number of muon neutrinos with respect to electron neutrinos in the atmospheric neutrino flux.

In the hypothesis of two-neutrino mixing, the oscillation probability is given by:

$$P = \sin^2 2\theta \sin^2 \left(1.27\frac{L}{E}\Delta m^2\right) \tag{1.2}$$

where θ is the mixing angle, L is the distance travelled by the neutrino (in km), E is the neutrino energy (in GeV) and Δm^2 is the difference of the square masses (in eV^2). From the analysis of the Super-Kamiokande collaboration [26], the most probable result is $\Delta m^2 = 3.5 \times 10^{-3}$ eV^2 and $\sin^2 2\theta = 1.0$. With these values, the survival probability 1–P vanishes for $L/E = (2n+1) \times$ 353 kmGeV^{-1}, where n is a non negative integer. Figure 1.6 shows these survival probability for the previously mentioned Δm^2 and $\sin^2 2\theta = 1.0$ values.

ANTARES could be a useful tool on this topic since it could have an optimal sensitivity to detect the first survival probability minimum in the most probable region claimed by Super-Kamiokande.

Tau neutrinos are also an interesting point to study by ANTARES. Its contribution to the atmospheric neutrino flux is negligible, but they have to be taken into account when studying oscillations [27]. If the oscillation $\nu_\mu \rightarrow \nu_\tau$ exists, it will produce τ leptons and their subsequent decay $\tau^- \rightarrow \mu^- \bar{\nu}_\mu \nu_\tau$ will be a contribution to the physical background.

On the other hand, tau neutrinos can be detected as signal (not background) at very high energy. The Earth is almost transparent to low energy neutrinos, but opaque to neutrinos above 100 TeV. However, tau neutrinos with energy larger than several hundreds of TeV can produce tau leptons before being absorbed and these will decay to ν_τ of lower energy, which are not so strongly absorbed. This flux would be constant during the Earth's rotation, whereas the flux of ν_μ would vary with the day because of the change in elevation seen by ANTARES.

1.2.3 Neutralino detection

There are many evidences which support the existence of dark matter in the Universe. Luminous matter can account only for a small fraction of the density of the Universe, so several candidates have been proposed. Since the density of baryonic matter is constrained by the abundance of the light elements to be a small contribution to the dark matter, the non baryonic alternative is a key point to understand this fundamental cosmological issue.

One of the most relevant candidates to the non baryonic dark matter is the Light Supersymmetric Particle (LSP) of the supersymmetric models. The main hypothesis of Supersymmetry is assumed to be a spontaneuously broken symmetry between bosons and fermions. The minimal supersymmetric model (MSSM) assumes a boson partner for every fermion, a fermionic partner for every boson and two Higgs doublets. It is also assumed that the so-called R-parity is conserved (R=+1 for ordinary particles and -1 for their supersymmetric partners). A consequence of this is that the lightest supersymmetric particle is stable. Although the experimental results constrain the identity of the LSP, it is still ambiguous. However, it is generally supposed that the LSP is the lightest neutralino.

These neutralinos would accumulate in the core of the Earth on the Sun and in the center of the Galaxy [28, 29]. This accumulation is produced by the scattering of the neutralinos when crossing these celestial bodies. If the speed becomes lower than the escape velocity, the neutralinos will remain there. These neutralinos will annihilate into a fermion-antifermion pair or into various two bodies combinatinations of W, Z and Higgs bosons. The decays to c, b and t quarks, τ leptons, Z, W and Higgs bosons can produce a significant flux of high energy neutrinos.

Detection of these neutrinos would provide important information about neutralino couplings and MSSM parameters.

1.2.4 Other exotic sources

- **GUT monopoles**
  Massive magnetic monopoles would be produced, according to the Grand Unified Theories (GUT) of the electroweak and strong interactions, after the Big Bang and they would be slowed down to velocities $\beta \leq 10^{-3}$. One of the points that makes interesting its existence is that they could produce baryon number violation.

  ANTARES could study this phenomena by the sequential Cherenkov flashes along the track of the slow monopole.

- **relativistic monopoles**
  The ultra high energy cosmic rays mentioned in the previous sections could be relativistic monopoles. With a trigger based on the slow monopole velocity, they can be distinguished from the PeV muons, whose signal is similar in energy.

- **SUSY Q-balls**
  Q-balls are another canditate to dark matter. These non-topological solitons are predicted by Supersymmetry and their signal in the detector depends on the parameters of the theory. For large baryon number ($\sim 10^{24}$) spectacular emissions of energy around 10 GeV/mm are expected.

- **New phenomena**
  In addition to the predicted phenomena discussed above, neutrino telescopes will provide an opportunity to see new Physics which has not been anticipated. ANTARES is a pioneer experiment which will try to open a new window to the Universe.

1.3 The ANTARES detector

In this section the ANTARES detector is described. First, the detection principle is explained and the expected fluxes from the sources mentioned in the previous section are given. Then, a technical description of the detector and its expected performance are presented.

1.3.1 Detection principle

The detection principle on which ANTARES is based was proposed by Markov in 1960 [1]. With a detector in the sea bed (to avoid atmospheric downgoing muons), the neutrino is detected through the Cherenkov light emitted by the muon produced in the charged current reaction:

$$\nu_\mu(\bar{\nu}_\mu) + N \longrightarrow \mu^-(\mu^+) + X \tag{1.3}$$

In principle, not only muonic neutrinos will be useful for neutrino astronomy. Also electronic and tau neutrinos give rise to leptons which emit Cherenkov light. However, the electromagnetic shower produced by electronic neutrinos are too small compared with the whole detector volume, so angular resolution will be poor. On the other hand, only low tau neutrino rates are expected.

Most of the muonic neutrinos pass through the Earth without interacting. However, a small probability of weak interaction exists and muon is produced, as it is shown in Equation 1.3. This muon can go across several kilometers of matter before stopping.

The deep inelastic charged current cross-section for $\nu_l + N \to l^- + X$ is given by [30]:

$$\frac{d^2\sigma_{\nu N}}{dxdy} = \frac{2G_F^2 m_N E\nu}{\pi} \frac{M_W^4}{(Q^2 + M_W^2)^2} \left[xq(x,Q^2) + x(1-y)^2\bar{q}(x,Q^2)\right] \tag{1.4}$$

where G_F is the Fermi constant, m_N and M_W are the nucleon and W-boson masses, and Q^2 is the square of the momentum transfer between the neutrino and the muon. The Bjorken variables are $x = Q^2/2m_N\nu$ and $y = (E_\nu - E_l)/E_\nu$, where $\nu = E_\nu - E_l$ is the lepton energy loss in the laboratory frame and q and $\bar{q}$ are the nucleon structure functions.

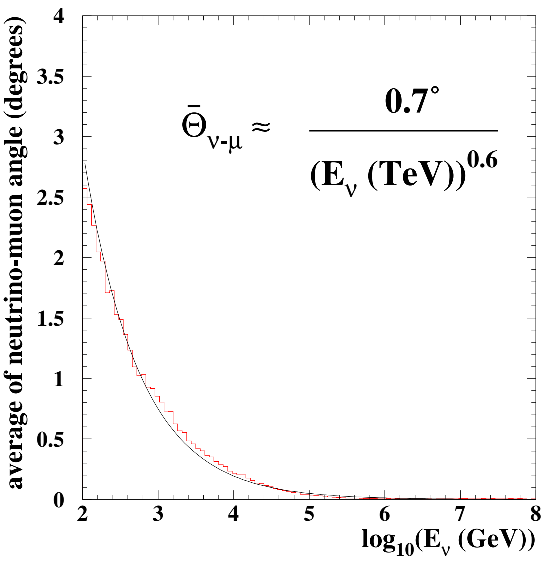

Figure 1.7: Angular difference between the initial neutrino direction and that of the muon track at the detector; the functional form shown reproduces the observed energy dependence well (solid curve).

At low energies ($E_\nu << M_W^2/2m_N \approx 5$ TeV), the cross-section grows linearly with the neutrino energy [2].

$$\sigma_{\nu N}(E_\nu) \simeq 0.67 \times 10^{-38} E_\nu(GeV) \quad cm^2 \tag{1.5}$$
$$\sigma_{\bar{\nu} N}(E_\nu) \simeq 0.34 \times 10^{-38} E_\nu(GeV) \quad cm^2 \tag{1.6}$$

At lower energies ($E < 100\ GeV$), the cross section is essentially constant with energy.

At high energies ($E_\nu >> M_W^2/2m_N \approx 5$ TeV), the cross-section is dominated by the behaviour of structure functions at small x.

The dependence of the angle between the incident neutrino and the outgoing muon on the neutrino energy can be parametrized according to the formula [2]:

$$\bar{\theta}_{\nu-\mu} \approx \frac{0.7^\circ}{(E_\nu(TeV))^{0.6}} \tag{1.7}$$

As it can be seen in Figure 1.7, this angle is small for high energies.

The muon energy loss in the medium can be approximated by the expression:

$$-\frac{dE}{dx} = a_{ion} + (b_{brems} + b_{pairs} + b_{n.r.})E \tag{1.8}$$

There are four different causes for this loss. On one hand, the ionization, which is a constant for energies above 1 GeV. On the other hand, bremsstrahlung, pair production and nuclear reactions grow linearly with muon energy.

As it has been mentioned, the muon track is detected by means of the Cherenkov emission. This occurs when a charged particle passes through a medium with velocity exceeding the speed of light in the medium. The angle of the cone in which the light is emitted depends on the particle velocity β and the refractive index of the medium n:

$$\cos\theta_C = \frac{c/n}{\beta c} = \frac{1}{\beta n} \tag{1.9}$$

In the case of typical events in ANTARES ($E < 10$ GeV), particles will be relativistic (β=1) so the Cherenkov angle, assuming n=1.35 for λ=450 nm, is $\theta_C \simeq 43°$.

The number of photons produced along a flight path dx in a wavelength bin $d\lambda$ for a particle carrying unit charge is:

$$\frac{d^2N}{dx d\lambda} = \frac{2\pi}{137\lambda^2}\left(1 - \frac{1}{n^2\beta^2}\right) \tag{1.10}$$

In principle, a high contribution of short wavelengths is expected from the dependence on $1/\lambda^2$. However, attenuation suppresses part of this contribution. The maximum in the water transparency is for $\lambda \sim$470 nm and this also matches the maximum in the photomultiplier efficiency.

1.3.2 Expected fluxes

In Section 1.2 a general overview of the high energy neutrino sources was presented. The expected flux produced by these sources depends on the model. Figure 1.8 shows the diffuse flux predicted by several models.

As it can be seen in the previous figure, at low energies the atmospheric neutrinos dominate. These atmospheric neutrinos are produced in reactions due to the cosmic rays:

$$\begin{array}{lll} p \longrightarrow \pi^+(+K^+\cdots) \longrightarrow & \mu^+ + \nu_\mu \\ & \downarrow \\ & e^+ + \bar{\nu}_\mu + \nu_e \\ \\ n \longrightarrow \pi^-(+K^-\cdots) \longrightarrow & \mu^- + \bar{\nu}_\mu \\ & \downarrow \\ & e^- + \nu_\mu + \bar{\nu}_e \end{array} \tag{1.11}$$

There is also another component of the physical background in these kind of telescopes. It can also be seen in the previous reactions: the downgoing muons induced by atmospheric cascades, which are interpreted as upgoing.

Atmospheric neutrinos are an irreductible background because they cannot be distinguished from extraterrestrial neutrinos. At high energies, this background is lower than the expected flux produced by the sources we are interested in.

In the case of atmospheric muons, there is a strong dependence on the zenithal angle, as it can be seen in Figure 1.9. There is a high flux of down-going muons, but the flux of up-going atmospheric muons is negligible since they are absorbed in the Earth. Atmospheric muons are the reason to build the telescope in the sea bed.

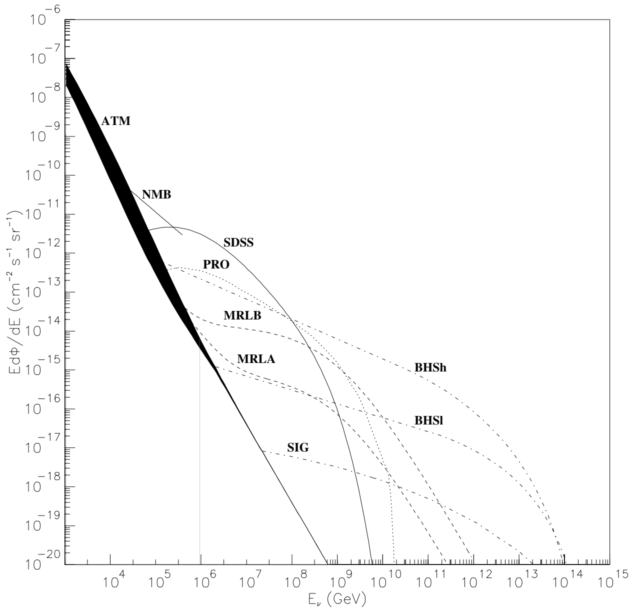

Figure 1.8: Neutrino fluxes as function of the neutrino energy for different models SDSS, NMB (continous lines), MRLA, MRLB (dashed line), PRO (dotted line), BHSI, BHSh and SIG (dashed-dotted lines). The fluxes have been multiplied by the neutrino energy.

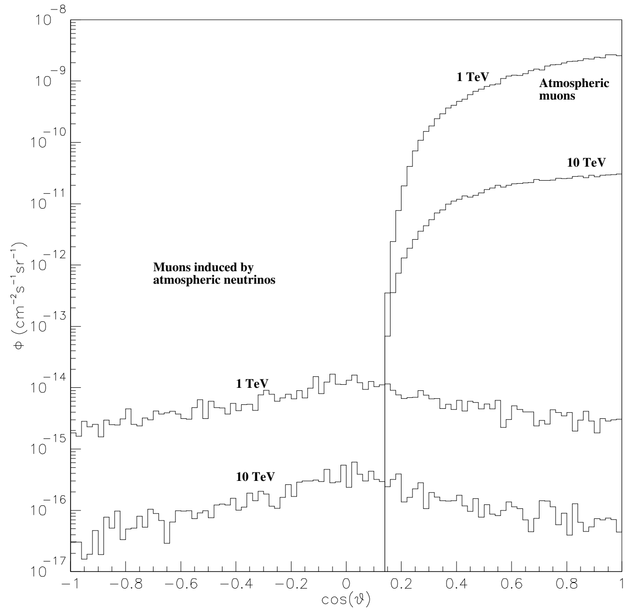

Figure 1.9: Atmospheric and neutrino induced muon flux dependence on the azimuthal angle.

Model	$E_{\mu}^{min} = 1$ TeV	10 TeV	100 TeV	1 PeV	10 PeV	100 PeV
Atmosf. [31]	12000	280	3.6	0.4	0.004	-
SDSS [32]	4200	2700	1100	180	12	0.2
NMB [33]	6300	1700	130	-	-	-
MRLA [34]	330	50	5	0.7	0.2	0.02
MRLB [34]	370	80	20	9	2.6	0.4
PRO [35]	510	360	180	50	4.5	0.5
BHSl [36]	3.8	2.6	1.4	0.6	0.2	0.05
BHSh [36]	700	340	135	42	10	2
SIG [37]	0.05	0.04	0.02	0.01	0.005	0.001

Table 1.1: Expected number of up-going induced muons per year and km^2 predicted by several models.

Table 1.1 shows the expected number of up-going induced muons according to several models. It can be seen that the rates for cosmic neutrinos decrease with increasing energy threshold more slowly than the rate for atmospheric neutrinos.

1.3.3 Detector description

The ANTARES collaboration aims to prove the feasibility of an undersea neutrino telescope. Extensive studies concerning critical points of the experiment (water optical properties, biofouling, bioluminiscence, etc.) have been performed. The first stage of the experiment is to build a 0.1 km^2 detector. After completing this first stage, the next step will be to build a neutrino telescope with volume 1 km^3.

1.3.3.1 Geometry

The 0.1 km^2 detector will be a tridimensional array of photomultipliers to detect the Cherenkov emission of the muons. The photomultipliers will be installed on flexible strings or lines and their signal will be sent to a junction box on the sea bed. This junction box will be linked by an electro-optical cable to a shore base where the data are recorded. This detector will have $\sim$1000 photomupliers located on 13 strings. Figure 1.10 shows a general overview of the detector.

Several criteria have to be taken into account to optimize the geometry of the detector. The specifications to study each of the three main parts of the scientific program are different [38]. The threshold to observe astronomical sources above the background of the atmospheric neutrinos is $\sim$1 TeV. The threshold for neutralino search is $\sim$25 GeV. Finally, the study of neutrino oscillations needs a threshold which depends on the value of Δm^2, but which is expected to be $\sim$10 GeV. The detector geometry has been optimized for the energy range 100 GeV-10 TeV. Smaller spacing

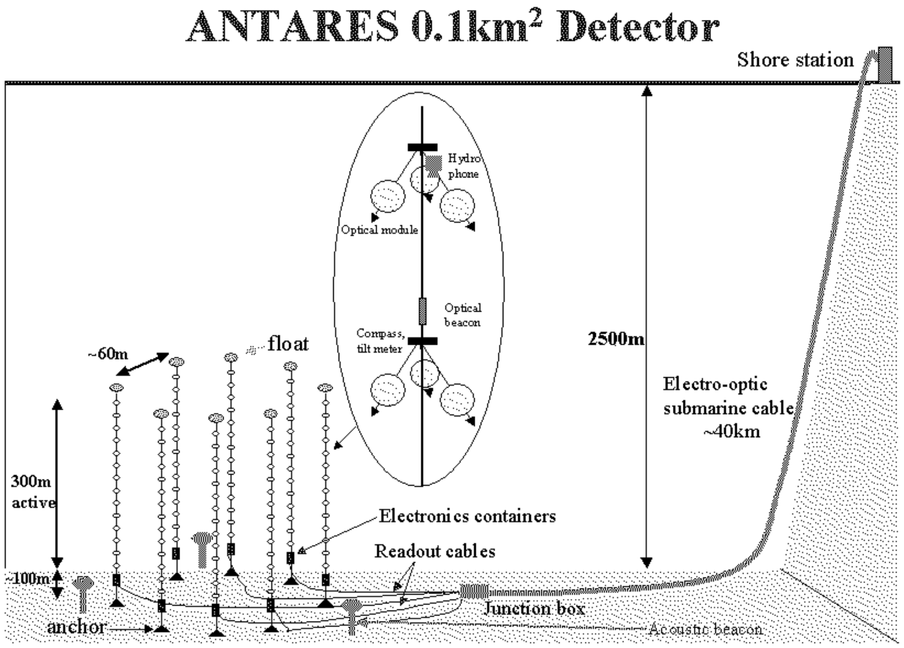

Figure 1.10: General overview of the detector.

between lines means to lower the energy threshold whereas greater spacing would be appropriate for a detector optimized to higher energies.

1.3.3.2 Detector elements

The photomultipliers (PMT) will be housed in a pressure-resistant sphere, which can withstand pressures up to 700 bars. Apart from the photomultiplier, there are also other elements inside the pressure-resistant sphere. First, the electronics associated with the PMT: a high voltage converter and the electronic circuit (ARS) to read the signal from the PMT. Secondly, a silicone gel ensures optical coupling (n_{gel}=1.40, n_{glass}=1.48, n_{water}=1.35). An internal LED will also be included to measure the transit time of every PMT. Finally, a μ-metal cage will shield the phomultiplier against the Earth magnetic field. A non-uniformity lower than 5 % is expected. The sphere and its components form the so-called Optical Module (OM) (see Figure 1.11).

Three Optical Modules are grouped together in a storey with the axis of the photomultipliers pointing 45° below the horizontal, as it is shown in Figure 1.12 (left). In every storey, there is an electronics container, the Local Control Module (LCM).

Each string contains 30 storeys, with a vertical distance of 12 m among them. The active part of the string starts 100 m above the sea bed to avoid sea dust. A buoy at the top will keep the string vertical. Therefore, the total length of each line is ~400 m. Figure 1.12 (right) shows a scheme of a string.

Due to sea streams, the strings are expected to oscillate. In order to measure the position of the OMs with an accuracy $\sigma < 20$ cm, tiltmeters, compass and hidrophones are included in each string. Moreover, four acoustic beacons will be on the sea bed, surrounding the detector.

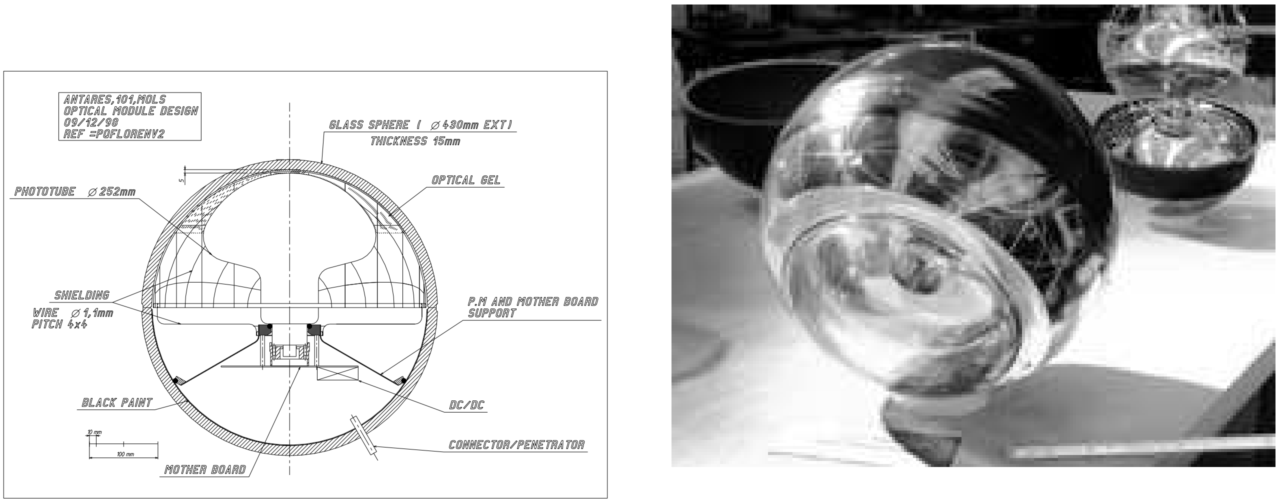

Figure 1.11: Left: schematic view of the Optical Module. Right: picture of the pressure-resistant sphere with all the elements which will be included.

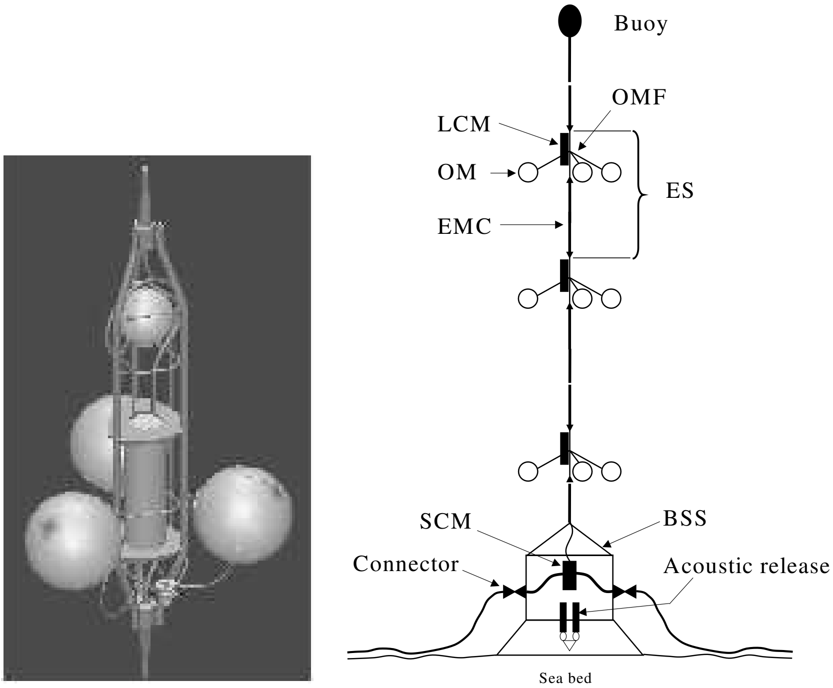

Figure 1.12: Left: scheme of a storey. Right: scheme of a string.

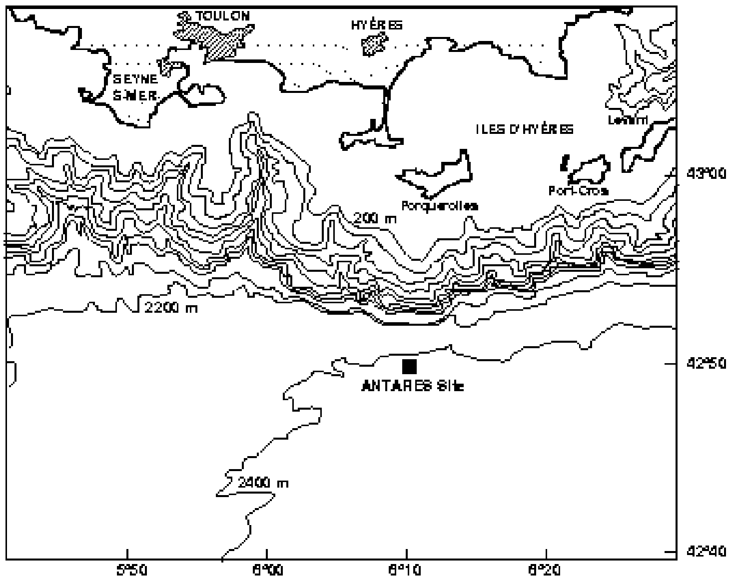

Figure 1.13: Map of the ANTARES site.

1.3.3.3 Trigger

There are two levels of off-shore trigger [38]. The L1 trigger is based on loose coincidences and large pulse heights within a storey. Only the ARSs for a PMT signal in the local storey will be read within a time window of 20 ns of the L1 trigger. The L2 trigger will require tighter conditions with a storey or between adjacent storeys on the same strings. When a L2 trigger occurs, all the ARSs in the detector will be read within a time window of ± 2 μs.

With this trigger system all the relevant data will be sent to shore, where more complex decisions can be made.

1.3.3.4 ANTARES site

1.3.3.5 Location

The detector will be located in the Mediterranean Sea (42°50'N, 6°10'E), on the French southern coast. Figure 1.13 shows a map with the location of the ANTARES site. This site is at a depth of 2400 m and 20 miles away from Toulon. The shore station will be located at La Seyne sur Mer.

In Figure 1.14 the area of the sky detectable form the ANTARES site is shown. The sources from the EGRET catalogue [11] which will be visible are also indicated.

1.3.3.6 Environmental parameters

Since 1996, many measurements of the environmental parameters of the ANTARES site have been made. This is a very important study since the performance of the detector depends critically on

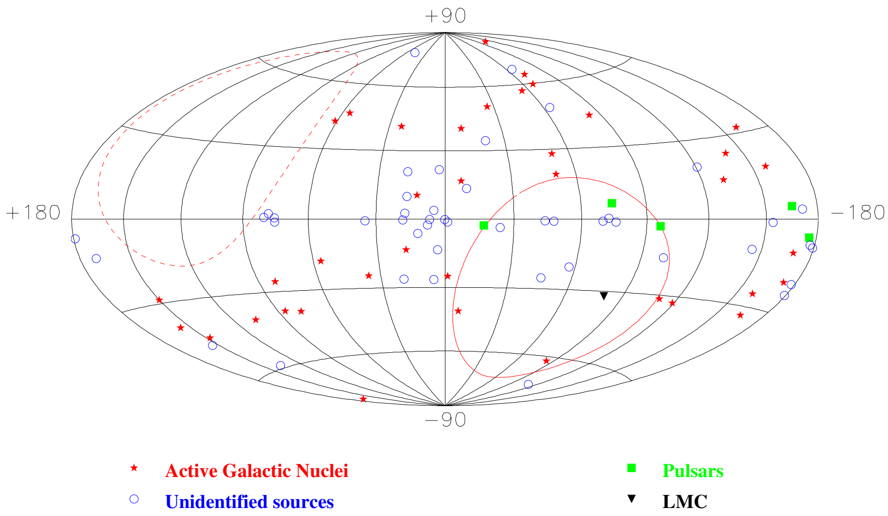

Figure 1.14: Visible sky region from ANTARES site. The area within the dashed line is not observable; the area within the solid line is observable 24 hours a day. Sources from the EGRET catalogue are also shown.

these parameters. Several autonomous lines have been deployed to carry out these studies.

- **Optical background**
  These measurements include the time dependence of the background as well as its spatial extent and its correlation to sea current.

  Figure 1.15 shows an example of counting rate as a function of time. There are two components: a low level background around 40 kHz and rapid ($\sim$ 1 s) flashes up to several MHz. The low level background varies between 17 kHz to 47 kHz over a time scale of hours. The disintegration of the ^{40}K isotope is the most likely cause of this background. Concerning the peaks, they are correlated with the current speed and are limited in spatial extend, so they are produced by bioluminiscence [39].

- **Biofouling and sedimentation**
  Biofouling is produced by bacteria sticked to the Optical Module surface. Although these bacteria are transparent, they make easier that sediments glue to the Optical Module.

  The results of the tests are presented in Figure 1.16. PIN diodes were located in different latitudes of the Optical Module. It can be seen that after 250 days, for horizontally-looking diodes the transmission loss is $\sim$2%, while for diodes looking 50° above the horizontal this loss is around 10% [40].

- **Optical properties of water**

  The setup to measure the attenuation length consisted of a rigid structure holding a collimated and continuous LED source located at a variable distance from an optical module (test 3). The LED luminosity is adjusted so as to obtain a constant current on the PMT. The value obtained is $\lambda_{att} = 41 \pm 1\ (stat) \pm 1_{syst}$ (see Figure 1.17).

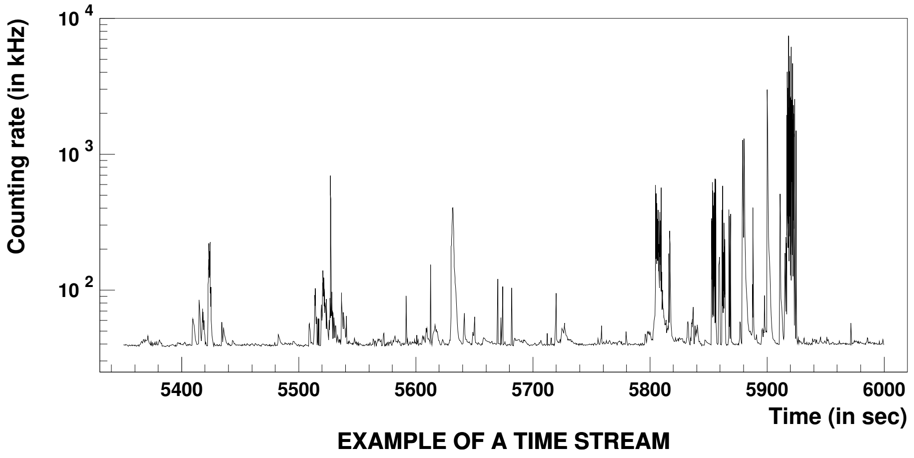

Figure 1.15: Time dependence on the counting rate.

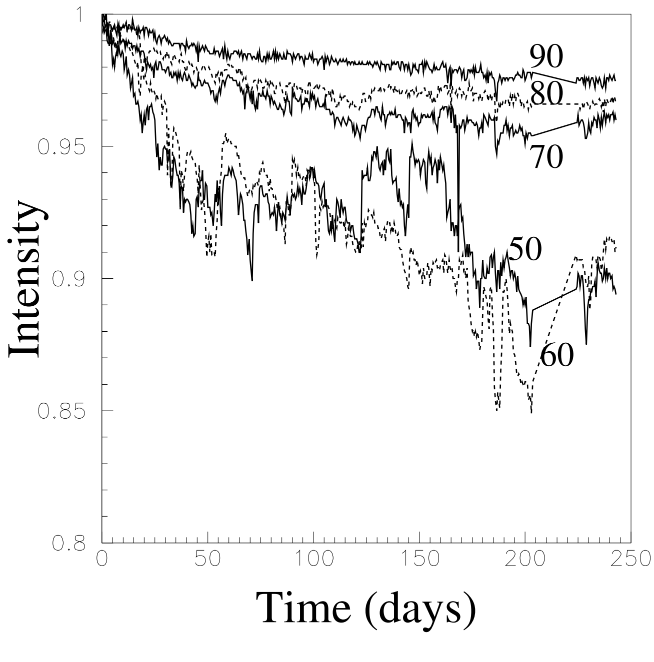

Figure 1.16: Transparency loss of a optical module for different polar angles.

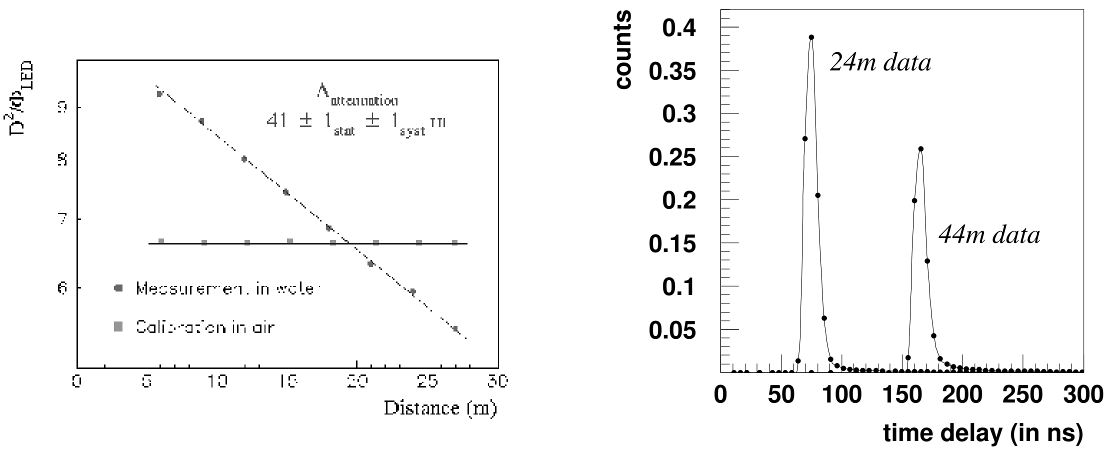

Figure 1.17: Left: Result of the measurement of the attenuation length. Right: Arrival time distributions of photons for two detector-source distances.

The attenuation length comes from both absorption and scattering, so complementary measurements were necessary to separate these contributions (test 3'). Arrival timing distributions from a pulsed isotropic LED source located at a distance of either 24 m or 44 m from a fast photomultiplier were obtained. The fit to this distribution allows to calculate the absorption length and effective scattering length:

$$\lambda_{eff} = \frac{\lambda_{scat}}{(1 - \langle \cos(\theta) \rangle)} \tag{1.12}$$

where λ_{scat} is the scattering length and $\langle \cos\theta \rangle$ is the average of the cosine of the scattering angle.

1.3.4 Performance of the detector

1.3.4.1 Angular Resolution

In order to do neutrino astronomy, a very good angular resolution has to be one of the main characteristics of the ANTARES telescope. For neutrino events with energy lower than 10 TeV, the angular resolution is dominated by the angle between the incident neutrino and the outgoing muon. Above 10 TeV, angular resolution is dominated by the timing resolution of the photomultipliers. To obtain an angular resolution of 0.2°, $\sigma_{PMT} \leq 1.3$ ns is required. If the timing resolution increases up to $\sigma = 2.0$ ns due to other contributions, the angular resolution degrades to 0.25°, which becomes 0.3° for a 10 TeV neutrino when the muon-neutrino kinematics is included. Other error sources in the angular resolution (clock stability, optical beacon calibration system, etc.) are required to have $\sigma < 0.5$ ns to keep the previous values.

1.3.4.2 Energy Resolution

The energy resolution is also energy dependent. Detector simulations have shown that muon energy can be reconstructed within a factor 3 for $1 < E_\mu < 10$ TeV. Due to the increase in ionization, for $E_\mu >$ TeV the energy resolution is roughly a factor 2. In order to do that, light amplitude has to be measured with a resolution better than 20%.

1.4 Other neutrino telescopes

There are other projects to perform neutrino astronomy:

- **DUMAND [41]** was the first of such detectors. It started in 1975, in Hawaii, and decommissioned in 1996. During this time many technical studies, very useful for the actual experiments, were performed.
- **BAIKAL** [42] is the first demonstration of feasability for underwater neutrino telescopes. It started in 1981 and has been deployed in the Siberian lake Baikal at 1300 m depth. It has 8 strings holding 192 optical modules. During 1998, 36 neutrino candidates have been detected, which is compatible with the expected atmospheric neutrino rate.
- **AMANDA** [43] is deployed in the South Pole, using ice as target and Cherenkov medium. Three different stages have been developed: AMANDA-A (4 strings, 80 OMs), AMANDA-B (10 strings, 302 OMs) and AMANDA-II (9 lines, 677 OMs). AMANDA-B has measured 188 atmospheric neutrino candidates and AMANDA-II is taking data.
- **NESTOR** [44] forsees to deploy a tower with 168 OMs in the Ionian sea (Greece). Environmental measurements have already been performed.
- **NEMO** [45] is performing environmental studies to identify the best site for the neutrino telescope in the Mediterranean sea.

Chapter 2

Characteristics of Photomultipliers. Experimental Setup.

Photomultiplier tubes (PMTs) are a key component of the ANTARES detector. As it has been explained in the previous chapter, muons emit Cherenkov light which has to be detected and this has to be converted into an electronic signal, that can be managed easily. This process is explained in the first section of this chapter. In Section 2.2, the measurements to parameterize the photomultiplier response The experimental setup are described in Section 2.3. The models we have studied are presented in Section 2.4. Finally, the ANTARES specifications are given.

2.1 Basic principle of photomultipliers

The process by which the incident photon is converted into an electronic signal can be divided in three stages. First, the photon is absorbed by the photocathode material and an electron is emitted, due to the photoelectric effect. This electron has to be focused towards the amplification chain by means of electric fields. This stage is specially delicate in those photomultipliers with a large photocathode surface, as it is our case. Finally, this so-called photoelectron is multiplied to produce a measurable charge in the dynode chain, which is collected in the anode. Figure 2.1 is a schematic view of a typical photomultiplier tube.

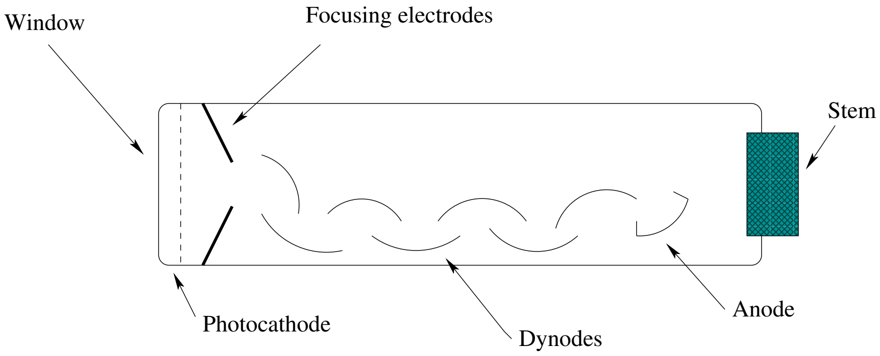

Figure 2.1: Schematic view of a photomultiplier tube. The three stages are indicated: photocathode emission, focalization and current amplification.

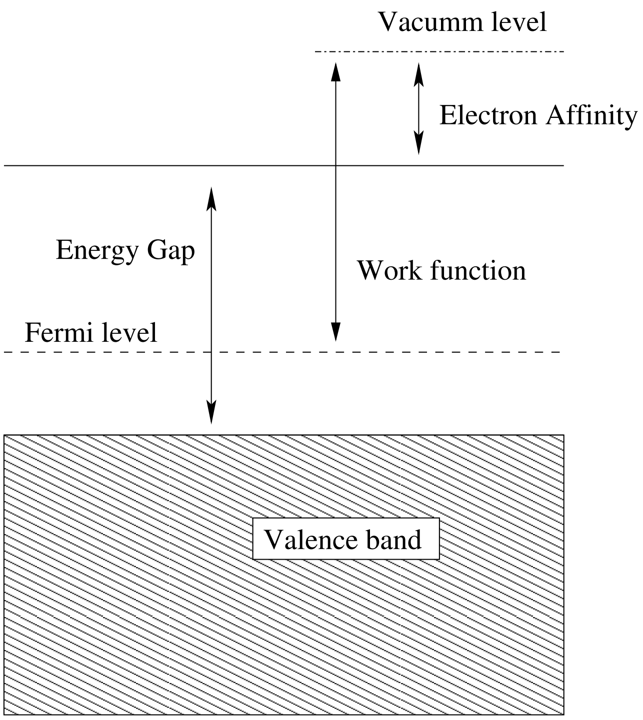

Figure 2.2: Alkali photocathode band model.

2.1.1 Photoelectron emission

2.1.1.1 Photocathode materials

Photocathodes are made of semiconductor materials. In Figure 2.2, the band diagram of an alkali photocathode is shown. The energy gap is the band which cannot be occupied by electrons. When a photon with energy $h\nu$ reaches the material it is absorbed by an electron which becomes excited and diffuses towards the photocathode surface. If it has energy enough, it can be emitted to the vacuum.

The number of photoelectrons emitted from the photocahtode over the number of incident photons (quantum efficiency) is given by [46]:

$$\eta(\nu) = (1 - R)\frac{P_\nu}{k}\left(\frac{1}{1 + 1/kL}\right) P_s \tag{2.1}$$

where:

- η: quantum efficiency.
- R: reflection coefficient.
- k: full absorption coefficient of photons.
- P_ν: probability that light absorption may excite electrons to a level greater than the vacuum level.

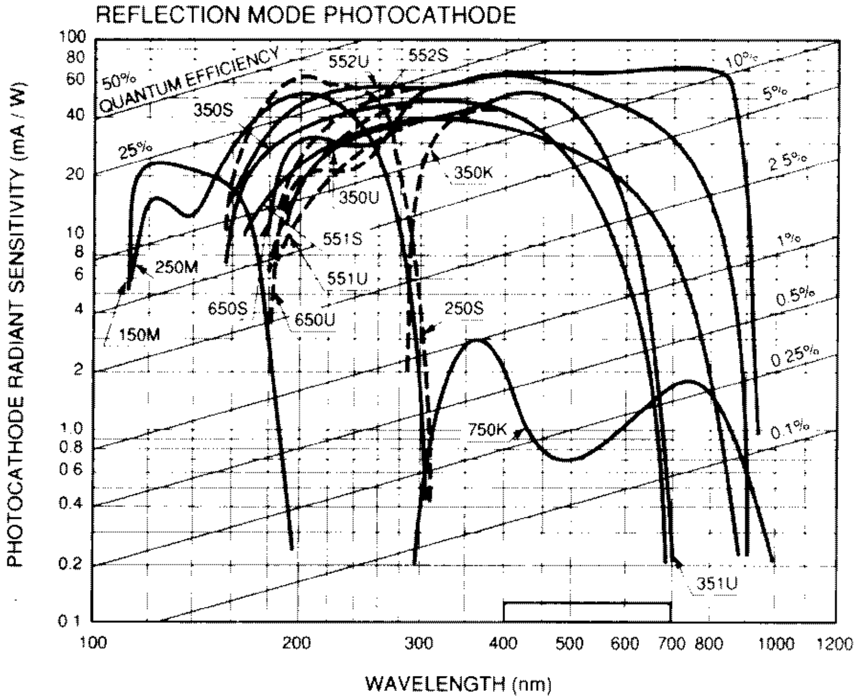

Figure 2.3: Radiant sensitivity of typical photocathode materials [46].

- L: mean escape length of excited electrons.
- P_s: probability that electrons reaching the photocathode surface are released into the vacuum.
- ν: frequency of light.

There are two modes of emission. In the reflection photocathodes, photoelectrons are emitted in the direction opposite to the incident light. They are mainly used for the side-on tubes, which receive light through the side of the glass bulb. In the transmission mode, photoelectrons are emitted in the same direction as the incident light and are used in head-on tubes, as it is our case.

Most materials used in photocathodes contain alkali metals with a low work function, such as Cs-I, Cs-Te, Sb-Sc, bialkali (Sb-Rb-Cs, Sb-K-Cs), Ag-O-Cs, GaAs(Cs) and InGaAs(Cs). Figure 2.3 shows the characteristic spectral response of the most typical photocathode materials. The parameter *radiant sensitivity* (S_k) which appears in this plot is the photoelectric current from the photocathode over the incident radiant flux. The relationship between the radiant sensitivity and the quantum effiency is given by:

$$S_k\ (A/m) = \frac{\lambda e}{hc}\eta = \frac{\lambda\ (nm)}{1240}\eta \tag{2.2}$$

As it will be mentioned in Section 2.4, the photocathode of the photomultipliers we have studied are of the so-called bialkali type. In the transmission mode, the spectral response range goes from the ultraviolet to the visible.

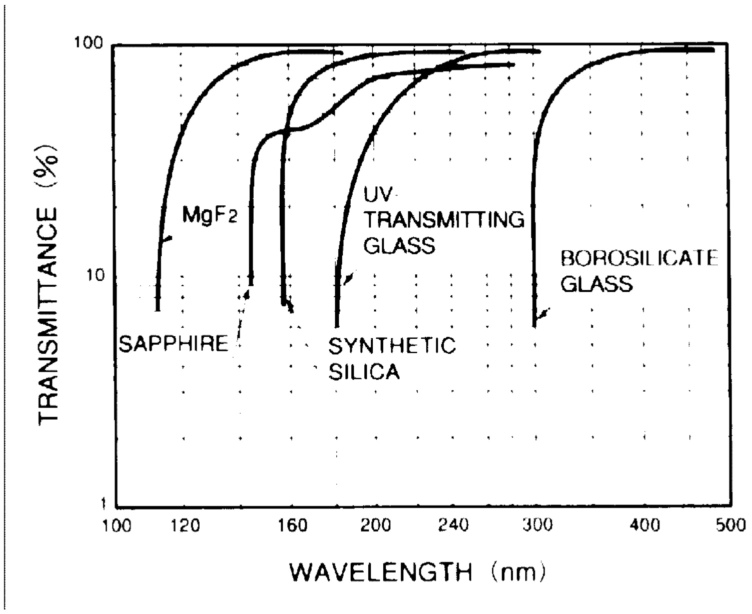

Figure 2.4: Spectral transmittance of typical window materials [46].

2.1.1.2 Window materials

The window material also limits the spectral response of the photomultiplier. Typical window materials are MgF_2 crystal, sapphire, synthetic silica, UV glass and borosilicate glass. Most photocathodes, i.e. bialkali ones, have sensitivity in the ultraviolet region, but the window absorbs this light. In Figure 2.4, the spectral transmittance of these materials is shown. Borosilicate glass is the most used material, as it is the case of the models in this study. It does not transmit ultraviolet radiation shorter than 300 nm.

2.1.2 Focalization

Focalization is needed to collect the photoelectrons and drive them to the amplification chain. In general, optics is optimized under two factors:

- **collection efficiency**: this is the number of photoelectrons which arrive at the dynode chain over the total number of photoelectrons produced in the photocathode. It depends on the wavelength of the incident light and is in general larger than 80%.
- **transit time spread up to the first dynode**: this parameter is the spread of the arrival time distribution of the photoelectrons from the photocathode to the amplification chain.

In the ANTARES experiment, the second factor is specially important, since the event reconstruction depends strongly on the time resolution and hence on the time spread of the photomultiplier. There are basically two factors which contribute to this transit time spread:

- **chromatic contribution**: the initial speed of the photoelectrons has two components, normal and parallel to the photocathode, corresponding to energies E_n and E_t, respectively. The fluctuation in the transit time due to a fluctuation in E_n is [47]:

$$\Delta t_n = \frac{1}{\varepsilon e}\sqrt{2m_e \cdot \Delta E_n} \tag{2.3}$$

where ε is the electric field in the photocathode surface.

On the other hand, there is an additional fluctuation produced in the first dynode due to the transverse component of the speed:

$$\Delta t_t \simeq \frac{r_0}{v} \tag{2.4}$$

where r_0 is the radius of the photoelectron diffusion zone in the first dynode and v is its speed when it reaches this dynode.

- **geometric contribution**: it comes from differences in the path lengths to the first dynode in different parts of the photocathode and non-homogeneities in the electric field. The second factor is difficult to parameterize, but the fluctuations due to different path lengths are given by:

$$\Delta t = \Delta L \sqrt{\frac{m_e}{2e\varepsilon L}} \tag{2.5}$$

The large size of the photocathodes in our detector implies that a very elaborate focalization system is needed to reach a time resolution good enough.

2.1.3 Current amplification

The amplification chain aims to produce a detectable electrical signal from one photoelectron. The mechanism to this end is as follows. The photoelectron is accelerated up to the first dynode. There, it losses its energy, allowing several electrons of the dynode material to escape towards the second dynode driven by the electric field. There, each of these electrons will also undergo the same process, called *secondary emission*. The multiplication factor depends on the type of photomultiplier, but can be larger than 10^8.

To describe mathematically this process, we express the *secondary emission ratio* δ as:

$$\delta = a \cdot v^x \tag{2.6}$$

where a is a constant, x is determined by the material of the electrode, typically with a value from 0.7 to 0.8 and v is the interstage voltage of the dynodes.

In the first dynode, the incoming current from the photocathode I_k produces an outgoing current I_1. Furthermore,

$$\delta_1 = \frac{I_1}{I_k} \tag{2.7}$$

This process continues in the next dynodes, so in general:

$$\delta_n = \frac{I_n}{I_{n-1}} \tag{2.8}$$

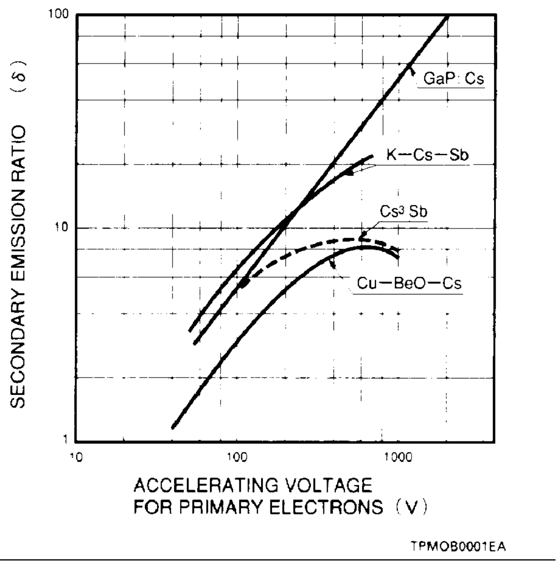

Figure 2.5: Secondary emission ratios of most common dynode materials [46].

The anode current I_a will be:

$$I_a = I_k \cdot \alpha \cdot \delta_1 \cdot \delta_2 \ldots \delta_n \tag{2.9}$$

where α is the collection efficiency.

The current amplification μ, defined as the ratio between the anode current and the photocathode current can be expressed as:

$$\mu = \frac{I_a}{I_k} = \alpha \cdot \delta_1 \cdot \delta_2 \ldots \delta_n \tag{2.10}$$

In order to simplify, we can assume that α=1 and an equal division of the voltage in the dynodes. In this case, the dependence of μ on the supply voltage V is:

$$\mu = (a \cdot v^x)^n = a^n \left(\frac{V}{n+1}\right)^{xn} = A \cdot V^{xn} \tag{2.11}$$

where A=$a^n/(\text{n+1})^{xn}$. Furthermore, the current amplification μ is proportional to the xn exponential power of the voltage.

Concerning the materials used for the dynodes they are chosen to have a good secondary emission efficiency. For instance, alloys such as AgMg, CuBe and NiAl produce oxides (MgO, BeO, Al_2O_3) in the surface of the dynode which give ~8 secondary electrons for incident electrons with an energy of 500 eV. On the other hand, some materials used for the photocathode are also suited for the dynodes, such as SbCs. In Figure 2.5 some of these materials are compared.

Another fundamental point in the amplification chain is the configuration of the dynodes. There are several possible structures, as it can be seen in Figure 2.6.

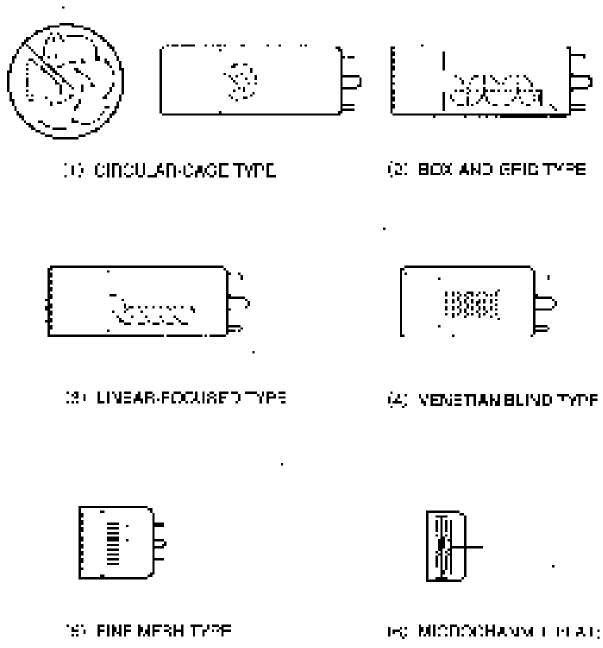

Figure 2.6: Types of dynode structures of the amplification chain.

- **Circular cage**: this configuration allows a good compactness and a fast time response. It is mainly used in side-on tubes.

- **Box-and-grid**: the main advantages of this type are the high collection efficiency and the good uniformity.

- **Linear-focused**: these photomultipliers feature in fast time response, good time resolution and excellent pulse linearity.

- **Venetian blind**: this type allows a good collection efficiency with a simple design. They are used very often for large photocathode tubes.

- **Fine-mesh**: in this configuration, the electric field is nearly parallel, what makes these tubes less sensitive to magnetic fields.

- **Microchannel plate**: in photomultipliers, the dynode is a microchannel plate with 1 mm thickness. The main advantages are the excellent time resolution and its immunity to tens of miliTeslas magnetic fields.

After the last dynode, the charge is collected in the anode. An important factor to optimize in this last stage is the spatial charge, because it degrades the linearity.

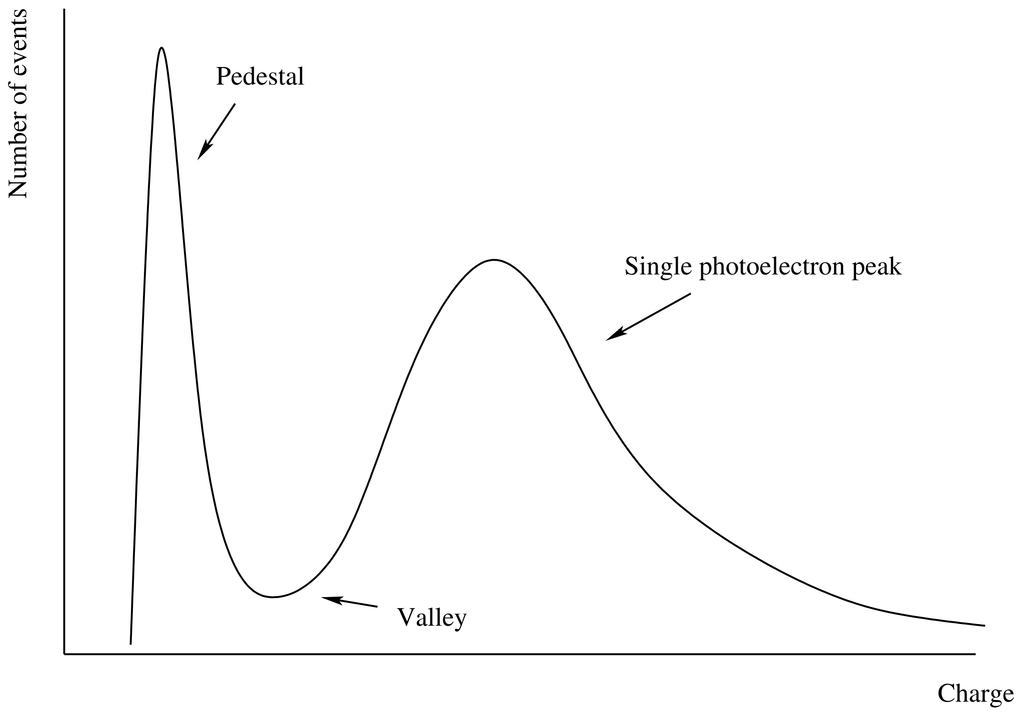

Figure 2.7: Scheme of a typical charge spectrum at the level of illumination of a single photoelectron.

2.2 Main parameters of photomultipliers

In this section, the main parameters of the photomultipliers are described. Most of them have been studied in the laboratory, as it will be seen in the following chapter.

2.2.1 Charge spectrum

An important measurement to characterize a photomultiplier is the charge spectrum. Figure 2.7 shows a scheme of one of these distributions. The main parameters of the spectrum are indicated.

The number of photoelectrons emitted in the photocathode, at a fixed level of light, is assumed to follow a poissonian distribution. A specially useful case is the *single photoelectron* (SPE) spectrum in which the amplified charge of one photoelectron dominates. In a SPE spectrum, the peak of one photoelectron is very clear, so important information can be obtained:

- The mean charge of one photoelectron is obtained from the position of the SPE peak. The gain of the photomultiplier is the ratio of this mean to the charge of one electron.
- The peak to valley ratio is the quotient between the height of the SPE peak and the height of the valley zone. The larger this parameter, the better the SPE events can be distinguished.
- The energy resolution is the ratio of the width of the SPE peak to the position of this peak, usually expressed in percentage.

In Section 3.1, the different contributions of this spectrum are discussed in more detail.

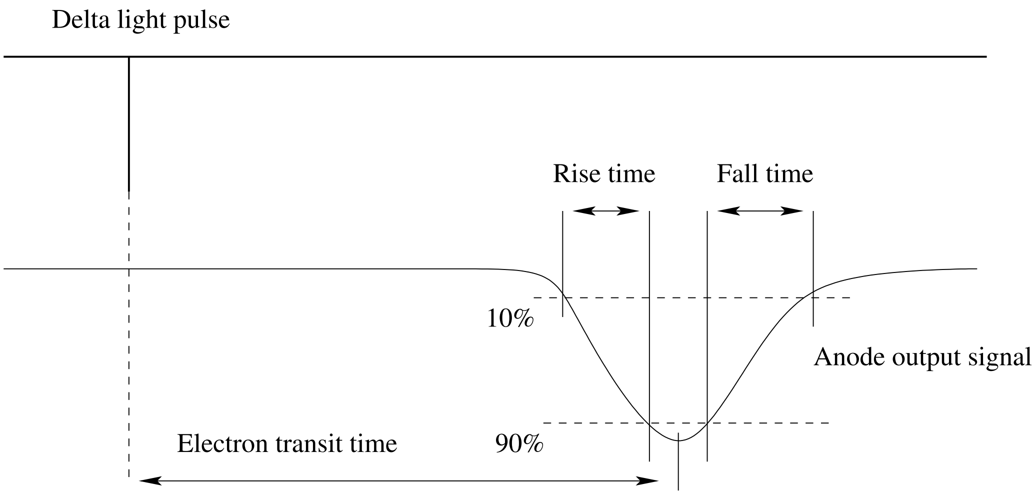

Figure 2.8: Definitions of rise time, fall time and transit time. The TTS is the FWHM of the transit time distribution.

2.2.2 Timing Properties

Timing properties are a key characteristic in many applications of the photomultiplier tubes. Figure 2.8 illustrates the relevant parameters.

2.2.2.1 Rise and fall time

The rise time is the interval in which the anode signal goes from 10% to 90% of its maximum amplitude, assuming a delta distribution of the source pulse. Conversely, the fall time is defined as the time to go from 90% to 10%. In general, the latter is two or three times longer than the former. Both parameters depend on the photomultiplier type.

2.2.2.2 Transit time

The transit time is the interval between the arrival of a light pulse at the photocathode and the output of the anode signal. The transit time is proportional to $1/\sqrt{V}$, where V is the high voltage applied to the photomultiplier.

The transit time depends on the tube type and is of the order of tens of nanoseconds. It also depends on the size of the tube.

2.2.2.3 Transit time spread (TTS)

The transit time spread is the most important timing characteristic of the photomultipliers in applications where a good time resolution is necessary. It is defined as the FWHM of the transit time distribution. In Section 2.1.2 the TTS of the focalization stage was presented. This contribution is included now and it is the main component in the total TTS but not the only one. Fluctuations in the amplification chain have a small contribution.

The transit time spread and the number of photoelectrons per pulse are related to each other, being the TTS proportional to $1/\sqrt{n}$.

2.2.3 Other characteristics

2.2.3.1 Dark current

When a photomultiplier is working in a completely dark environment there should be no current from the anode. However, this is not actually true since a small current (called dark current or dark noise) is present due to several factors:

- **Thermionic emission current from the photocathode and dynodes**
  The photocathode and the dynode materials have a very low working function so thermionic emission is produced even at room temperatures. This effect follows the Richardson law:

  $$i_s = AT^{5/4}e^{-e\phi/KT} \tag{2.12}$$

  where i_s is the anode current; ϕ, the work function; e, the electron charge; K, the Bolztmann constant; T, the absolute temperature, and A, a constant. As it can be seen in the previous equation, thermionic emission depends on the material and the temperature. The lower the work function, the wider the spectral response and the higher the dark current. An effective method in order to reduce this contribution to the dark current is to cool the photomultiplier. At room temperature, thermionic emission is the main factor in the dark current, but cooling reduces it significantly. Dark current from the photocathode is higher than from the dynode. This is because the photocathode surface is larger and the dynodes of the later stages contribute less to the output current.

- **Leakage current**
  Since photomultipliers work at high voltages and low currents, insulating materials are very important. The contribution to the dark current coming from leakage in the insulation is worked out with the Ohm's law:

  $$i_l = \frac{supply\ voltage}{insulation\ resistance} \tag{2.13}$$

  At low voltages, the leakage current has relatively more effect on the dark current, since thermionic emission varies exponentially with voltage. On the other hand, and as it has been mentioned, leakage current is the most important factor at low temperatures, when the thermionic effect is lower. In order to minimize this leakage, it is important to avoid contamination from dirt and moisture.

- **Scintillation from the glass envelope or electrode support materials**
  This occurs when electrons deviated from their normal trajectory reach the glass envelope, producing scintillations. This problem can be reduced by applying a conductive paint around the outside of the bulb and connecting it to the cathode potential.

- **Field emission**
  At very high voltages, some electrons may be emitted from the electrodes due to the strong electric field, causing an increase in the dark current. This phenomenon is dangerous because it may damage the photomultiplier. To avoid this, it is necessary to work at a voltage lower than the maximum voltage specified by the manufacturer.

- **Background radiation**
  There are also other contributions to the dark current. On one hand, cosmic rays, specially

muons, can produce Cherenkov emission when passing through the glass envelope. Another important source of dark current comes from the potassium oxide (K_2O) of the glass, since the isotope ^{40}K emits beta rays. In order to reduce this problem, the K_2O content is minimized when the glass is made.

2.2.3.2 Afterpulses

The signal from the anode is sometimes accompanied by a second synchronous signal. This phenomenon is called afterpulsing. There are two main causes with different characteristics. On one hand, what we call *afterpulses-1*, are produced almost immediately after the main pulse (the delay is from several nanoseconds to several tens of nanoseconds). These are mainly caused by photons emitted in the last dynodes. These photons reach the photocathode and produce a new photoelectron, which is multiplied as usual.

On the other hand, there are pulses delayed several microseconds. They are called *afterpulses-2* and are produced by the ionization of the residual gas inside the tube. The most usual ions are H_2^+, He^+, C_4^+ and Cs^+. The transit time for them is much longer than for electrons due to the mass difference. They are produced mainly in the last dynodes, since the electron current is higher there.

Finally, two other types of pulses are considered. They are not afterpulses but they are related to them. First, *prepulses* are produced before the main pulse when a photon goes through the photocathode and interacts in the first dynode. Since the path for these photoelectrons is shorter, the signal is produced a few tens of nanoseconds earlier than usual.

Delayed pulses, on the other hand, are produced when the photoelectron leaving the photocathode is intercepted and reflected by potential grids before reaching the first dynode. It is important to note that these pulses are in the same time window than afterpulses-1, but they are not in coincidence with a main pulse, since they are primary pulses..

2.2.3.3 Linearity

In principle, the number of photoelectrons collected in the anode should be proportional to the number of incident photons. This ideal case would mean a perfect linearity. However, there are some effects which produce deviations from this proportionality:

- **Voltage source**: The current in the anode can affect the voltage supplied to each dynode, and this produces a variation in the secondary emission coefficients and, therefore, a modification of the gain. Since the higher is the voltage, the larger is this variation (reduction), a loss of linearity is expected.

- **Space charge**: When a high number of photoelectrons are travelling through the tube, the electric field is modified and it can deviate some of these photoelectrons from their natural path and they can even be lost. The formula of Child-Langmuir gives the saturation density current between two electrodes.

$$I_s(A \cdot cm^{-2}) = 2.2 \cdot 10^{-6} \frac{V^{3/2}(volt^{3/2})}{a^2(cm^2)} \tag{2.14}$$

  The space charge effect is stronger in the last dynodes, since the charge density is higher. In order to reduce this lost of linearity, the voltage in the dynodes is not uniform, but it is increased progressively. This effect is also taken into account in the design of the dynode geometry.

2.3 Experimental setup

In this section the experimental setup used in the characterization of the photomultipliers is presented. It has been divided in three parts. After a general description of the setup, the light source is commented and finally, the results of complementary measurements are presented.

2.3.1 General description

Figure 2.9 shows a scheme of the experimental setup used for the photomultiplier characterization. This is only a general overview since a more detailed description is given for each measurement in Chapter 3.

The photomultiplier is set in a black box (80 cm $\times$ 80 cm $\times$ 140 cm) in order to protect them against the environmental light (see Figure 2.10 (left)). The high voltage is supplied by a NIM module located in the crate outside the box.

The photomultiplier is illuminated by means of a green laser, which is in an external black box. This laser is triggered by a pulse generator. An optical fiber guides the light from the laser to the PMT black box. In order to get a more uniform illumination a diffuser is used. The distance between the diffuser and the PMT surface is $\sim$60 cm. The output signal from the photomultiplier is sent to the crate by means of NIM and CAMAC modules. In some measurements, this signal is not sent to the crate but to the oscilloscope. Finally, the data are sent to the PC via a GPIB connector. Both the CAMAC modules and the oscilloscope can export information in this way. A picture of the rack with the NIM and CAMAC modules and the pulse generator can be seen in Figure 2.10 (right).

2.3.2 Light source

As it has been mentioned, the light source used to illuminate the photomultiplier is a green laser (see Figure 2.11 (left)), a Nd-YAG device, i.e. a synthetic ($Y_3Al_5O_{12}$) crystal dopped by Nd in concentrations of 10^{20} atoms/cm^3. The wavelength emission is 532 nm (it emits at 1064 nm but the light frequency is doubled). It is pulsed by the Q-switching mechanism, providing very fast pulses ($\sim$0.5 ns). The emitted energy per pulse is $\sim$1.2 μJ at 1.5 kHz. The output stability is better than 1% over several hours and the energy emission changes less than 1% after switching on and off. Moreover, these devices are small and robust, with an announced lifetime of $\sim 10^4$ operation hours.

This laser has an internal photodiode in its head which sends back a signal to the power supply when the laser shot is produced. Figure 2.11 (right) shows the timing diagram of the laser response.

2.3.3 Complementary measurements

Several complementary measurements have been performed in order to check the experimental setup. They are presented here.

- **Laser energy stability**
  One of the most relevant measurements is the stability of the energy emitted in each pulse. An energy detector (see Figure 2.12) was used to perform the measurement and the results

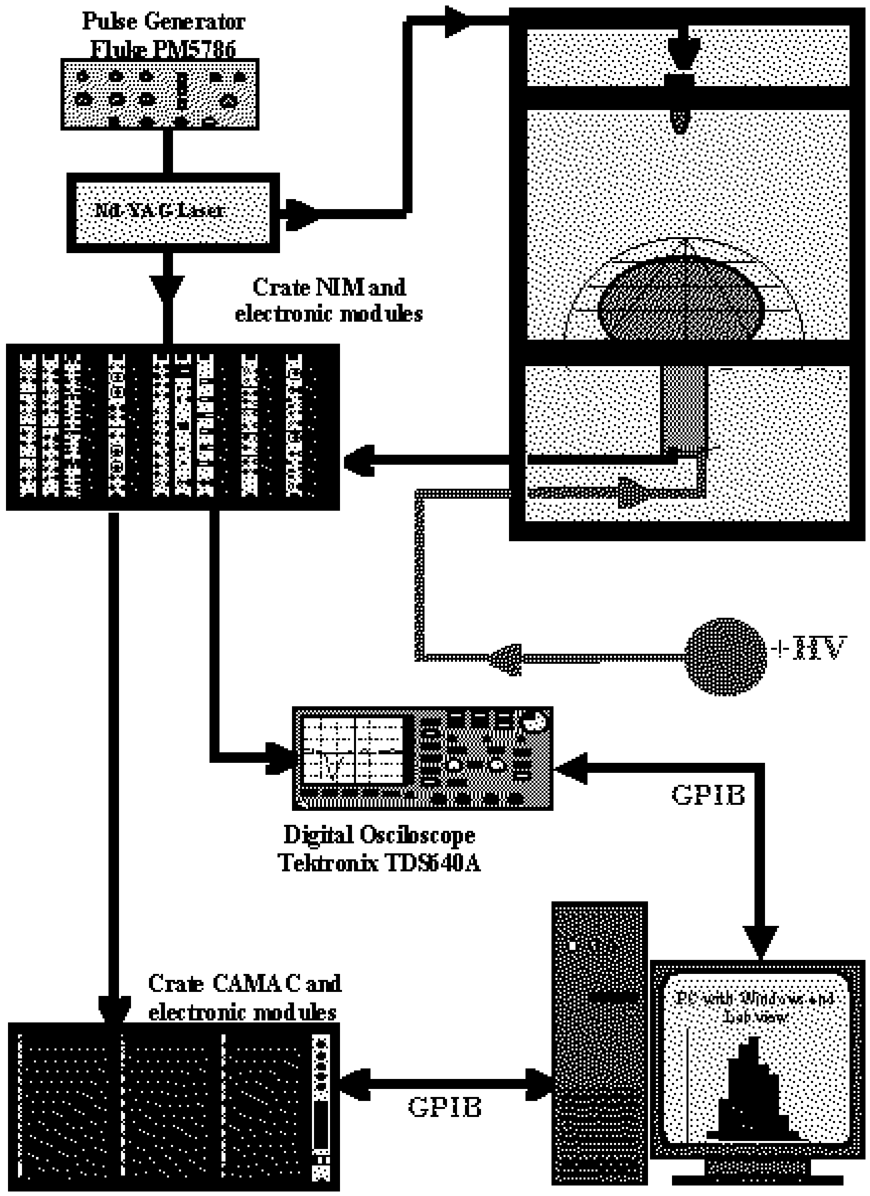

Figure 2.9: Schematic view of the experimental setup.

Figure 2.10: Left: picture of the black box with one of the Hamamatsu photomultipliers. Right: picture of the rack with the NIM and CAMAC modules; the oscilloscope can also be seen.

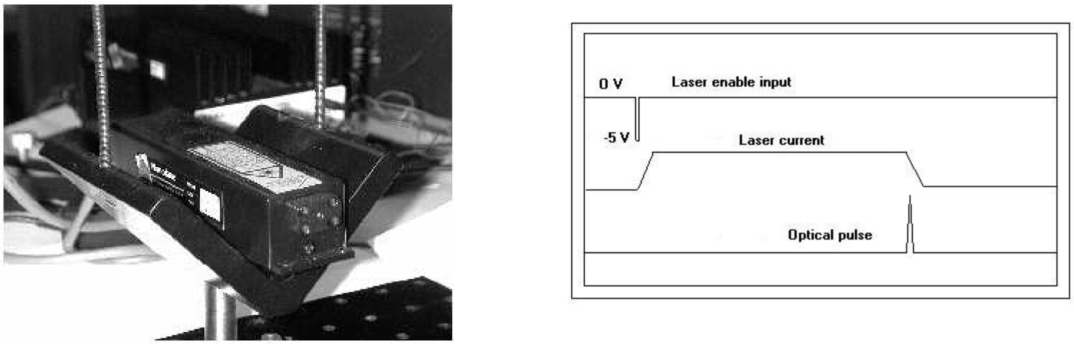

Figure 2.11: Left: picture of the laser used in the PMT characterization. Right: time diagram of the Q-switching of the laser.

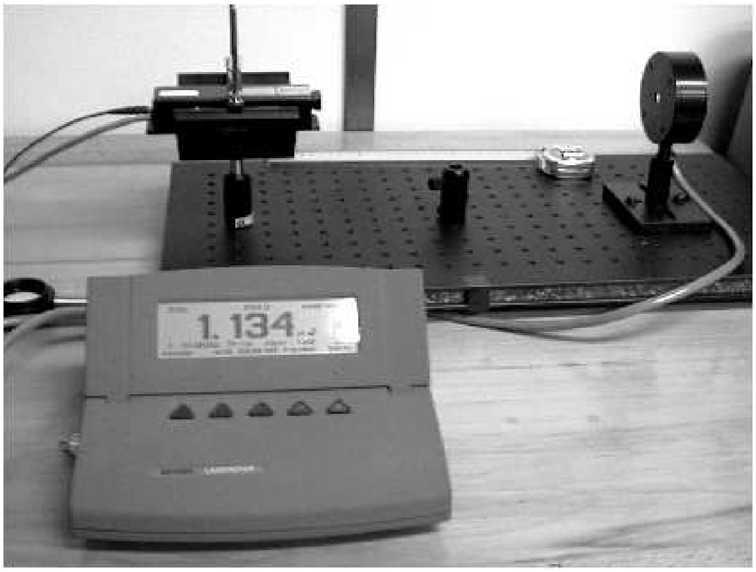

Figure 2.12: Picture of the OPHIR energy detector used to measure the laser stability.

can be seen in Figure 2.13. The conclusion is that after 2-3 minutes, the laser becomes stable for several hours (fluctuations $< 1\%$) [48].

- **Angular distribution from the diffuser**

  The angular distribution given by the diffuser has also been measured. This is important because as it has been mentioned, a pointlike illumination of the photocathode is not desirable. It would give, for instance, a wrongly small value of the TTS. This angular distribution has been measured by means of the OPHIR energy detector and the result is shown in Figure 2.14.

  The diffuser is expected to be Lambertian, i.e. the angular distribution has to follow a cosine behaviour. As it can be seen in the plot, when including an offset as free parameter, the fit is very good. To guide the eye, a pure cosine curve is also drawn.

- **ADC calibration**

  The ADC has to be calibrated to check the relationship between charge and channel number and the linearity range of the module. In Figure 2.15, the results of this calibration are shown.

  Both the relationship between charge and ADC channel and the linearity are as it is expected.

- **TDC calibration**

  In order to calibrate the TDC, we have used the pulse generator which can generate two independent NIM signals. The delay between them can be changed. The results for two of the channels can be seen in Figure 2.16. As it can be seen, a good linearity is observed.

2.4 Models under study

Two models of photomultipliers have been studied. On one hand, two tubes of the Photonis model XP1804/D2 and on the other hand four tubes from Hamamatsu, model R8055. In both cases, they have large photocathode and a long amplification chain to reach a gain $\sim 10^8$.

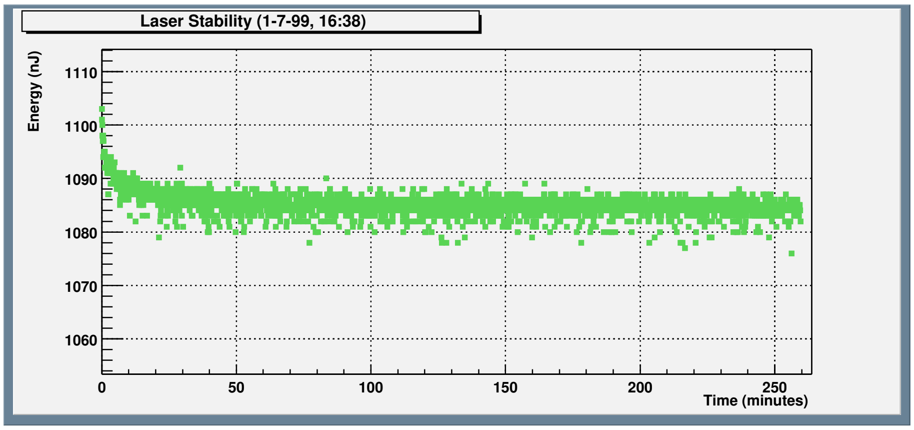

Figure 2.13: Energy emitted by the Nd-YAG laser as a function of time.

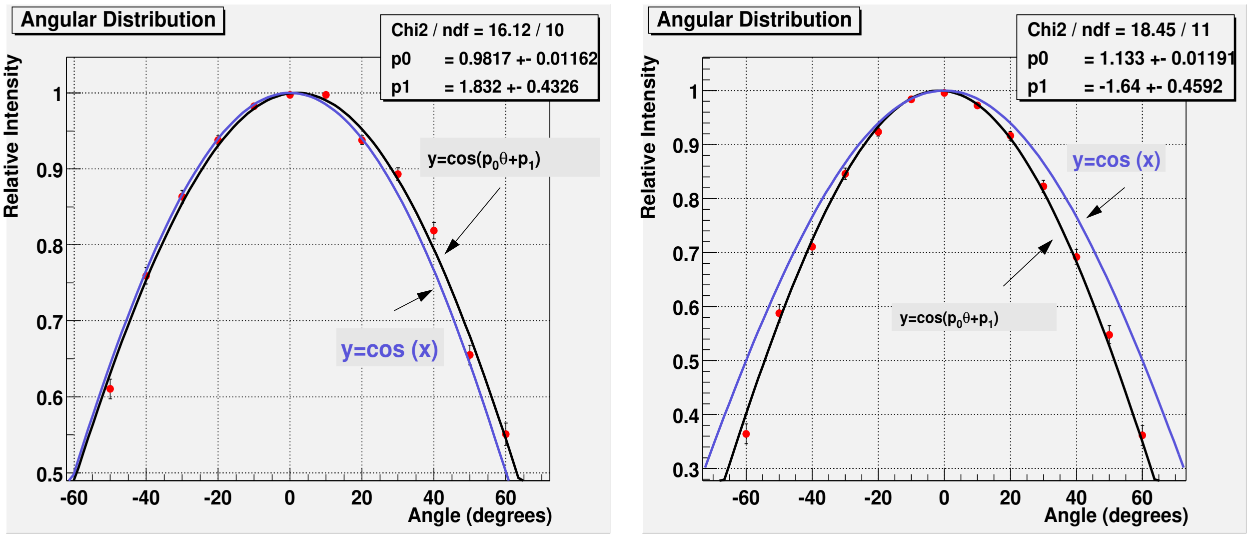

Figure 2.14: Angular distributions measured for two of the diffusers.

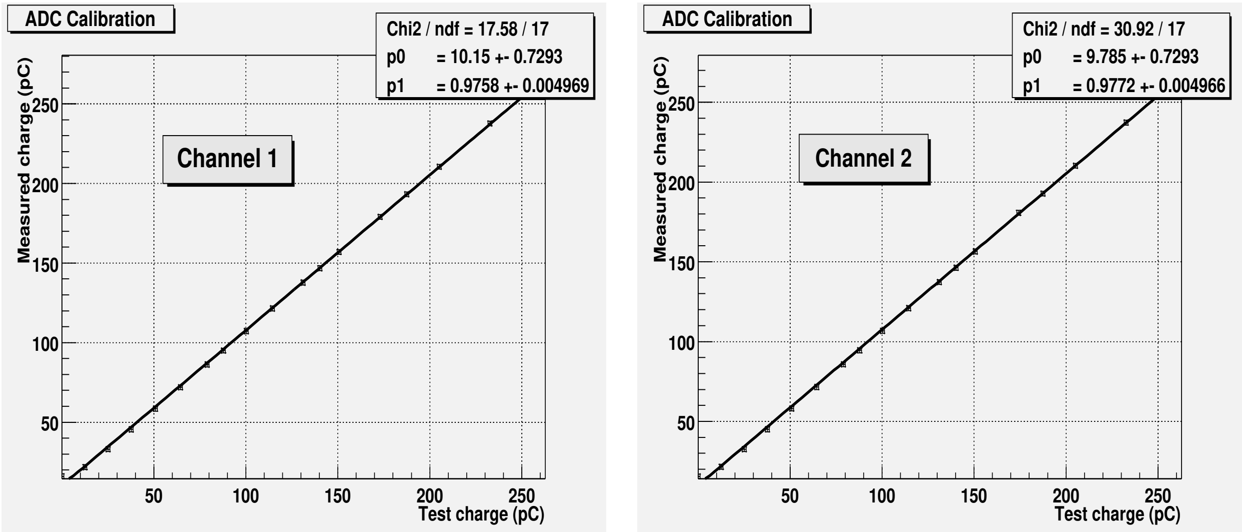

Figure 2.15: Example of the ADC calibration results.

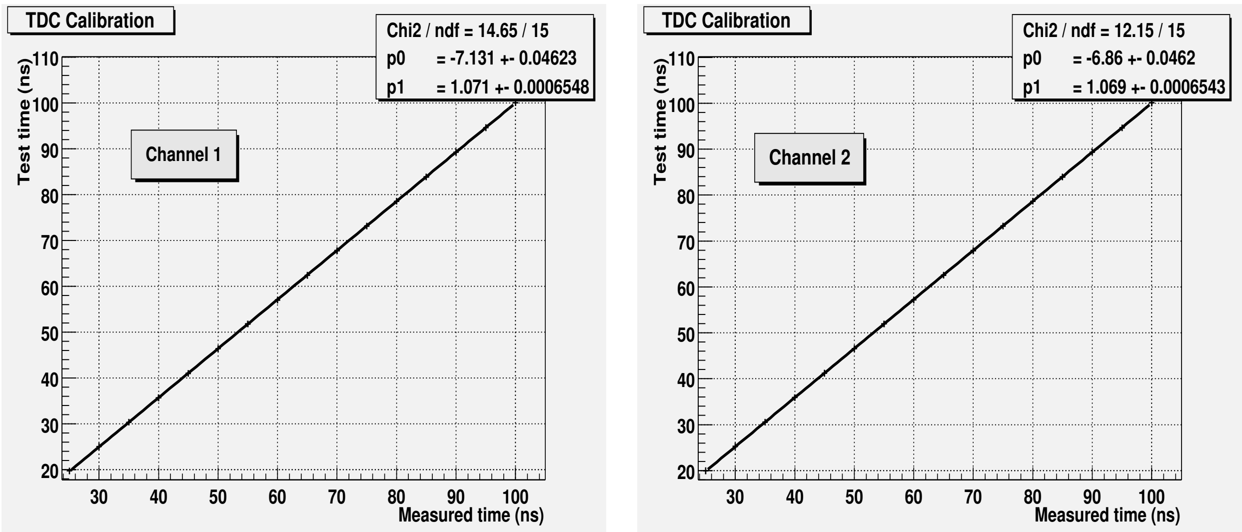

Figure 2.16: Example of the TDC calibration results.

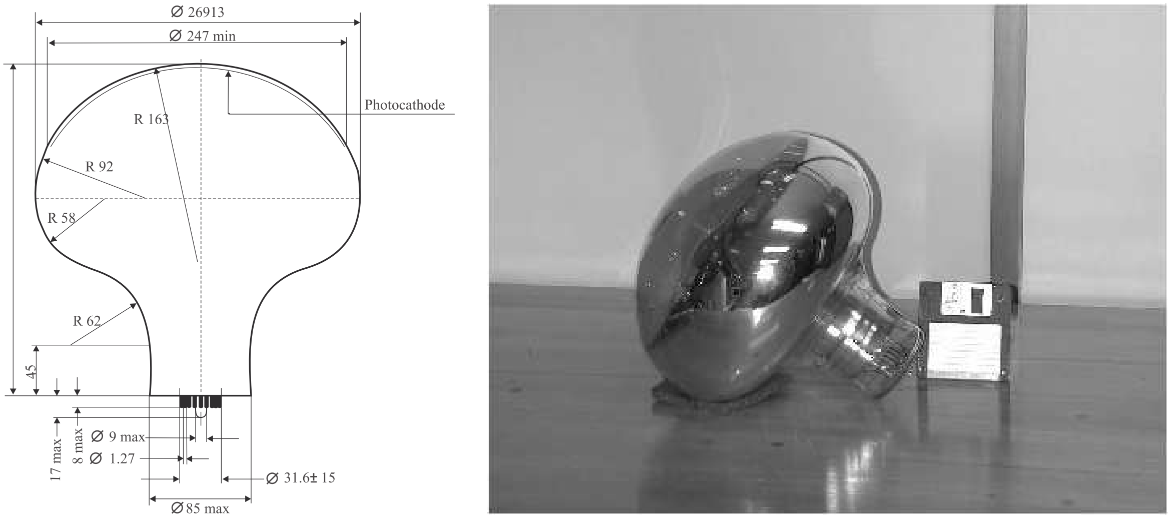

Figure 2.17: Left: schematics of the Photonis XP1804/D2 photomultiplier. Right: picture of one of these photomultipliers.

2.4.1 Photonis XP1804/D2

The diameter of these photomultipliers is 10.6". The photocathode is almost spherical and made of bialkali. There are 11 stages in the amplification chain, with a linear focused structure. Two tubes of this model have been studied, with serial numbers 35 and 39. Figure 2.17 shows the schematics and a picture of one of these tubes.

2.4.2 Hamamatsu R8055

These photomultipliers have a 13" photocathode diameter. As in the previous case, it is almost spherical and is made of bialkali. The number of stages is 10, in a box line structure. Four tubes of these model have been studied. Their serial numbers are AF0170, AF0171, AF0174 and AF0175. In Figure 2.18, the schematics and a picture of one of these photomultipliers can be seen.

Table 2.1 shows a comparison of the two models under study.

Parameter	**Photonis**	**Hamamtsu**
Model name	XP1804/D2	R8055
Photocathode diameter	10.6"	13"
Photocathode material	Bialkali	Bialkali
Number of stages	11	10
Dynode structures	Linear focused	Box line

Table 2.1: Characteristics of the models under study.

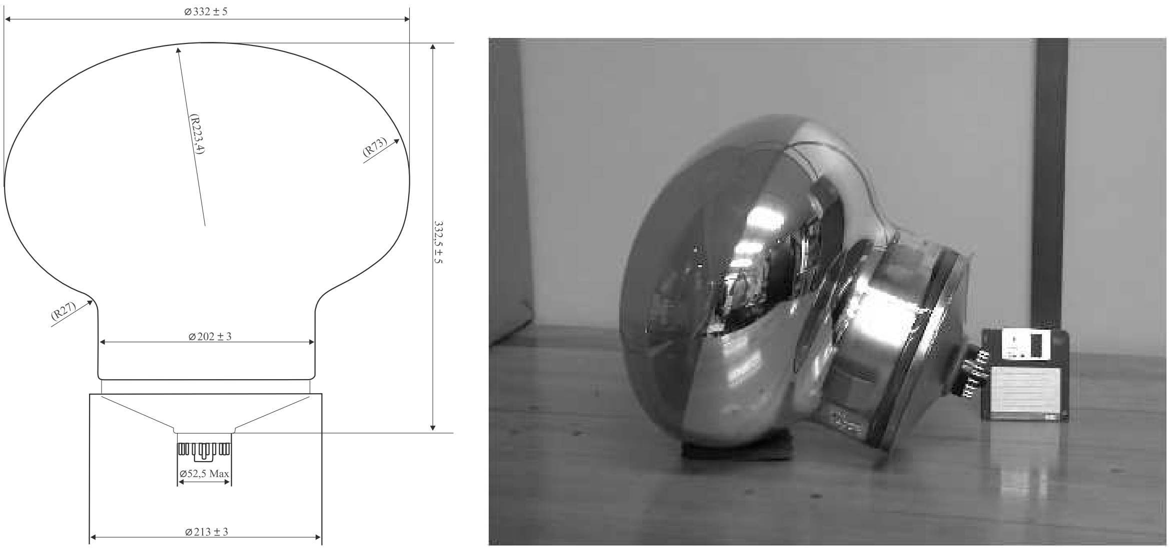

Figure 2.18: Left: schematics of the Hamamatsu R8055 photomultiplier. Right: picture of one of these photomultipliers.

2.5 ANTARES specifications

In this section, all the specifications required for the photomultipliers of the ANTARES detector are presented [49]. The rationale of these specifications lies in the experiment requirements and the present technological constraints of this type of photomultipliers. In the next chapter, the results obtained for the photomultipliers under study will be compared to these specifications.

- **Photomultiplier dimensions**: The inner diameter of the pressure-resistant spheres is 42.0 cm. Since other elements have to be included inside the sphere, the limit for the photocathode radius of curvature is 19.0 cm. Moreover, the maximum height is 35 cm.

- **Nominal voltage**: The nominal voltage is defined as the HV at which the gain is 5×10^7. The maximum acceptable value is 2000 V.

- **Amplitude**: In order to avoid the use of amplifiers, a good amplitude response is required for a SPE pulse. The minimum value according to the specifications is 50 mV on a 50 Ω load when the photomultiplier is working at the nominal voltage.

- **Peak to valley ratio**: A peak to valley ratio larger than 2 is required in order to be able to isolate properly a SPE from the pedestal.

- **Energy resolution**: In principle, there is no limit in the energy resolution, since the limit in the peak to valley ratio is enough. However, an energy resolution better than 40% is recommended.

- **Dark Noise**: Dark noise is not a critical parameter for the ANTARES photomultipliers due to the ^{40}K background. A limit to the dark current of 25% of the rate due to ^{40}K has been proposed. Experimental results [39] show that the ^{40}K rate is around 40 kHz for 8" Hamamatsu PMTs. Furthermore the limit value, which depends on the photocathode surface, is $\sim$30 Hz/cm^2.

- **Afterpulse rate**: In order to avoid spurious events, the maximum acceptable rates are: prepulses, 1%; delayed pulses, 5%; afterpulses-1, 1%, and afterpulses-2, 10%.

- **Transit time spread**: This is one of the most relevant parameters in the photomultipliers of the ANTARES detector. The limit value of TTS is FWHM=3 ns in order to reach an angular resolution of $\sim 0.2°$, as it was mentioned in Chapter 1.

Chapter 3

Results of the Photomultiplier Tests

In this chapter, the results obtained in the characterization of the photomultipliers under study are presented. The measurements performed are the following:

- Gain: dependence on high voltage and determination of the nominal voltage.
- Amplitude: dependence on high voltage and its relationship with gain.
- Peak to valley ratio: dependence on high voltage.
- Energy resolution: dependence on high voltage.
- Transit time spread: dependence on high voltage.
- Dark noise rate: dependence on high voltage and evolution after exposure.
- Afterpulse rate: prepulse, late pulse and afterpulse 1 and 2 rates and their dependence on high voltage.

As we have mentioned in the previous chapter, much of this information (gain, peak/valley, energy resolution) can be obtained from the SPE spectrum, so the fitting procedure is explained in detail in Section 3.1. Then, the results drawn from this spectrum are presented in the following sections. Results on amplitude are presented after those on gain, since both are closely related. Finally, TTS, dark noise and afterpulsing are analyzed in Sections 3.6, 3.7 and 3.8, respectively. All these results have been published as internal notes of the collaboration [50].

3.1 Single photoelectron charge spectrum

3.1.1 Fitting procedure

In Chapter 2, a scheme of a SPE charge spectrum was presented. In order to explain the shape of this spectrum, all the different processes have to be taken into account. Firstly, it can be assumed that the light emission from the source follows a Poissonian distribution. The *single* photoelectron level means that the mean number of photons arriving at the photocathode is lower than one, but there is a probability for a different number of photons, n, given by:

$$P(n;\bar{n}) = \frac{\bar{n}^n e^{-\bar{n}}}{n!} \tag{3.1}$$

where $\bar{n}$ is the mean number of photoelectrons.

The next stage is the photoelectric conversion. This can be described by a binomial distribution. Every photon can be converted into an electron with a probability given by the quantum efficiency η. Once the photoelectron is emitted, the collection efficiency α gives the probability that it reaches the first dynode, described by another binomial distribution. Therefore, the resulting distribution of these processes (light emission, photoconversion and collection) is the convolution of a Poissonian and two binomials, i.e. a Poissonian with mean:

$$\mu = \bar{n} \cdot \eta \cdot \alpha \tag{3.2}$$

Once the photoelectron reaches the first dynode, the multiplication process starts. The general way to treat this stage is to consider that the number of secondary electrons after every amplification is given by a Polya distribution:

$$P(n;\mu,b) = \frac{\mu}{n!}(1+b\mu)^{-n-1/b} \prod_{i=1}^{n-1}(1+ib) \tag{3.3}$$

where μ is the mean of the distribution and b is a parameter that modifies the shape of the function, from a Poissonian (b=0) to an exponential (b=1). For these photomultipliers a more simple hypothesis can be assumed. Due to the high number of stages and to the high gain, these Polyas can be approximated to Gaussians. Furthermore, if the parameters of the Gaussian for one photoelectron are μ_1 and σ_1, the parameters of the distributions for the coincidence of two or more photoelectrons (N) are given by the convolution of the corresponding Gaussians, i.e.:

$$\mu_N = N \cdot \mu_1 \tag{3.4}$$

$$\sigma_N^2 = N \cdot \sigma_1^2 \tag{3.5}$$

There are still two other considerations to be made. On one hand, it is necessary to take into account the pedestal: a positive shift in the position of the whole spectrum. There are two causes for this: the continuous component of the dark current and the intrinsic shift of the ADC. The pedestal can be approximated by a Gaussian with parameters μ_{ped} and σ_{ped}. On the other hand, the possibility of a bad amplification in the process of multiplication has to be considered. The most likely reason for that is the effect of backscattering in the dynodes. Typical values for the backscattering coefficient range from 20% to 30%. For these events, the charge for one photoelectron is smaller than the usual SPE charge. These bad amplified events lie in the so-called *valley* region between the pedestal and the SPE peak. The shape of this valley varies strongly with the PMT model. We have approximated it by the sum of an exponential and a Gaussian, so three parameters are needed to describe it: w is the fraction of wrongly amplified photoelectrons, β gives the fraction of valley events going to the exponential (and not to the Gaussian) and α is the slope of the exponential. The parameters of the Gaussian are worked out assuming that an amplification stage is lost. Notice that, since the voltage division in the bleeder is not homogeneous, these parameters would be different depending on which dynode has been lost. However, these differences can be ignored, specially because only the first dynodes contribute significantly.

The spectrum can be described by the distribution:

$$S(x) = G_{ped}(x) \otimes F_{valley}(x) \otimes \sum_{n=1}^{\infty} P(n;\mu) \otimes G_n(x) \tag{3.6}$$

where there are 8 parameters to fit:

- p_0: mean number of photoelectrons arriving to the first dynode (μ).
- p_1: mean of the Gaussian for the pedestal (μ_{ped}).
- p_2: width of the Gaussian for the pedestal (σ_{ped}).
- p_3: mean of the Gaussian for the one photoelectron peak (μ_1).
- p_4: width of the Gaussian for the one photoelectron peak (σ_1).
- p_5: rate of wrongly amplified single photoelectron events (w).
- p_6: slope of the exponential in the valley (α).
- p_7: rate of valley events going to the exponential and not to the Gaussian (β).

The fit is performed by a program written in C++ [3] which uses Minuit [51] to minimize χ^2. Due to the sensitivity to local minima, it is very important to give initial values to the parameters as close as possible to the true values. The fitting program gives errors around 0.1% or lower. When the fit process is repeated using slightly different initial values, variations of almost 1% are observed. These would be, hence, the statistical errors from the fit. However, when a measurement is repeated in the same experimental conditions, fluctuations are near 5%. These are, actually, the errors that have to be considered, since they give the true stability of the distribution due to the experimental conditions.

Figure 3.1 shows a typical example of a SPE charge spectrum. The different contributions (pedestal, valley and the peaks of one or more photoelectrons) can be seen. The contribution to χ^2 of each channel of the spectrum is shown in Figure 3.2.

3.1.2 Measurement and results

Figure 3.3 shows a scheme of the experimental setup used to obtain the charge spectrum. As it was mentioned is Section 2.3, a pulsed laser is used to illuminate the photomultiplier. The internal photodiode of the laser gives the gate signal, which is then inverted (in the Linear Fan In / Fan Out module) and discriminated. The gate is delayed to coincide with the photomultiplier signal.

The spectrum shape dependence on the photomultiplier tube and on the voltage can be seen in Figures 3.4 and 3.5, respectively.

All the spectra are taken at the SPE level, although the illumination is not exactly the same for all of them. The width of the SPE peak is in general wider for the Hamamatsu PMTs, which is related to the value of the energy resolution. Figure 3.6 shows the values of the paramters which define the valley (p_5, p_6 and p_7). The value of p_5 is higher for the Photonis PMTs. There is only one Hamamatsu tube with $p_5 > 0.2$. This parameter is important because it gives an idea of the backscattering coefficent of the dynodes. The lower p_5, the better the efficiency in the multiplication process. The parameters p_6 and p_7 give information on the shape of the valley. They show that the valley of all the tubes, except for Photonis 35 and Hamamatsu AF0175, are similar.

To evaluate the quality of the fit, we have to compare χ^2 with the number of degrees of freedom (ndf). In Figure 3.7, χ^2/ndf is plotted versus the high voltage for all the PMTs. Except for spectra obtained at low voltages, all the fits give good values of χ^2.

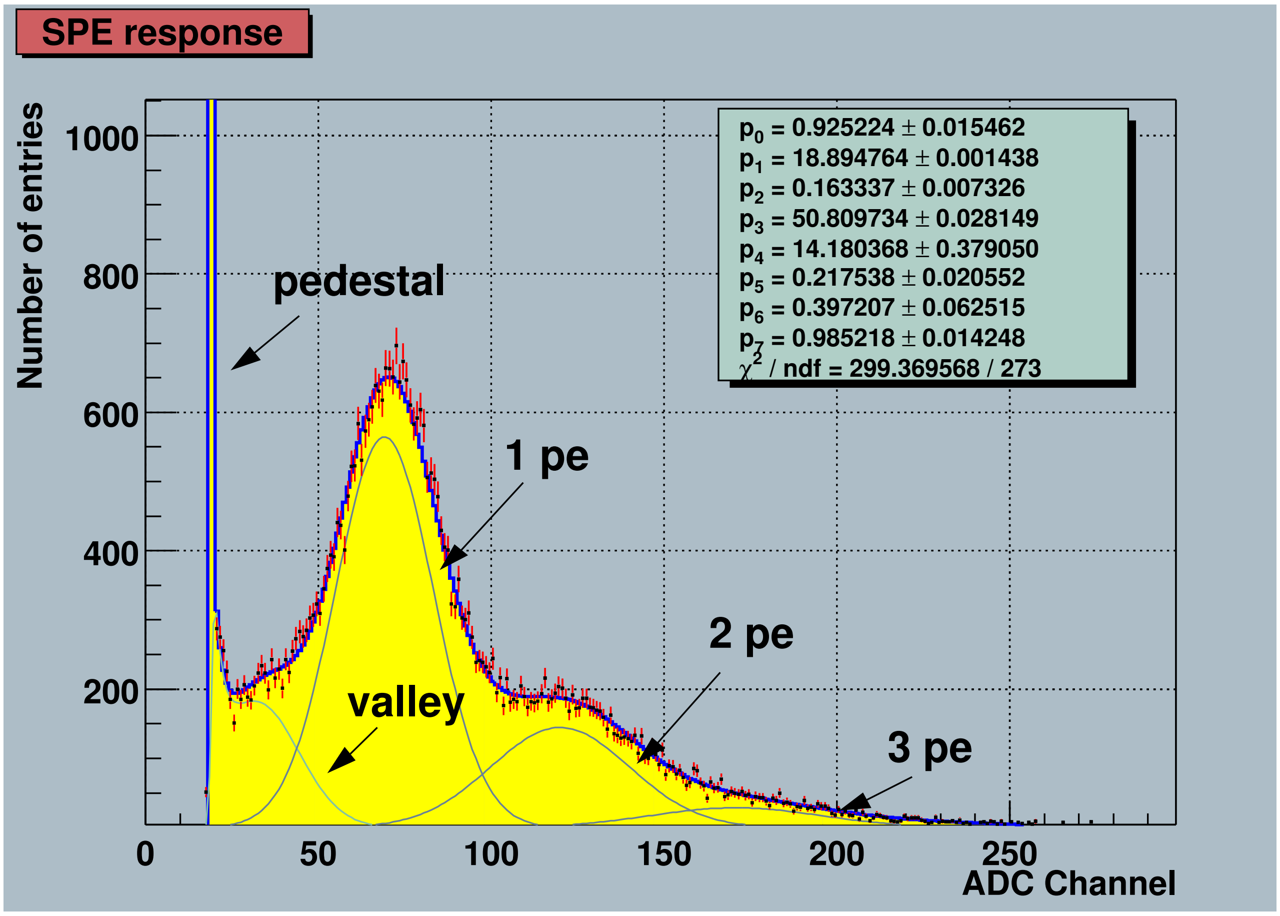

Figure 3.1: Example of single photoelectron charge spectrum. Each of the contributing distributions is also drawn.

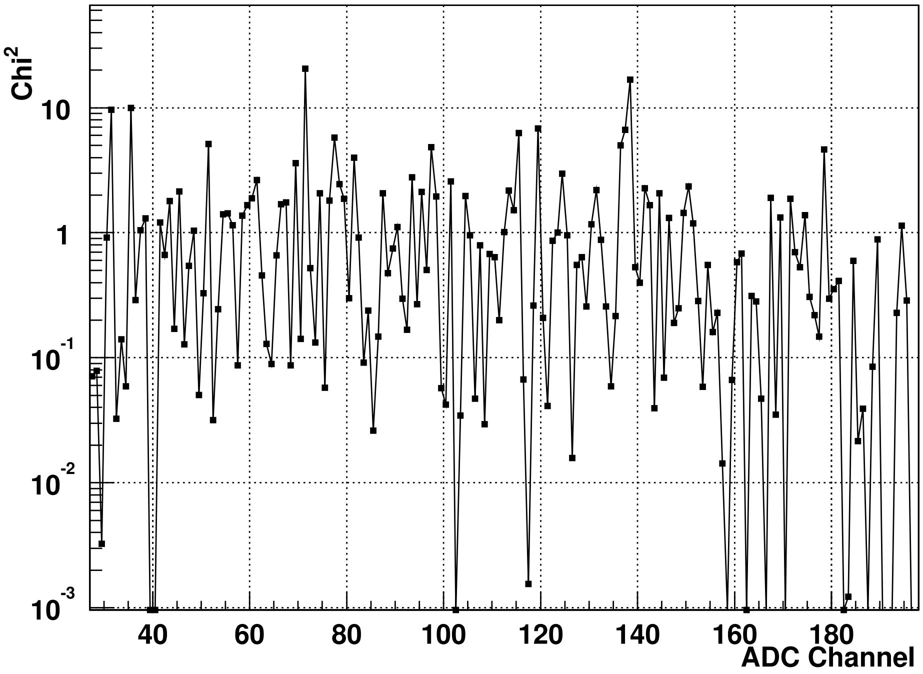

Figure 3.2: χ^2 of each channel of the spectrum. The values are distributed around one, giving a total χ^2/ndf of 1.09.

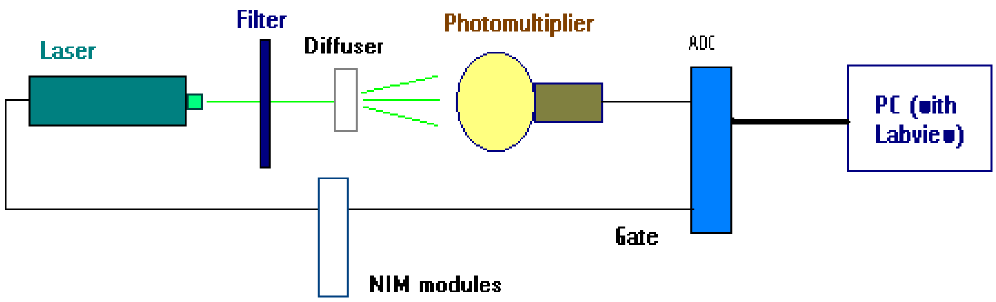

Figure 3.3: Experimental setup used in the charge spectrum measurement.

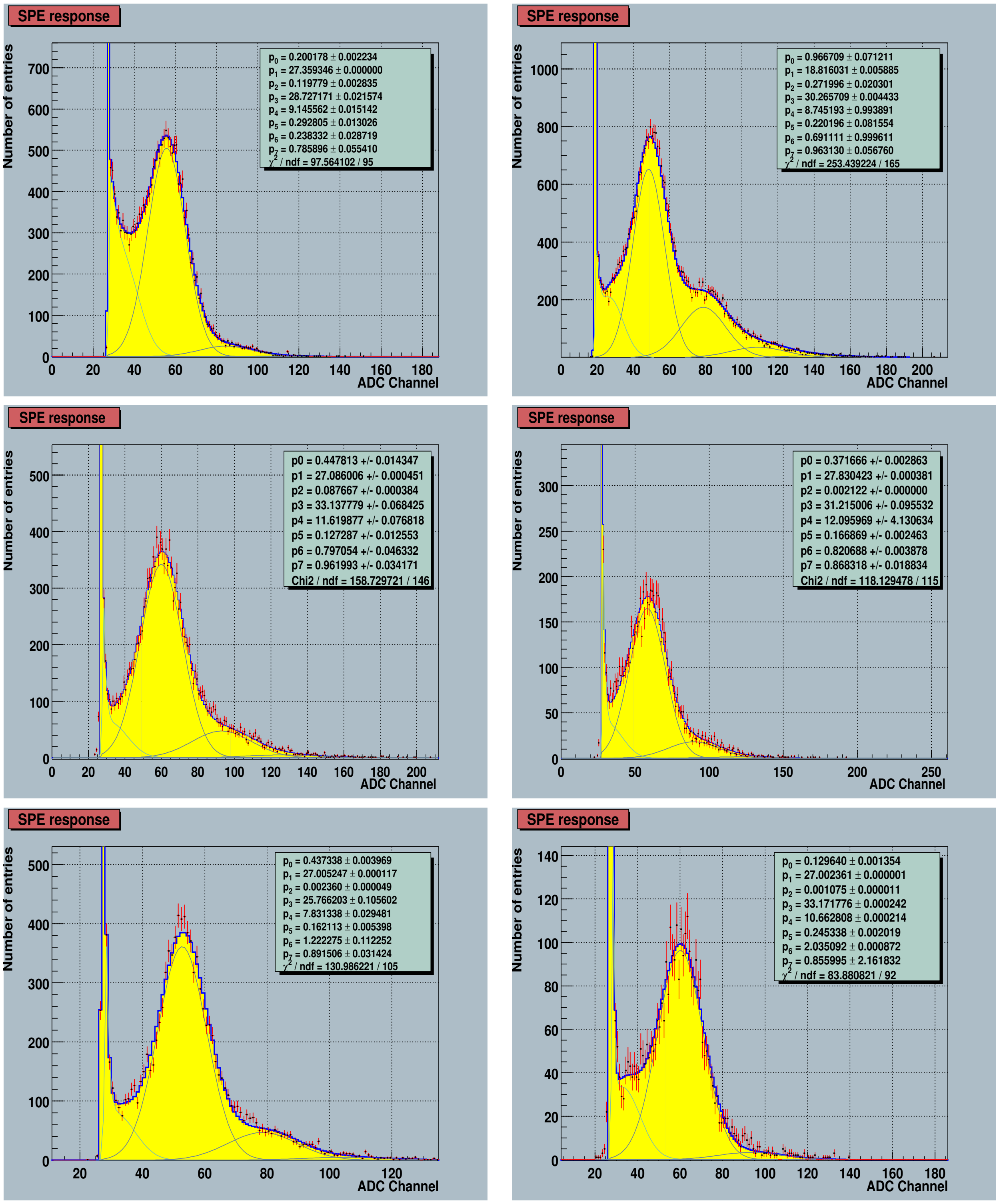

Figure 3.4: Charge spectra of all the models under study. From left to right and from up to bottom: Photonis 35 and 39 and Hamamatsu AF0170, AF0171, AF0174 and AF0175.

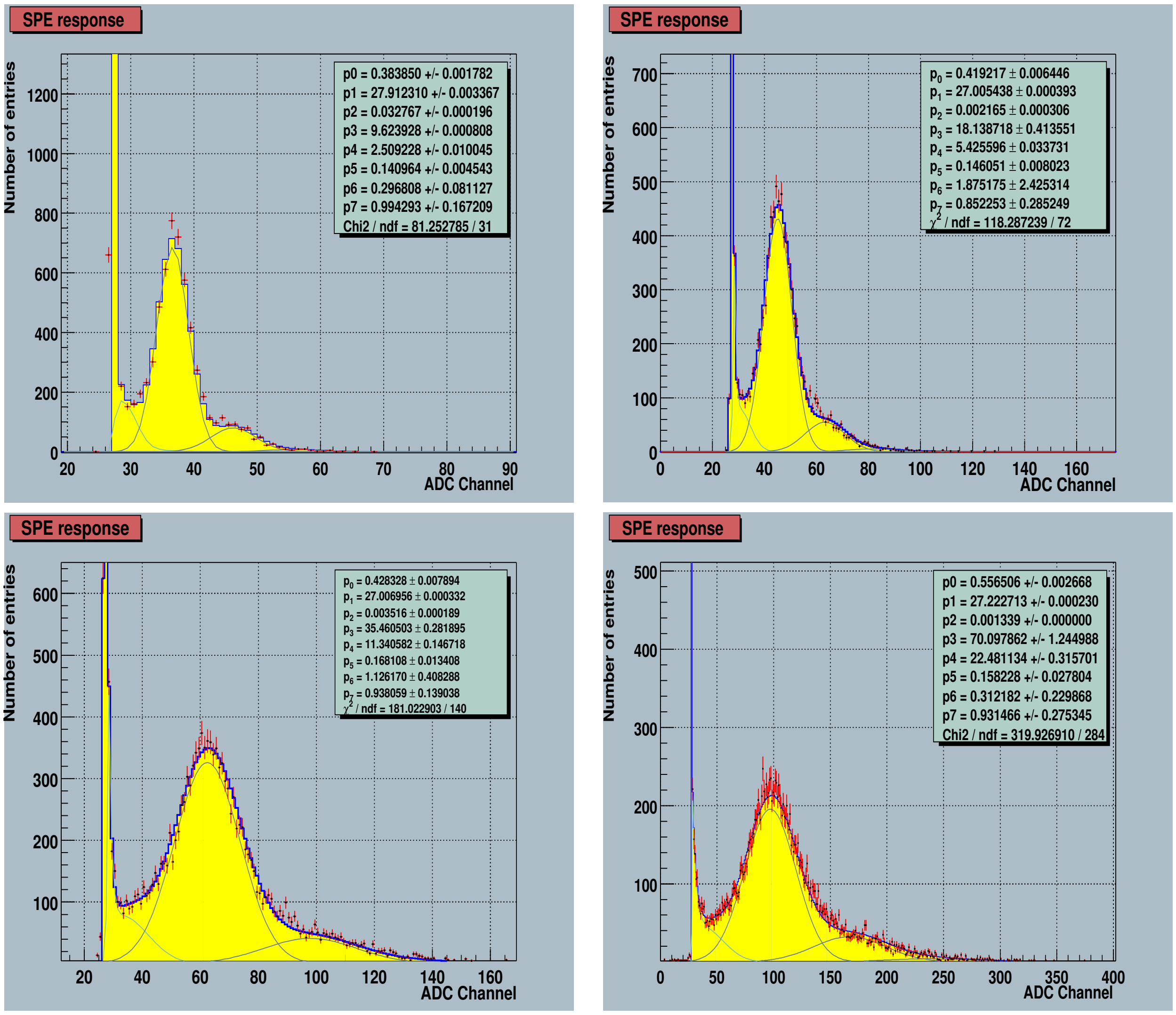

Figure 3.5: Charge spectra for several voltages for the photomultiplier Hamamatsu AF0174. From left to right and from up to bottom: 1600 V, 1800 V, 2000 V and 2200 V.

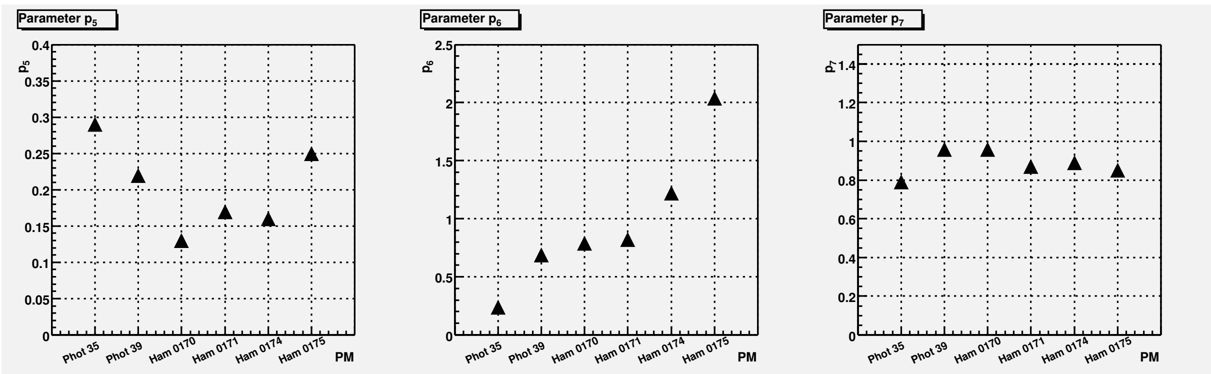

Figure 3.6: Value of the parameters p_5, p_6 and p_7 for all the photomultipliers.

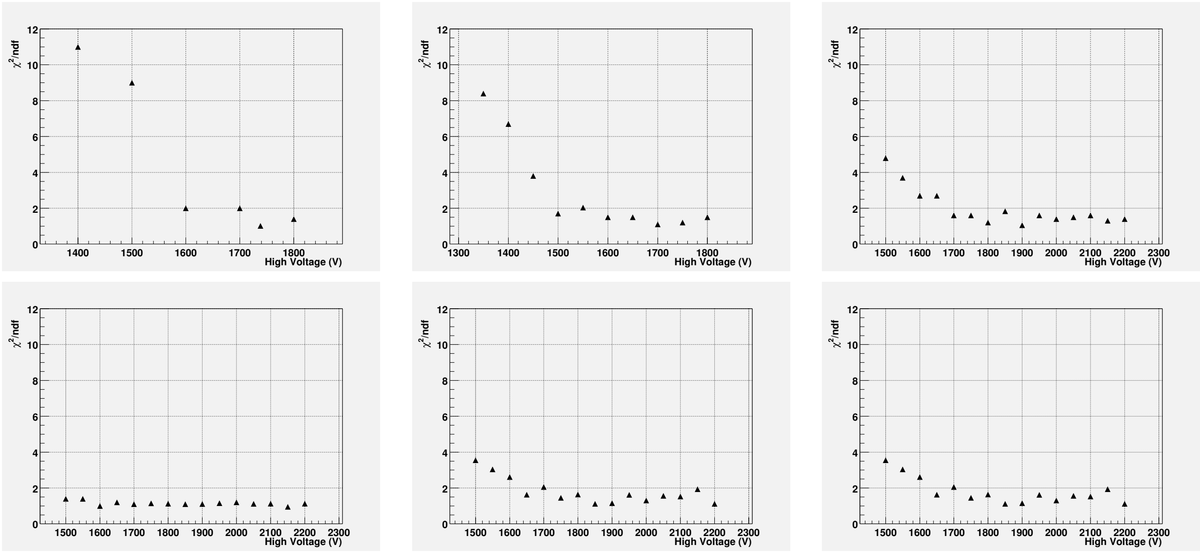

Figure 3.7: χ^2/ndf dependence on voltage. From left to right and from up to bottom: Photonis 35 and 39 and Hamamatsu AF0170, AF0171, AF0174 and AF0175.

3.2 Gain

The gain is obtained from the position of the SPE peak, as given by the parameter p_3. This value, which is the channel number, has to be converted into charge in terms of electron charge units:

$$Gain = \frac{p_3 \cdot 0.25\ pC/channel}{1.602 \times 10^{-7} pC} \tag{3.7}$$

Figures 3.8 and 3.9 show the dependence of gain on high voltage. These curves have been fitted to the product of an exponential and a parabola. The basic behaviour is exponential and deviations from it are taken into account by means of the parabola. From these plots, the nominal voltage, i.e. the voltage at which the gain is 5×10^7, can be determined:

$$Gain(HV) = \exp[k_0 + k_1 \cdot HV] \cdot [k_2 \cdot (HV)^2 + k_3 \cdot HV + k_4] \tag{3.8}$$

In the case of the Photonis photomultipliers, the behaviour of the two curves show some differences. The shape of the Photonis 35 curve is closer to an exponential than that of the Photonis 39. On the other hand, the gain of Photonis 39 is higher, so its nominal voltage is smaller.

The gain curves of the Hamamatsu photomultipliers are more similar among them, but there are still differences in the nominal voltages.

In Table 3.1, all the parameters of the fits are shown. Two parameters are specially relevant. First, k_1 is the slope of the exponential, so it gives the increase of the gain with the voltage. On the other hand, a high value in k_2 indicates a clear deviation from the ideal behaviour. In Table 3.2, the nominal voltage values are shown.

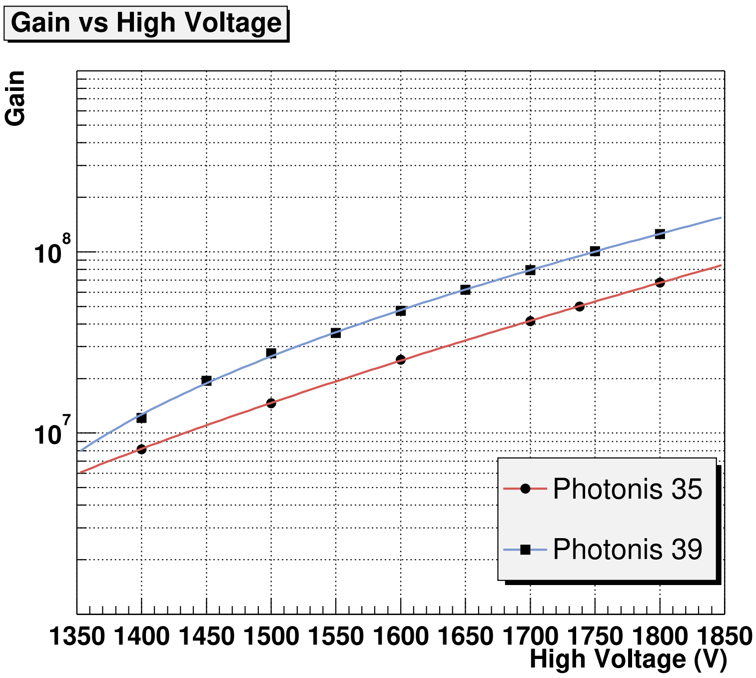

Figure 3.8: Gain curve as a function of high voltage for the Photonis photomultipliers.

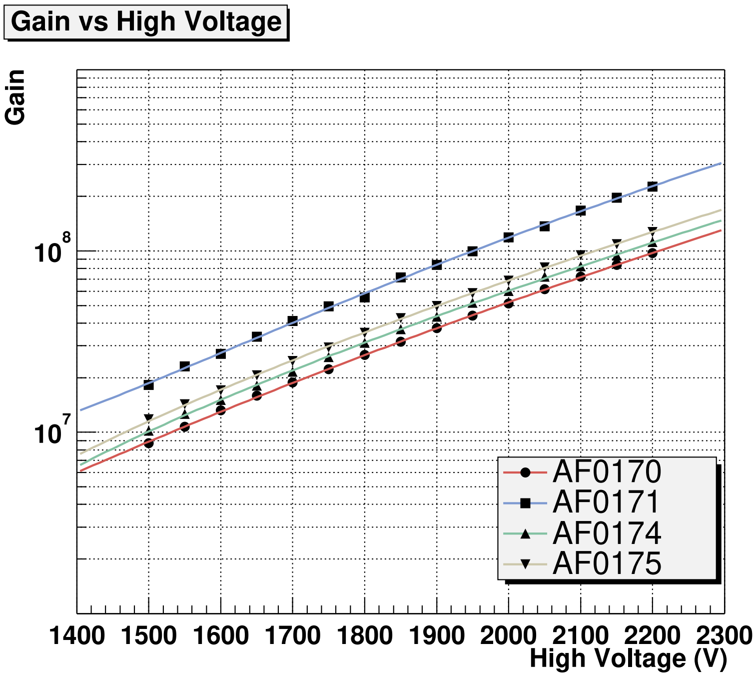

Figure 3.9: Gain as a function of high voltage for the Hamamatsu photomultipliers.

Serial Number	k_0	k_1 ($\times 10^{-3}$)	k_2 ($\times 10^6$)	k_3 ($\times 10^3$)	k_4	χ^2/ndf
Phot 35	-5.45 ± 0.07	3.13 ± 0.03	-32 ± 2	8.1 ± 1.7	22.7 ± 1.6	1.1
Phot 39	-3.26 ± 0.06	2.36 ± 0.03	-46 ± 2	6.1 ± 1.1	25.3 ± 0.7	1.3
Ham AF0170	-2.82 ± 0.09	2.01 ± 0.04	-5.2 ± 0.2	2.0 ± 0.5	4.3 ± 0.3	0.9
Ham AF0171	-4.18 ± 0.09	2.51 ± 0.04	-7.8 ± 0.2	6.5 ± 1.7	11.1 ± 1.2	1.0
Ham AF0174	-2.89 ± 0.02	2.03 ± 0.09	-6.1 ± 1.3	2.3 ± 1.4	5.0 ± 0.9	1.2
Ham AF0175	-3.55 ± 0.02	2.29 ± 0.09	-4.8 ± 1.2	3.2 ± 1.3	5.9 ± 1.3	1.1

Table 3.1: Parameters of the gain fit.

Serial Number	Nominal Voltage (V)
Phot 35	1738 ± 5
Phot 39	1615 ± 5
Ham AF0170	1995 ± 5
Ham AF0171	1757 ± 5
Ham AF0174	1941 ± 5
Ham AF0175	1918 ± 5

Table 3.2: Nominal voltages for the different photomultipliers.

3.3 Amplitude

The amplitude spectrum is closely related to the charge spectrum, since relationship between the charge and the amplitude of a pulse is expected.

The experimental setup to determine the amplitude can be seen in Figure 3.10. It is similar to that used in the measurement of the charge spectrum but the acquisition is performed by the oscilloscope, which sends the result to the PC. In Figure 3.11, a typical amplitude spectrum can be seen.

The fitting procedure is simpler than in the previous case. The SPE peak is fitted to a Gaussian, whose mean is the amplitude. Figures 3.12 and 3.13 show the dependence of the amplitude on the voltage.

A summary of the amplitudes of all the photomultipliers at the nominal voltage can be seen in Table 3.3. The Photonis PMT amplitudes are higher than those of Hamamatsu.

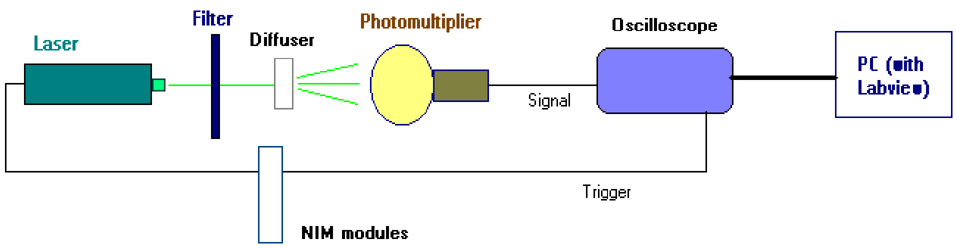

Figure 3.10: Experimental setup to measure the amplitude spectrum.

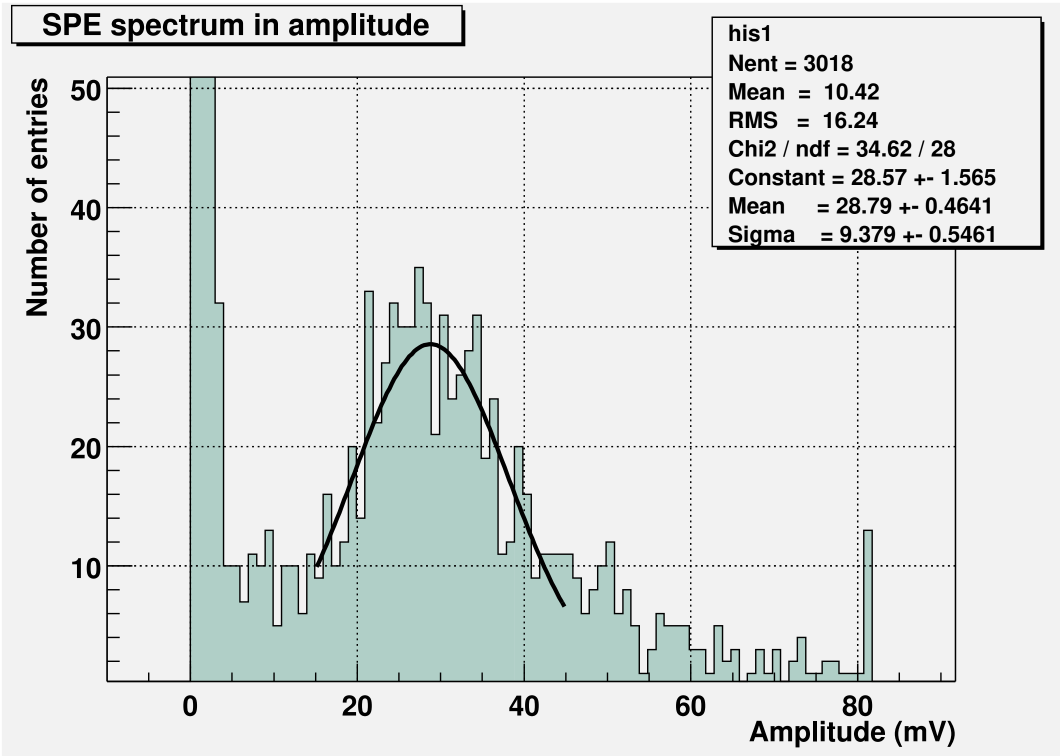

Figure 3.11: Example of amplitude spectrum.

It is also interesting to plot the relationship between amplitude and gain. These curves are expected to be similar for the same model of photomultiplier, since they are related to the pulse shape and thus to the dynode structure of the photomultiplier. They are shown in Figures 3.14 and 3.15. The behaviour of the curves is nearly the same when comparing the tubes of the same model, specially in the case of the Hamamatsu PMTs. The increase of amplitud with voltage is faster for the Photonis PMTs.

In all cases, this dependence is almost linear. The deviation from linearity has to do with the differences in pulse shape. It is important to note that in the actual ANTARES experiment, signals will be discriminated on the basis of amplitude.

Serial Number	Nominal Amplitude
Phot 35	60.2 ± 1.3 mV
Phot 39	62.5 ± 0.8 mV
Ham AF0170	33.2 ± 1.2 mV
Ham AF0171	30.5 ± 1.2 mV
Ham AF0174	34.3 ± 0.5 mV
Ham AF0175	35.8 ± 0.7 mV

Table 3.3: Amplitude at nominal voltage for the different photomultipliers.

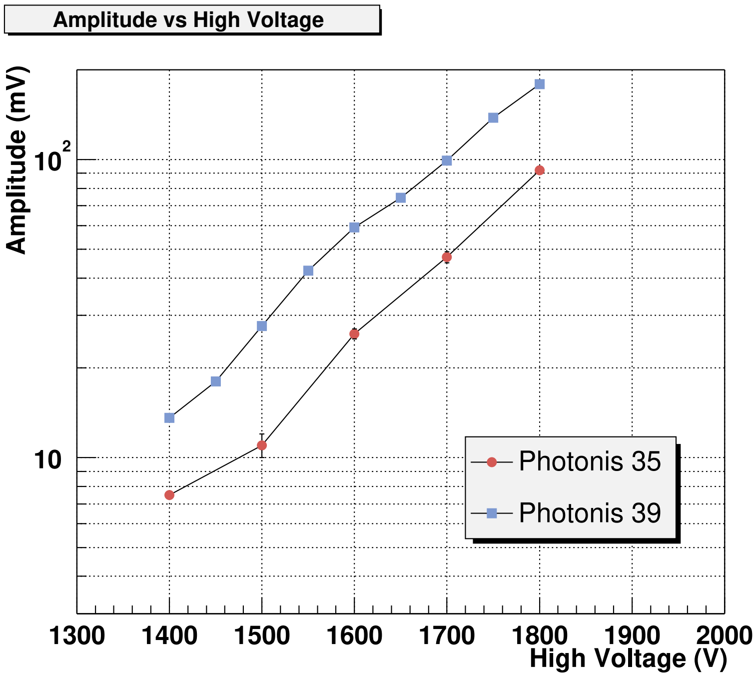

Figure 3.12: Amplitude dependence on voltage for the Photonis photomultipliers.

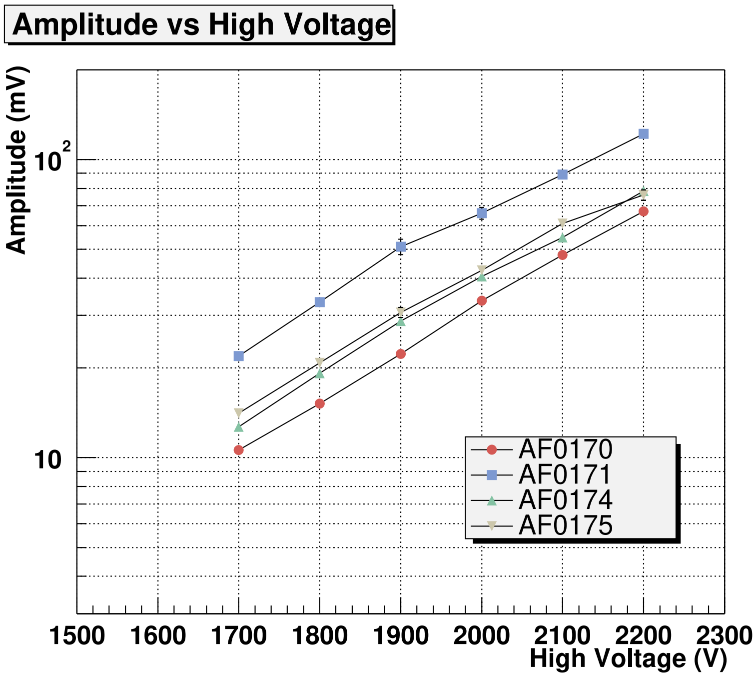

Figure 3.13: Amplitude dependence on voltage for the Hamamatsu photomultipliers.

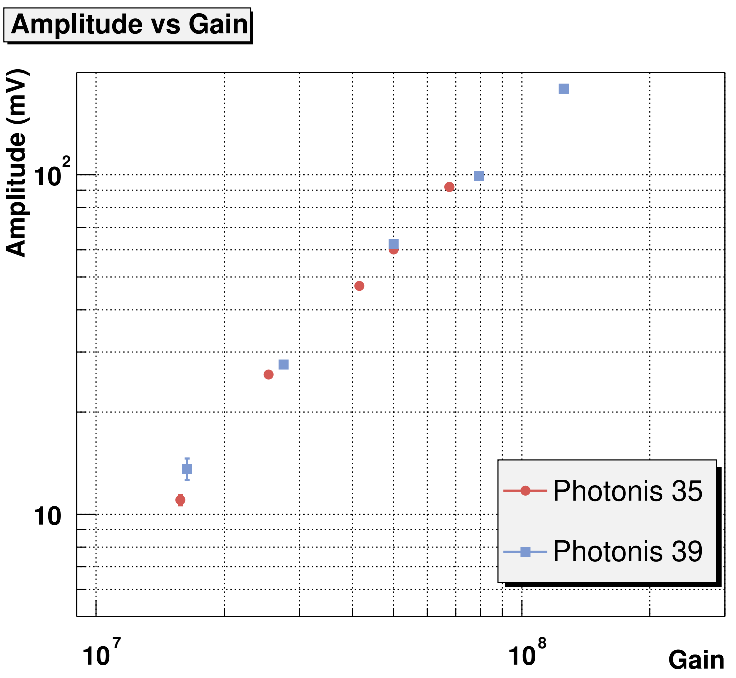

Figure 3.14: Relationship between amplitude and gain for the Photonis photomultipliers.

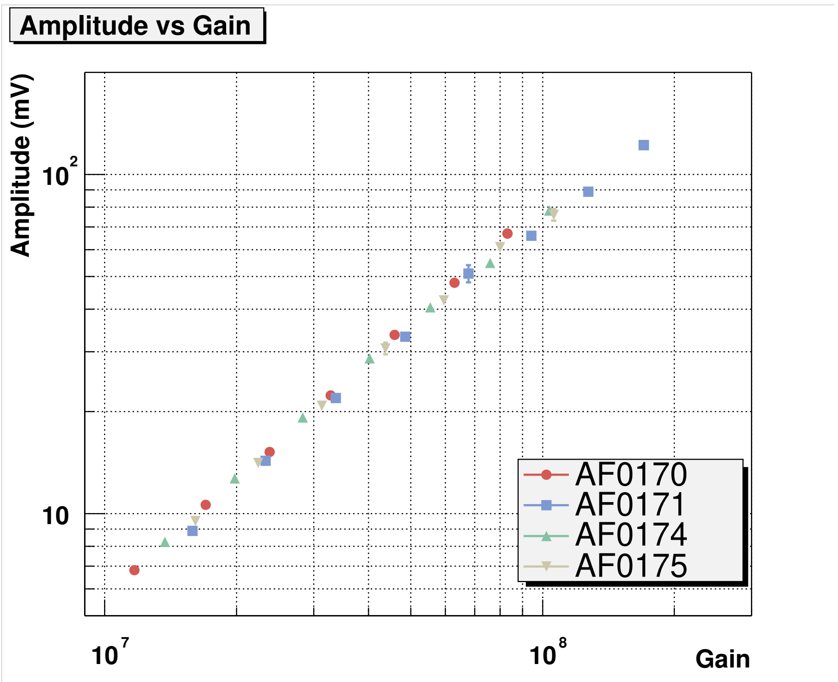

Figure 3.15: Relationship between amplitude and gain for the Hamamatsu photomultipliers.

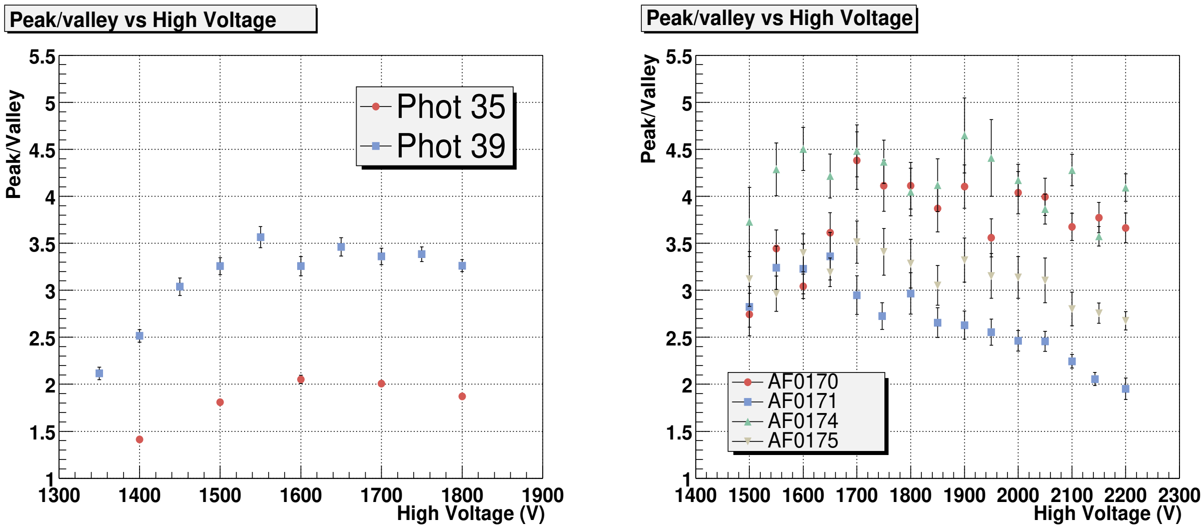

Figure 3.16: Peak to valley ratio for the Photonis (left) and for the Hamamatsu (right) photomultipliers.

Serial Number	Peak to Valley
Phot 35	1.8 ± 0.1
Phot 39	3.5 ± 0.1
Ham AF0170	4.2 ± 0.2
Ham AF0171	2.9 ± 0.2
Ham AF0174	4.1 ± 0.3
Ham AF0175	3.4 ± 0.2

Table 3.4: Peak to valley ratio at nominal voltage.

3.4 Peak to Valley Ratio

The ratio between the height of the SPE peak and the valley is an important magnitude since it can be used to estimate the capability of the photomultiplier to discriminate the number of photoelectrons in an event. As it was seen in Section 2.5, the value according to the ANTARES specifications should be larger than 2. Figure 3.16 shows the results.

Concerning the Photonis photomultipliers, it can be seen that the shape of both curves is similar. It grows with voltage up to the region around the nominal voltage and then becomes stable. However, there is an important difference in the value. Photonis 35 has a low peak/valley (below 2), whereas the value of Photonis 39 is clearly above 3. This points again to a manufacturing difference between these tubes.

On the other hand, the peak/valley ratio of all the Hamamatsu photomultipliers is in general above the specifications. It also becomes stable near the nominal voltage. For very low or very high voltages, the peak/valley ratio decreases. In Table 3.4 these results are summarized.

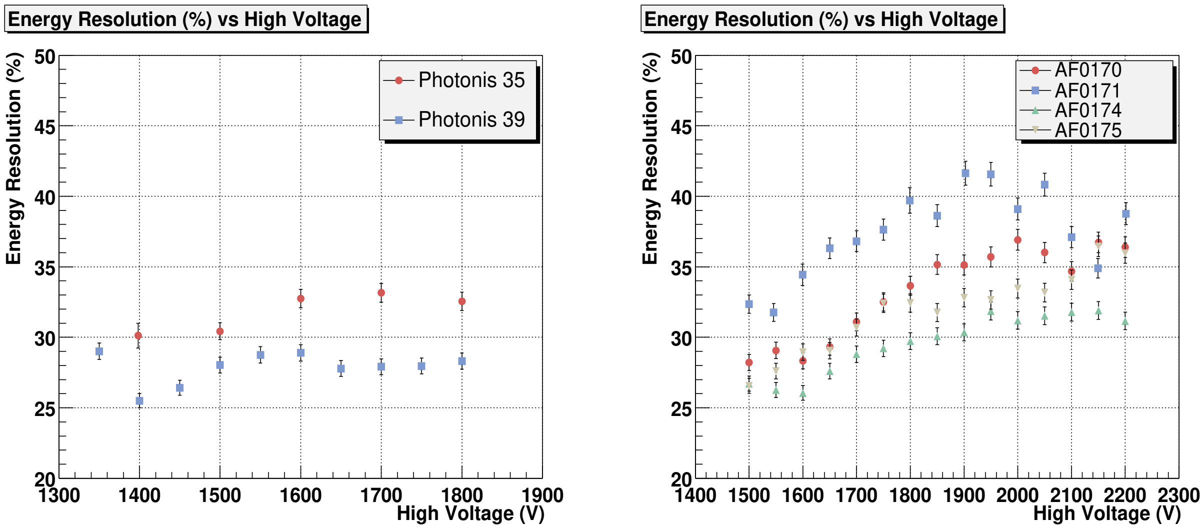

Figure 3.17: Energy resolution of the Photonis (left) and Hamamatsu (right) photomultipliers.

Serial Number	Energy Resolution (%)
Phot 35	33 ± 2
Phot 39	29 ± 2
Ham AF0170	36 ± 2
Ham AF0171	37 ± 2
Ham AF0174	32 ± 2
Ham AF0175	32 ± 2

Table 3.5: Energy resolution at the nominal voltage.

3.5 Energy resolution

Energy resolution (the ratio of $\sigma_{1\ pe}$ to $\mu_{1\ pe}$) is a useful parameter to estimate the fluctuations in charge of the SPE events. The results are shown in Figure 3.17.

In this case, the differences between the tubes are not very large. There is a slow increase of the energy resolution with voltage and it becomes stable near the nominal voltage. At this point energy resolution is in general over 30%, except for Photonis 39. Table 3.5 shows the energy resolution at the nominal voltage.

3.6 Transit time spread

3.6.1 Experimental setup

Transit time spread is a key parameter in the ANTARES experiment, as it has been explained in Section 1.3.4. Therefore, it is very important to measure it with high accuracy. The experimental setup used to do this end is shown in Figure 3.18.

The laser illuminates the photomultiplier, whose output is discriminated in order to build the

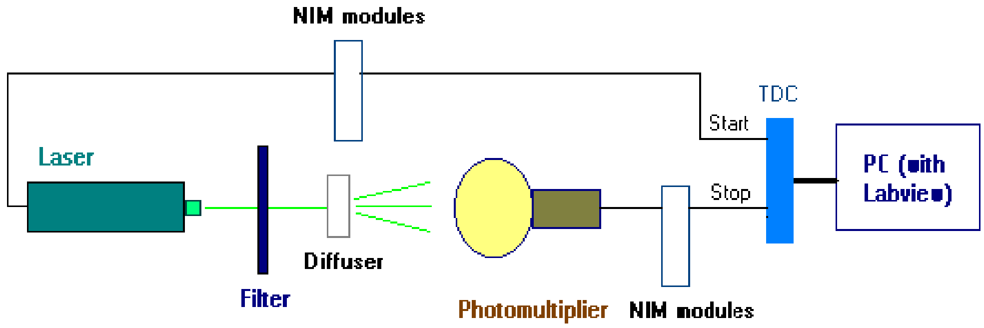

Figure 3.18: Experimental setup to measure TTS.

STOP signal for the TDC. The START signal is given by the internal photodiode, whose output has to be inverted and discriminated.

Two remarks have to be made. On one hand, it is important that the level of illumination be lower than one photoelectron. This is to avoid as much as possible the coincidence of two or more photons that would decrease the measured value of the TTS by a factor $\sqrt{n}$, where n is the number of photoelectrons. Typically, we attenuate the light to a level of around 0.3 photoelectrons.

Another important point is the discrimination threshold for the photomultiplier signal. The higher the threshold, the lower the value obtained for the TTS, since pulses below the threshold are rejected, so they do not contribute to the dispersion. The threshold selects similar pulses. We have discriminated over one half of the amplitude of a SPE event.

3.6.2 Results

Two typical time distributions are shown in Figure 3.19 for a Photonis (left) and a Hamamatsu (right) tube.

Both distributions seem to be asymmetric, especially the Photonis curve. In order to establish a valid criterion to calculate the TTS, several options were considered. The first idea was to fit the upper part of the distribution to a Gaussian, but the dependence on the fit limits was too strong, so it is necessary to find a function which fits the whole range. A Landau distribution was tried, but the results were clearly not satisfactory. Finally, a fit to the convolution of a Gaussian and an exponential:

$$f(t) = p_3 \cdot \frac{1}{\sqrt{2\pi} p_1} \cdot exp(\frac{-(t-p_0)^2}{2p_1^2}) \otimes exp(-p_2 t) \tag{3.9}$$

This fit (see Figure 3.19) works properly, giving a good value of χ^2. The TTS obtained from this distribution has three components, as it is indicated in Equation 3.10:

$$\mathrm{FWHM}^2_{tot} = \mathrm{FWHM}^2_{PMT} + \mathrm{FWHM}^2_{laser} + \mathrm{FWHM}^2_{elec} \tag{3.10}$$

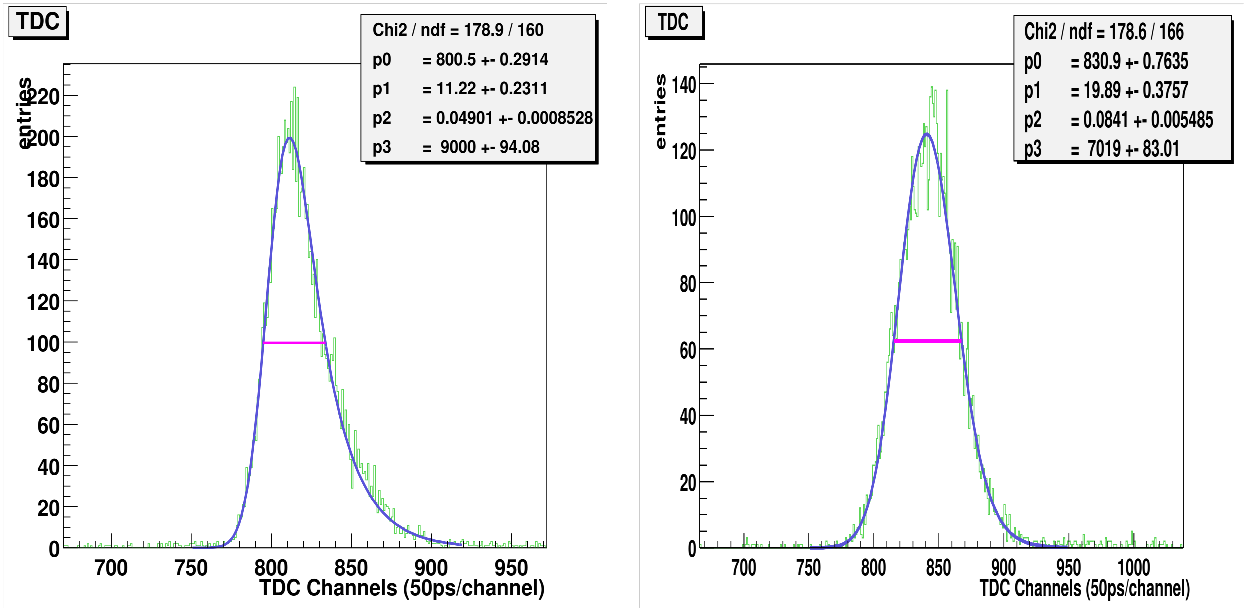

Figure 3.19: Two examples of transit time distributions. Left: Photonis 39; Right: Hamamatsu AF0170.

- FWHM_{PMT}: The intrinsic TTS of the photomultiplier. This is the magnitude we are interested in and will be extracted substracting the two remaining components.

- FWHM_{laser}: The width of the laser pulse.

- FWHM_{elec}: The contribution from the electronics.

In order to subtract the two last terms, a very fast photomultiplier was used. The TTS of this photomultiplier (model R5496) has been calibrated by Hamamatsu. The value they obtain is $\text{FWHM}_{fast\ PMT} = 0.23 \pm 0.01$ ns. Measuring the total width of the distribution obtained by illuminating the fast photomultiplier using the same experimental setup, it is possible to calculate the effect of the source and the electronics. Notice that even if the value given by Hamamatsu for the TTS of the tube is not exact, a reasonable deviation from it would not be important, since it is small and the terms contribute quadratically. Assuming a FWHM of the laser of 0.5 ± 0.1 ns, systematics can contribute to the error up to 0.1 ns. The value of the TTS not due to the PMT is 0.65 ± 0.05 ns, i.e. of the order of what we expected. Figure 3.20 shows an example of the time distributions with the fast photomultiplier alone.

The dependence of the TTS on the high voltage in the case of the Photonis photomultipliers is shown in Figure 3.21. As it is expected, there is a decrease in the TTS with voltage. This decrease is particularly fast for the Photonis 35. At the nominal voltage, the TTS is 1.8 and 2.1 ns, for Photonis 35 and 39, respectively.

Concerning the Hamamatsu photomultipliers (see Figure 3.22), the decrease rate with voltage is similar to the previous case, but the distributions are wider ($\sim$2.6 ns at the nominal voltage). Nevertheless, they are within the ANTARES specifications.

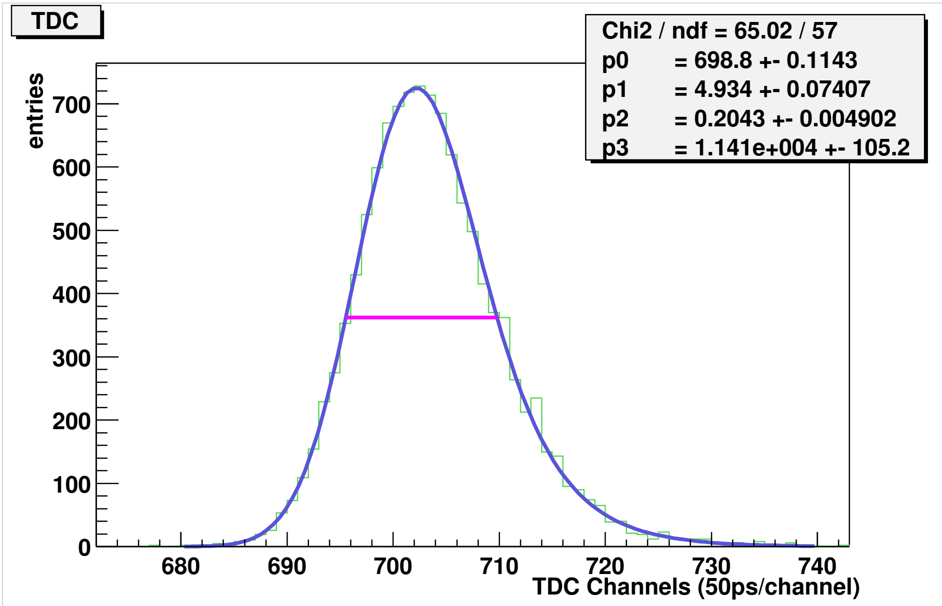

Figure 3.20: Time distribution obtained for a Hamamatsu R5496 photomultipier.

Serial Number	TTS
Phot 35	1.8 ± 0.1 ns
Phot 39	2.1 ± 0.1 ns
Ham AF0170	2.5 ± 0.1 ns
Ham AF0171	2.7 ± 0.1 ns
Ham AF0174	2.6 ± 0.1 ns
Ham AF0175	2.6 ± 0.1 ns

Table 3.6: Transit time spread at the nominal voltage.

In Table 3.6 the FWHM at the nominal voltage for all the photomultipliers is shown. As in the case of the charge spectrum, the errors given by the fit are much smaller than those due to fluctuations in the experimental conditions, so an estimation of the latter is used by repeating the measurements. The best values of TTS are obtained for Photonis PMTs. However, both models are within the specifications.

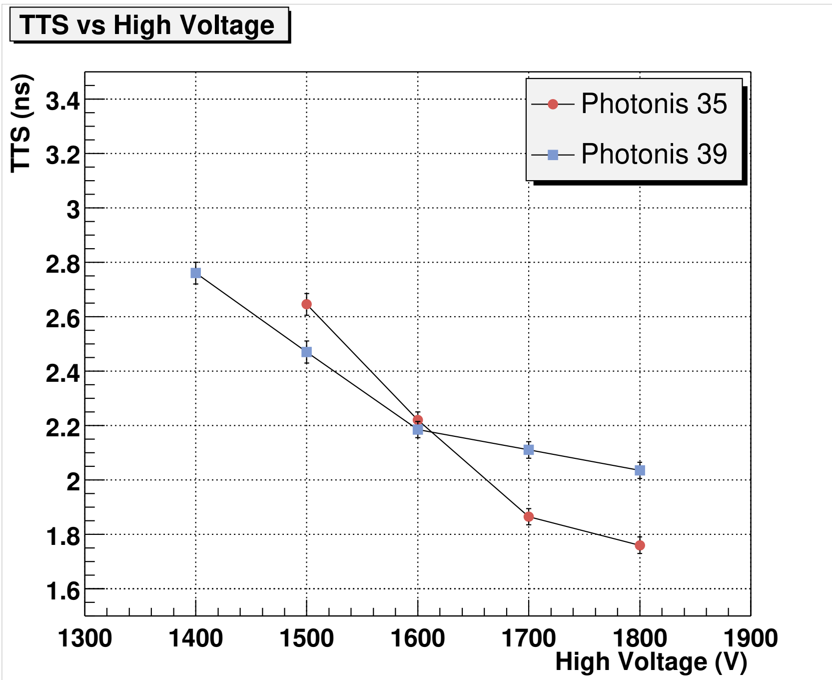

Figure 3.21: TTS dependence on voltage for the Photonis photomultipliers.

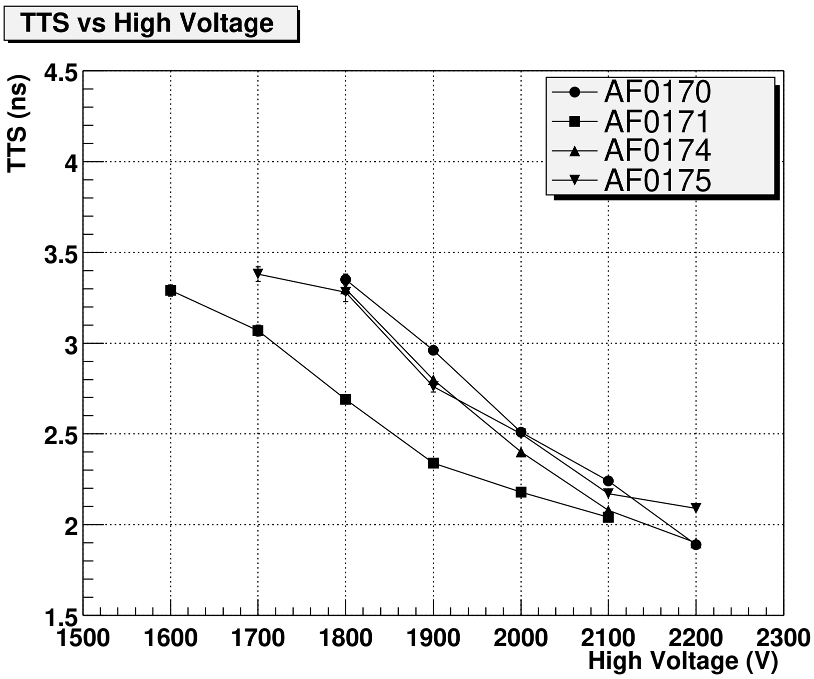

Figure 3.22: TTS dependence on voltage for the Hamamatsu photomultipliers.

3.7 Dark current

In principle, dark current is not a critical parameter in our experiment, since noise coming from ^{40}K is expected to be much higher than other internal sources of dark current.

The experimental setup for the measurement of the dark current is shown in Figure 3.23. The output from the photomultiplier is sent to a Linear Fan In / Fan Out module, from where four signals identical to the input signal are sent to four amplitude discriminators. The number of pulses above each threshold is counted.

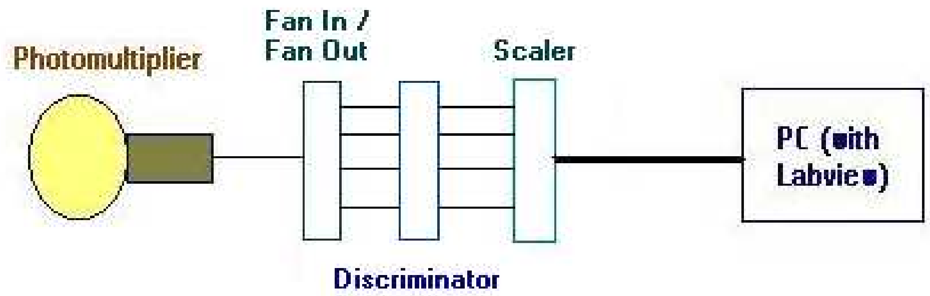

Figure 3.23: Experimental setup to measure dark current rates.

Each discriminator uses a different threshold. This threshold is established in terms of the number of photoelectrons in amplitude, for the sake of a better comparison among the tubes.

3.7.1 Dependence on high voltage

The first analysis made is the dependence on high voltage. The results are plotted in Figures 3.24 and 3.25, where the dark current rate for a threshold of half a photoelectron is shown.

There is a smooth increase with voltage in all the tubes. However, whereas this increase is faster at low voltages for the Photonis PMTs, the contrary occurs for the Hamamatsu PMTs.

3.7.2 Dependence on threshold

There is another interesting way to plot these results. The dependence on the threshold at the nominal voltage can be studied as it is shown in Figures 3.26 and 3.27.

These curves have clearly two parts. Around the region of one photoelectron, the variation is stronger than for thresholds larger than two photoelectrons. This is the expected behaviour, since in our operating conditions, the main source of dark current is the thermionic effect, which produces basically SPE pulses.

There are some differences between the two PMT models. The Photonis photomultipliers present a lower rate of dark noise than those of Hamamatsu. Moreover, the change around the SPE threshold is faster in the Photonis model than in the Hamamatsu one.

When comparing tubes of the same model, we can see that the behaviour of Photonis 35 and 39 is similar. The behaviour of Hamamatsu PMTs is also similar but the magnitud of dark current clusters in pairs.

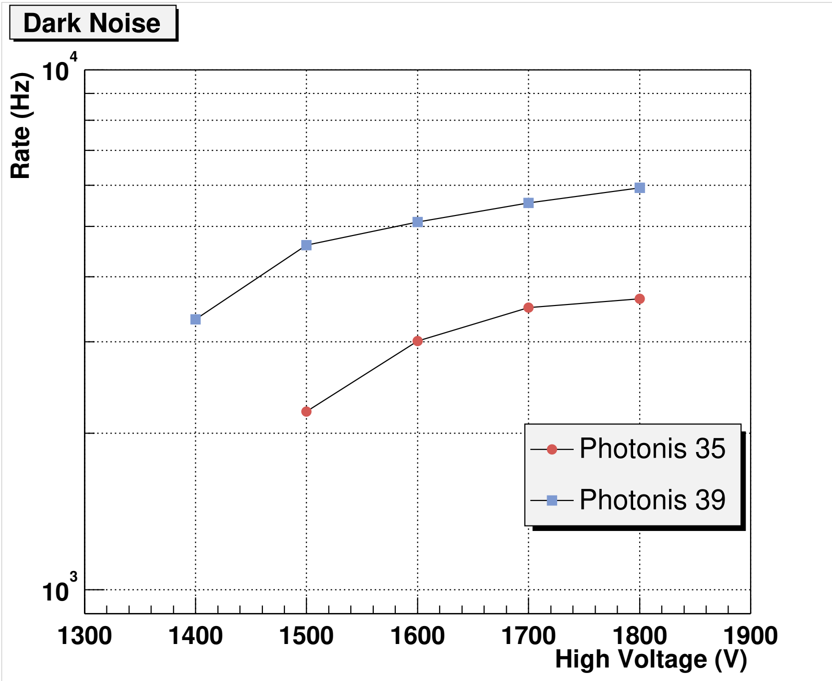

Figure 3.24: Dark noise as a function of voltage for the Photonis photomultipliers. A threshold of half a photoelectron has been used.

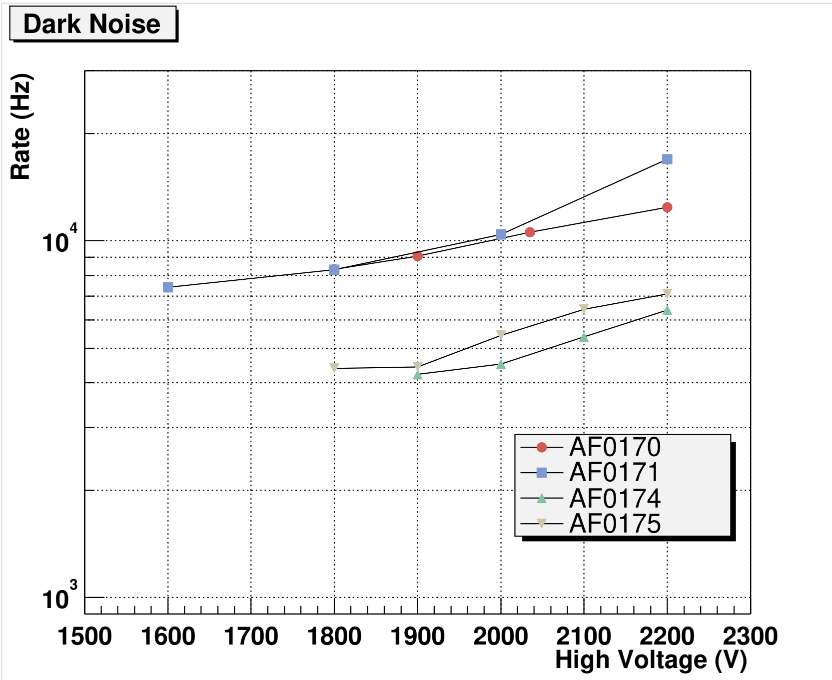

Figure 3.25: Dark noise dependence on voltage for the Hamamatsu photomultipliers. A threshold of half a photoelectron has been used.

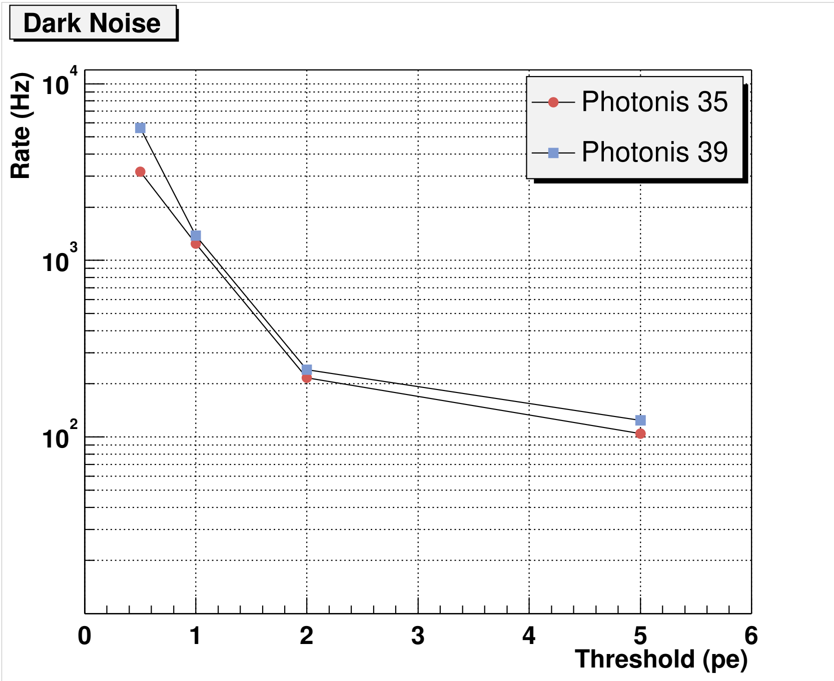

Figure 3.26: Dark noise dependence on threshold for the Photonis photomultipliers at the nominal voltage.

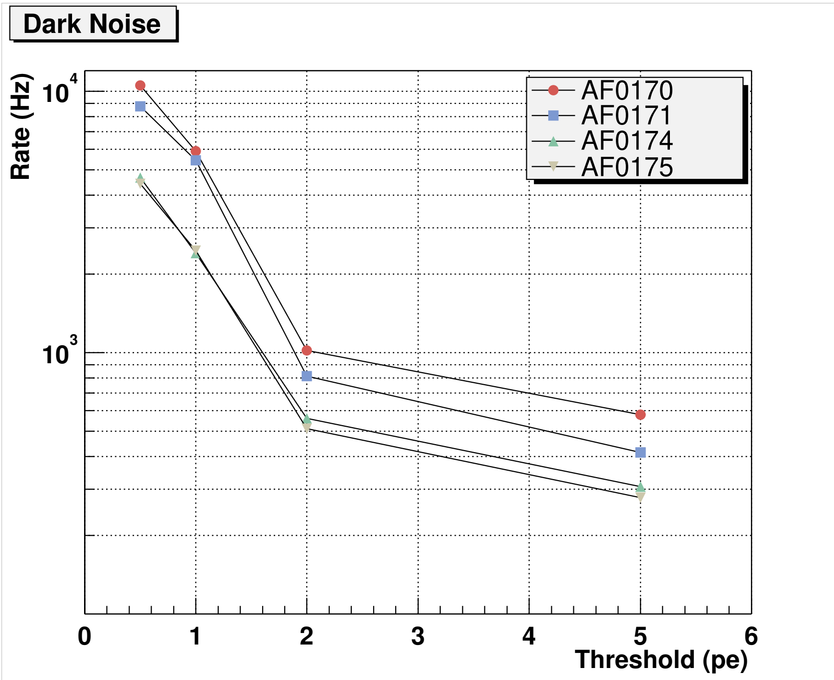

Figure 3.27: Dark noise dependence on threshold of the Hamamatsu photomultipliers at the nominal voltage.

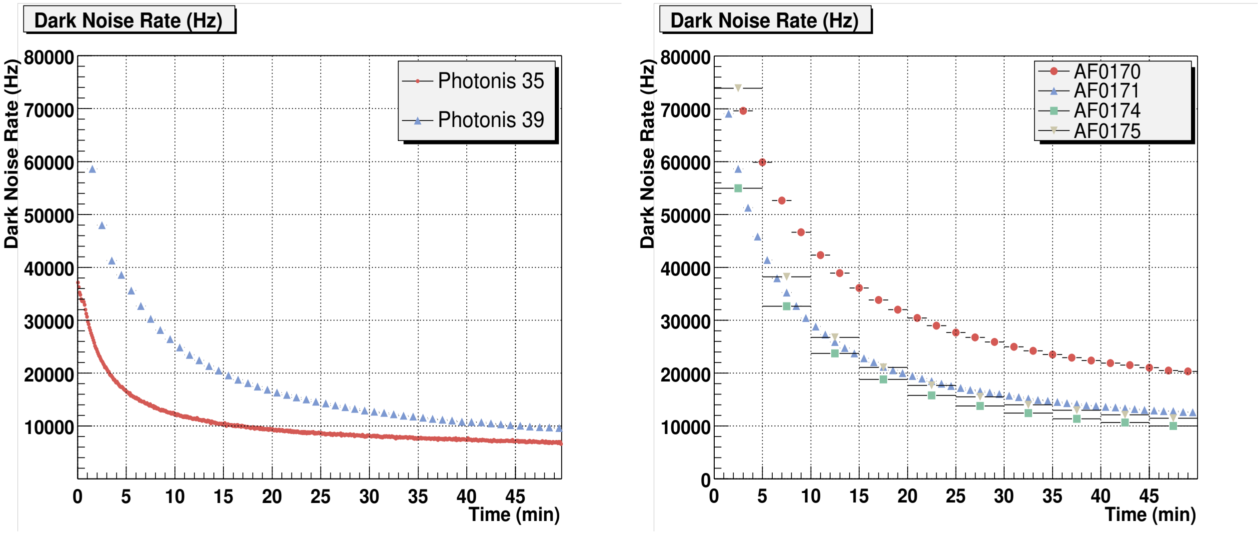

Figure 3.28: Dark noise evolution after exposure for Photonis (left) and Hamamatsu (right) photomultipliers.

3.7.3 Dark noise evolution after exposure

The last test related to the dark current rate is the study of its evolution in time after exposing them to the environmental light of the laboratory with the HV turned off. There are two reasons for that. Firstly, because the photomultipliers will be exposed to the sun light when the lines will be deployed. It is difficult to estimate if the light intensity in both situations is similar, but large differences are not expected. On the other hand, the global time calibration of the detector by the optical beacons will mean an exposure to a high intensity yield. Therefore, it is necessary to study the effect on the photomultipliers. In particular, one of the magnitudes more sensitive to the light exposure is the dark current.

After exposing the photomultiplier during ten minutes to the environmental light, it is put back into the dark box and dark noise rates are measured as usual.

Figure 3.28 shows the evolution with time of all the photomultipliers. In the case of Photonis, a clear difference exists between both tubes. Concerning Hamamatsu photomultipliers, the behaviour is similar for all of them except for AF0170, whose evolution is slower.

The values that we have obtained indicate that, in general, stabilization is reached very soon. After one hour, the dark noise rate decreases to twice the final rate.

3.8 Afterpulses

As it has been mentioned, it is important to control afterpulsing since it can cause misreconstruction problems and affect the data flow rate. In this section, four kind of events are analyzed:

- **Prepulses**: Pulses which occur 10–80 ns before the main pulse window. The main pulse window is the time interval within ±10 ns around the expected arrival time. They are not associated with a primary pulse. They are most probably produced when a photon is absorbed in the first dynode instead of the photocathode.

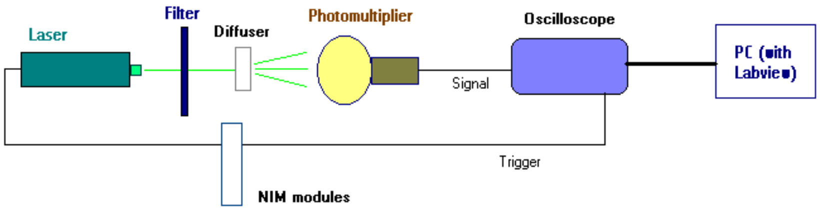

Figure 3.29: Experimental setup to measure afterpulse rates.

- **Delayed pulses**: Pulses arriving 10–80 ns after the main pulse window. They are not associated with a primary pulse. They are most likely produced when a photoelectron released in the photocathode is intercepted and reflected by the potential grid before reaching the first dynode.
- **Afterpulses-1**: Afterpulses which arrive 10–80 ns after the main pulse window. They are secondary pulses. The cause of these pulses are photons radiated by the last dynodes which reach the photocathode.
- **Afterpulses-2**: Pulses occurring 80 ns–16 μs after the main pulse window. They are secondary pulses. They are caused by ionised residual gas atoms accelerated back to the photocathode.

3.8.1 Experimental setup

The experimental setup used to measure afterpulse rate is shown in Figure 3.29. The photomultiplier is illuminated with a low level of light ($\sim$0.4 pe). Its signal is sent to the oscilloscope, which is triggered by the internal photodiode of the laser. The oscilloscope digitizes the output from the PMT and sends it to the PC, where a LabView program finds the peaks in the waveform. There are differences in the measurement procedure between the case of prepulses, delayed pulses and afterpulses-1 and the case of afterpulses-2. The time scale used in the first case is 0.2 ns/channel which allows to cover $\pm$200 ns around the main pulse window. On the other hand, the scale to measure afterpulses-2 is 10 ns/channel, i.e. the region from –4 to 16 μs with respect to the main pulse window. In this case, the signal from the photomultiplier is too narrow to be detected by the oscilloscope, so it is necessary to use a discriminator. With this method, however, the amplitude information is lost.

3.8.2 Results

3.8.2.1 Prepulses, delayed pulses and afterpulses-1

The acquisition program looks on-line for peaks in the waveform digitized by the oscilloscope and stores the position and amplitude information. The analysis program uses this information to calculate the afterpulse rates. This analysis program takes into account the effect of the dark current, which is substracted. The trigger of the oscilloscope is forced to locate the main pulse peak near the middle of the scale to allow the simultaneous analysis of prepulses, delayed pulses and afterpulses-1.

- **Photonis**

  The histogram with the information relative to the position of all the pulses detected by the acquisition program is shown in Figures 3.30 and 3.31 (left). A clear difference between Photonis 35 and 39 can be seen. In the latter case, a peak appears 40 ns after the main pulse window. In the plot to the right we show the pulses not associated with a primary pulse in the window. These are the delayed pulses. The delayed pulse plots have been obtained in anticoincidence with pulses in the main pulse window. Most of the pulses which are in the delayed pulse window of Photonis 35 seem to be primary pulses. In this case, the peak in the distribution correspondig to the main pulses is very wide. The prepulse rate is low in both cases.

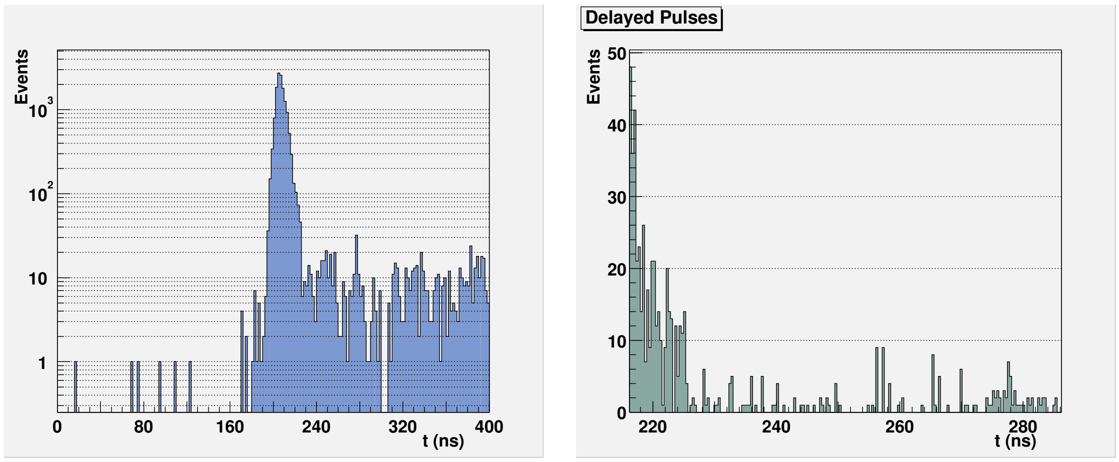

Figure 3.30: Left: Time distribution of all the pulses detected. Right: Time distribution of the delayed pulses for the Photonis 35 PMT.

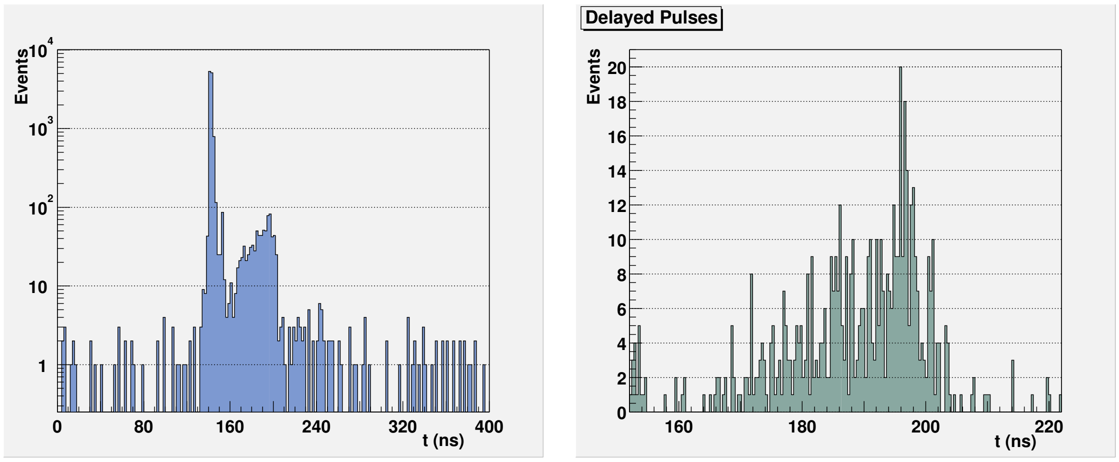

Figure 3.31: Left: Time distribution of all the pulses detected. Right: Time distribution of the delayed pulses for the Photonis 39 PMT.

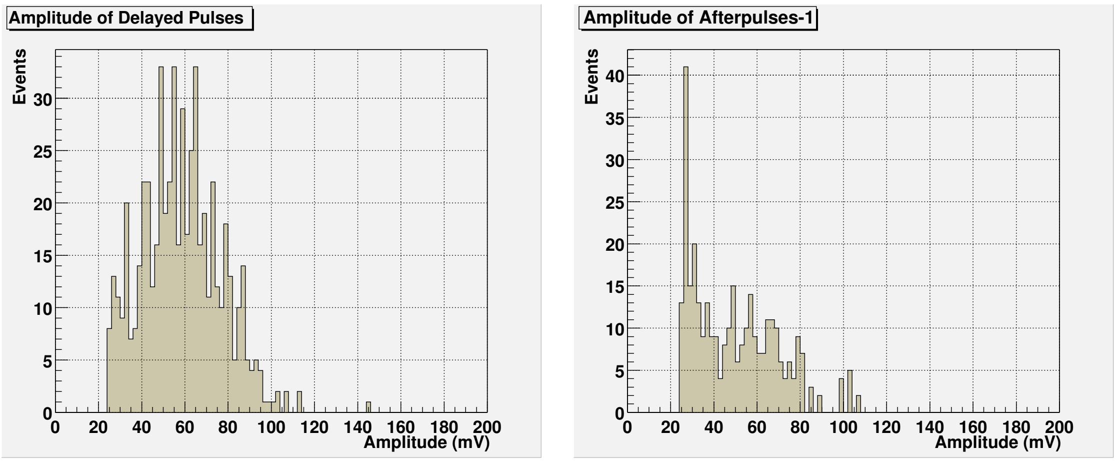

Figure 3.32: Amplitude distributions of delayed pulses (left) and afterpulses-1 (right) for Photonis 39.

As an example of Photonis amplitude spectrum for afterpulses, in Figure 3.32 both delayed and afterpulse-1 distributions are shown. Delayed pulse amplitudes are larger than those of afterpulses-1.

- **Hamamatsu**

  Figures 3.33-3.36 show the time distribution of all (left) and only delayed (right) pulses. The major difference among these tubes is in the prepulses rate. A peak in the prepulses region appears for Hamamatsu AF0174 and AF0175, but not for AF0170 and AF0171. On the other hand, there are no great difference in the delayed pulses window.

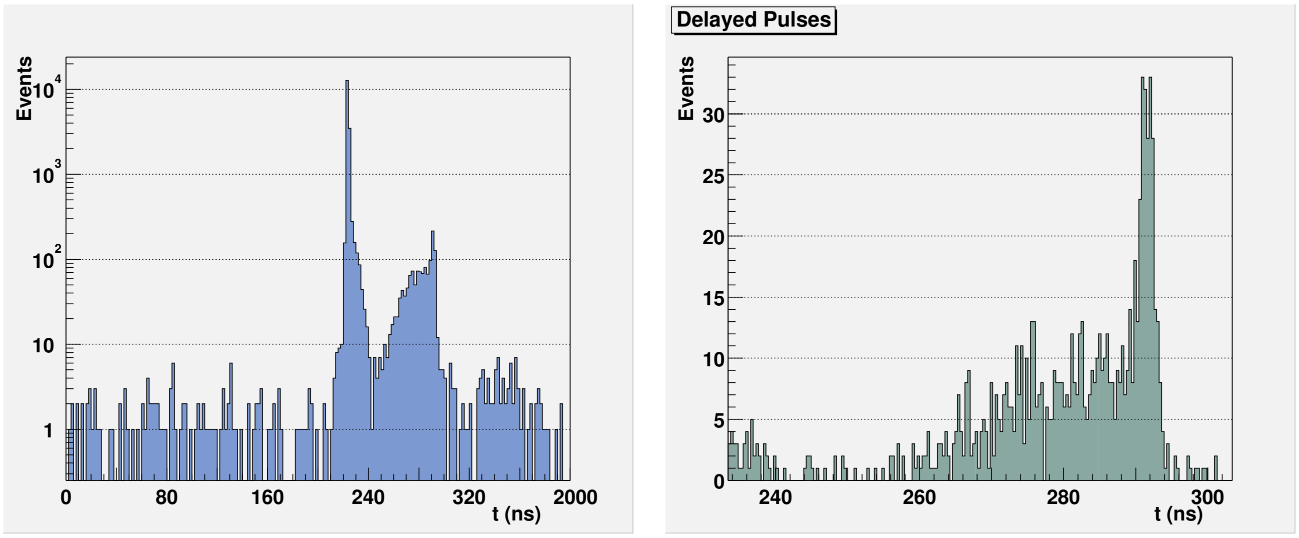

Figure 3.33: Left: Time distribution of all the pulses detected. Right: Time distribution of the delayed pulses for the Hamamatsu AF0170 PMT.

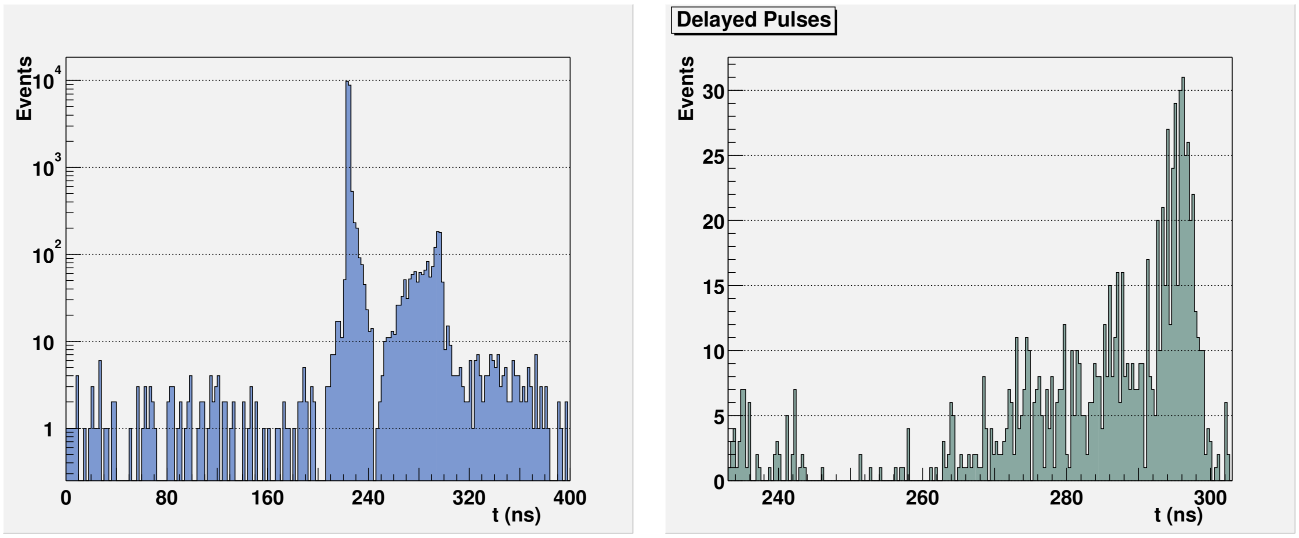

Figure 3.34: Left: Time distribution of all the pulses detected. Right: Time distribution of the delayed pulses for the Hamamatsu AF0171 PMT.

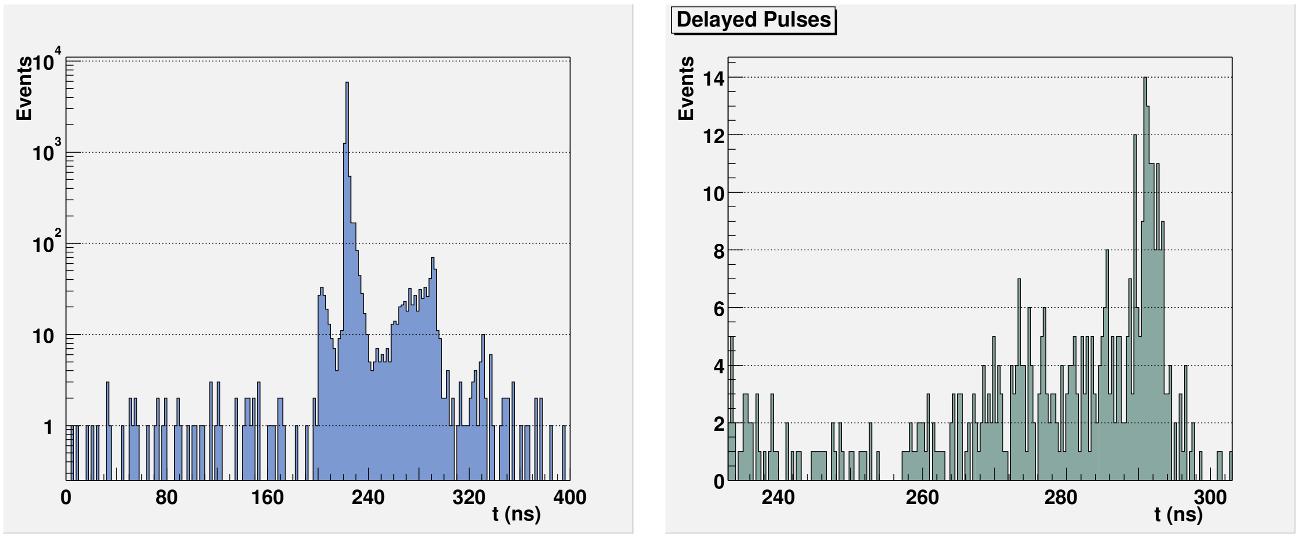

Figure 3.35: Left: Time distribution of all the pulses detected. Right: Time distribution of the delayed pulses for the Hamamatsu AF0174 PMT.

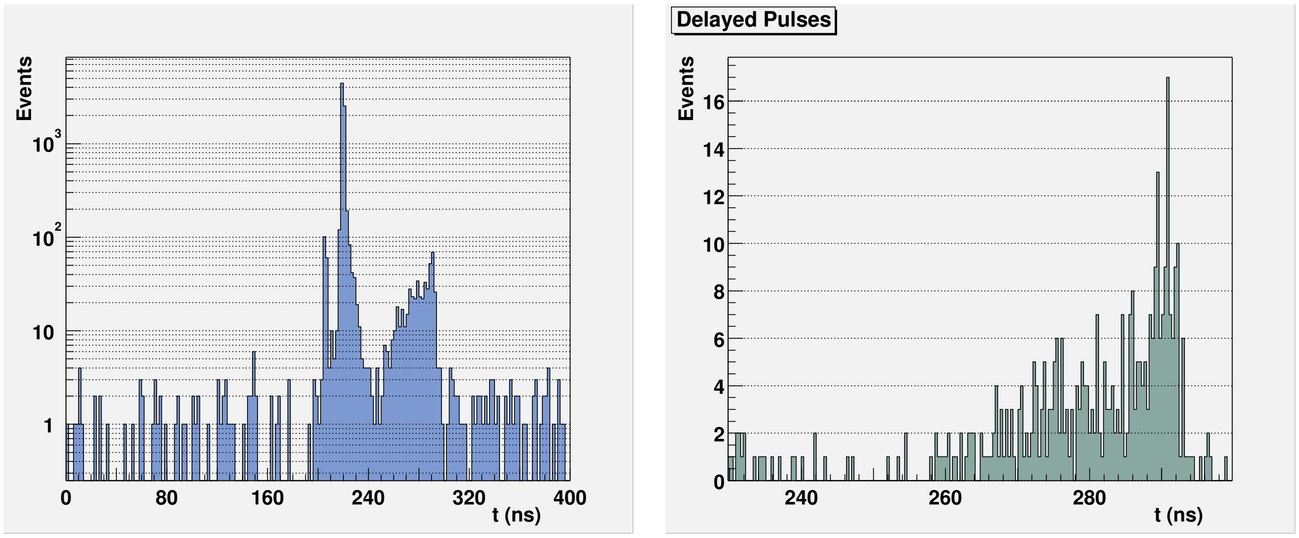

Figure 3.36: Left: Time distribution of all the pulses detected. Right: Time distribution of the delayed pulses for the Hamamatsu AF0175 PMT.

Figure 3.37 shows the amplitude distributions of delayed pulses (left) and afterpulses-1 (right) for the PMT AF0175, as an example of the Hamamatsu photomultipliers. The mean amplitude of delayed pulses is larger, but the spectra are more similar between them than in the case of Photonis.

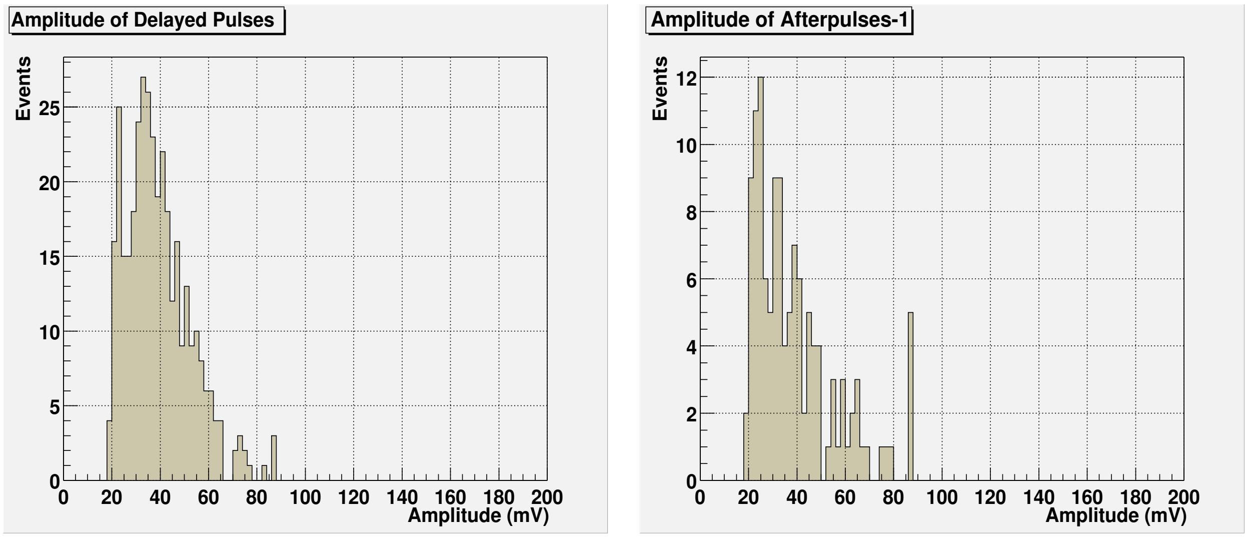

Figure 3.37: Amplitude distributions of delayed pulses (left) and afterpulses-1 (right) for Hamamatsu AF0175.

3.8.2.2 Afterpulses-2

As it has been mentioned, the information about afterpulses-2 is lost in the measurement procedure since the output PMT signal is too narrow to be detected by the oscilloscope in this scale (10 ns/channel). In this case, the position of the main pulse peak is located at the 20% of the whole scale, since only pulses after the main pulse have been analyzed.

- **Photonis** Figures 3.38 and 3.39 show the time distribution of all the pulses detected (left) and the afterpulses-2 (right), i.e. those associated with a pulse in the main window. The most clear difference between both distributions is the region just after the main pulse window. In the case of Photonis 39, the rate in the three first microseconds of the afterpulse-1 window is higher. After that, there is a broad peak 8 μs after the main pulse peak in the two distributions.

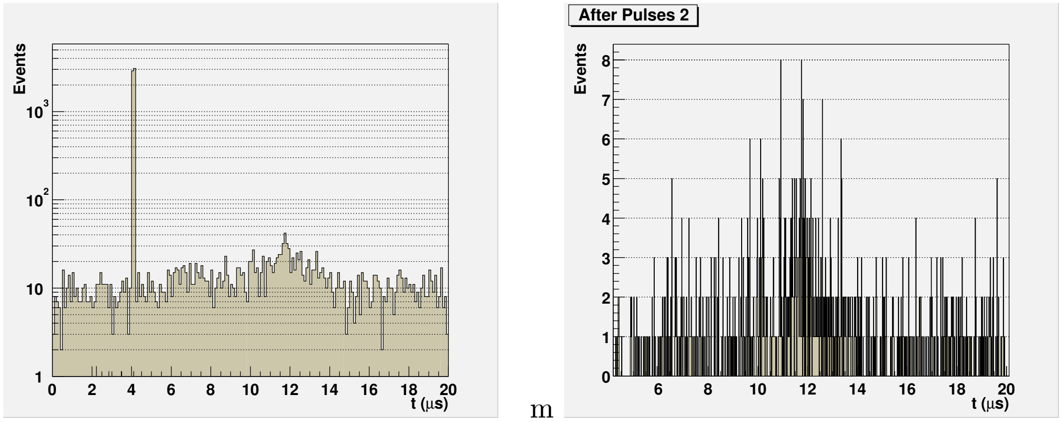

m

Figure 3.38: Left: Time distribution of all the pulses detected. Right: Time distribution of the afterpulses-2 for Photonis 35.

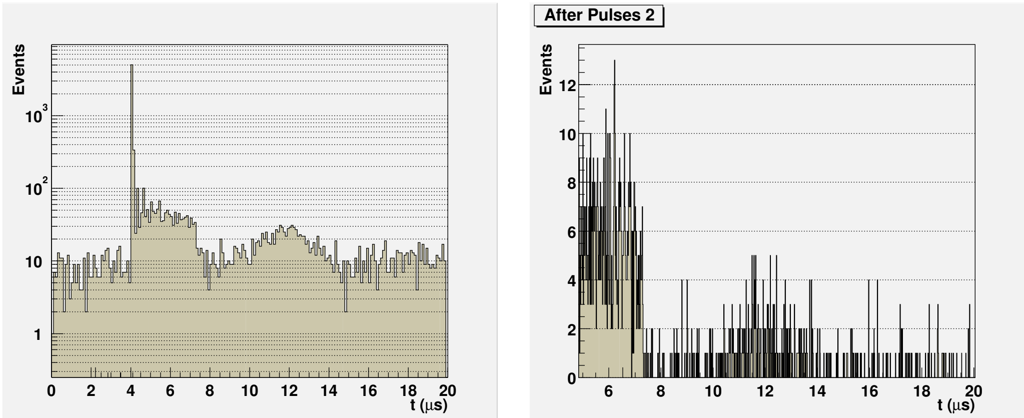

Figure 3.39: Left: Time distribution of all the pulses detected. Right: Time distribution of the afterpulses-2 for Photonis 39.

- **Hamamatsu**

The distributions of afterpulses-2 of the Hamamamatsu PMTs are shown in Figures 3.40-3.43. In this case, the distributions are very similiar among them. After the main pulse window, there is a wide region with nothing but dark noise. The afterpulse-2 peak is 12 μs later. The position of the peak and the amount of afterpulses-2 is very similar for all of them, when comparing Hamamamatsu AF0170 and AF0171 with AF0174 and AF0175. In addition to this peak, another peak appear $\sim$3 μs after the main pulse window. This peak can be seen clearly in the plots on the right.

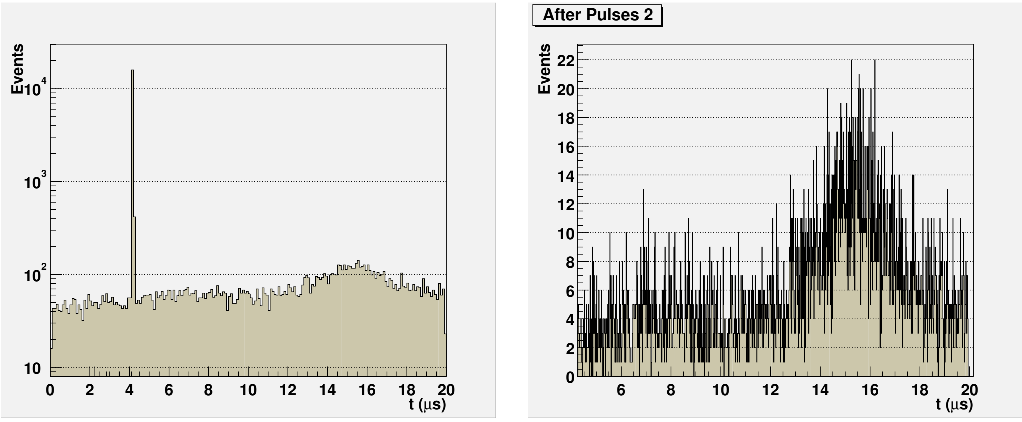

Figure 3.40: Left: Time distribution of all the pulses detected. Right: Time distribution of the afterpulses-2 for Hamamatsu AF0170.

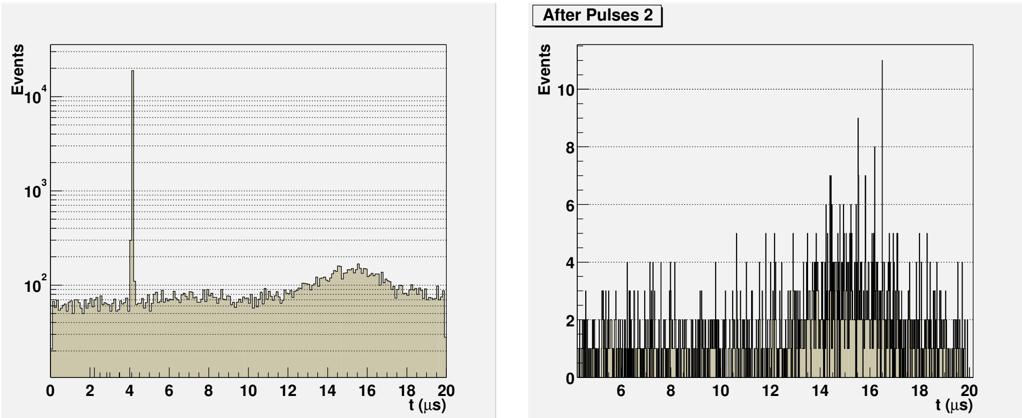

Figure 3.41: Left: Time distribution of all the pulses detected. Right: Time distribution of the afterpulses-2 for Hamamatsu AF0171.

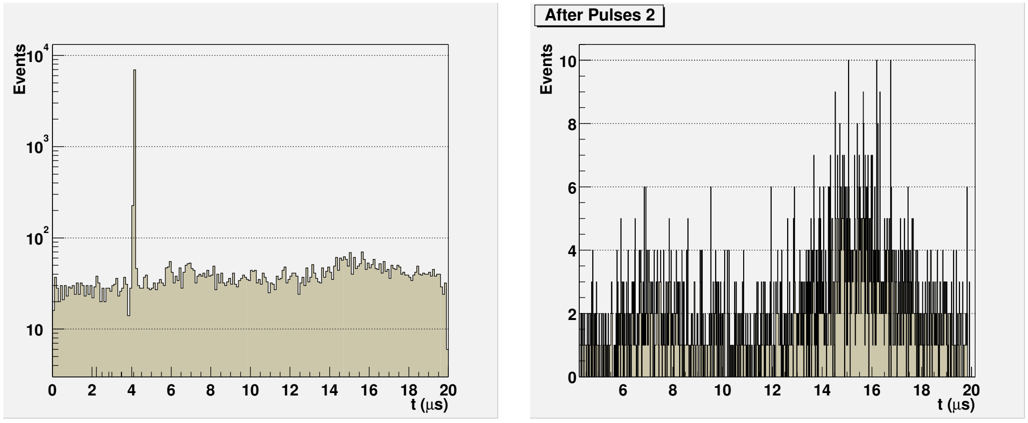

Figure 3.42: Left: Time distribution of all the pulses detected. Right: Time distribution of the afterpulses-2 for Hamamatsu AF0174.

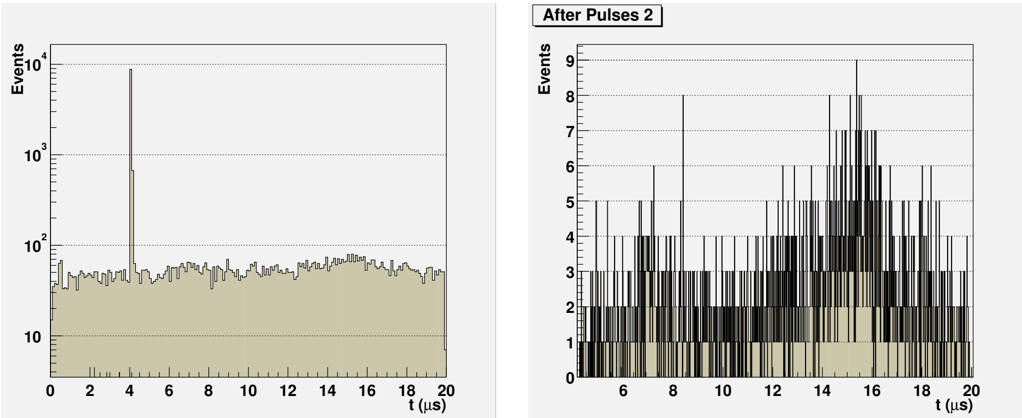

Figure 3.43: Left: Time distribution of all the pulses detected. Right: Time distribution of the afterpulses-2 for Hamamatsu AF0175.

Since afterpulses-2 are believed to be produced by ionised residual gas atoms, a possible explanation of the previous results is the effect of two different ions. The delay depends on the ion mass. Slow pulses are usually produced by Cs^+ (from the bialkali photocathode) and fast pulses, by H_2^+, He_2^+ and CH_4^+ [47]. The high rate observed in the fast afterpulse-2 region could be related therefore to a high contamination by these ions.

To summarize, the results of afterpulses are presented in Table 3.7. The prepulse and delayed rates are within the specifications (except for the prepulses of Ham AF0174 and AF0175), whereas the afterpulse-1 and afterpulse-2 rates are too high. Therefore, it is desirable that the manufacturers improve this point.

Rate (%)	**Prepulses** $[-80ns, -10ns]$	**Delayed Pulses** $[10ns, 80ns]$	**Afterpulses-1** $[10ns, 80ns]$	**Afterpulses-2** $[80ns, 16\mu s]$
Photonis 35	0.0 ± 0.4	4.7 ± 0.2	1.8 ± 0.1	15 ± 3
Photonis 39	0.0 ± 0.3	4.7 ± 0.2	1.8 ± 0.1	21 ± 4
Ham AF0170	0.7 ± 0.2	5.0 ± 0.2	2.8 ± 0.1	20 ± 2
Ham AF0171	0.8 ± 0.2	4.8 ± 0.2	2.6 ± 0.1	15 ± 2
Ham AF0174	1.6 ± 0.2	5.2 ± 0.3	1.7 ± 0.2	17 ± 3
Ham AF0175	2.3 ± 0.2	4.8 ± 0.3	1.6 ± 0.2	17 ± 3

Table 3.7: Afterpulse rates for the studied photomultipliers.

3.9 Conclusions

The results obtained are summarized in Table 3.8.

	Photonis 35	**Photonis 39**
Nominal Voltage (V)	1738	1615
Signal Amplitude (mV)	60.2 ± 1.3	62.5 ± 0.8
Peak to valley ratio	1.8 ± 0.1	3.5 ± 0.1
Energy resolution (%)	33 ± 2	29 ± 2
TTS (FWHM (ns))	1.8 ± 0.1	2.1 ± 0.1
Dark noise rate (1/2pe) (kHz)	3.4 ± 0.1	5.3 ± 0.1
Prepulses rate (%)	0.0 ± 0.4	0.0 ± 0.3
Delayed pulses rate (%)	4.7 ± 0.2	4.7 ± 0.2
Afterpulses-1 rate (%)	1.8 ± 0.1	1.8 ± 0.1
Afterpulses-2 rate (%)	15 ± 3	21 ± 4

Table 3.8: Results for the Photonis photomultipliers at the nominal voltage.

	AF0170	**AF0171**	**AF0174**	**AF0175**
Nominal Voltage (V)	1995	1757	1941	1918
Signal Amplitude (mV)	33.2 ± 1.2	30.5 ± 1.2	34.3 ± 0.5	35.8 ± 0.7
Peak to valley ratio	4.2 ± 0.2	2.9 ± 0.2	4.1 ± 0.3	3.4 ± 0.2
Energy resolution (%)	36 ± 2	37 ± 2	32 ± 2	32 ± 2
TTS (FWHM (ns))	2.5 ± 0.1	2.7 ± 0.1	2.6 ± 0.1	2.6 ± 0.1
Dark noise rate (1/2pe) (kHz)	10.5 ± 0.2	8.6 ± 0.2	4.3 ± 0.1	4.6 ± 0.1
Prepulses (%)	0.7 ± 0.2	0.8 ± 0.2	1.6 ± 0.2	2.3 ± 0.2
Delayed pulses (%)	5.0 ± 0.2	4.8 ± 0.2	5.2 ± 0.3	4.8 ± 0.3
Afterpulses-1 (%)	2.8 ± 0.1	2.6 ± 0.1	1.7 ± 0.2	1.6 ± 0.2
Afterpulses-2 (%)	20 ± 2	15 ± 2	17 ± 3	17 ± 3

Table 3.9: Results for the Hamamatsu photomultipliers at the nominal voltage.

We can conclude that there are some significant differences between the two Photonis photomultipliers. Photonis 39 satisfies all the specifications except the requirement on the afterpulse-2 rate. On the other hand, Photonis 35, whose nominal voltage and signal amplitude are higher, has a poor peak to valley ratio, and a high afterpulse-2 rate.

The properties of the Hamamatsu photomultipliers are in general within specifications. However, as in the case of the Photonis photomultipliers, the afterpulse-2 rate is too high for all the photomultipliers. In addition to that, the nominal amplitude below the requirements.

Chapter 4

General Characteristics of the Optical Beacon Simulation

In this chapter, a general description of the Optical Beacon simulation is presented. As it will be seen in Section 4.1, the Optical Beacon is one of the time calibration systems of the ANTARES detector. The aim of this part of this work is to study by Monte Carlo simulation the features and performances of different possible layouts of the time calibration system based on external light sources. The characteristics of the simulated sources are described in Section 4.2; the simulated layouts, in Section 4.3; the programs used, in Sections 4.4 and 4.5, and the simulated water models are explained in Section 4.6.

4.1 Timing calibration

As it was mentioned when the detector perfomance was presented, a good accuracy in the timing calibration is essential to perform a good muon track reconstruction. For this reason, it is important to identify and measure all the possible time delays and jitters. In this section, these delays and the methods used to measure them are described.

Three independent and complementary systems will perform the relative timing calibration [52] (see Figure 4.1):

- The internal clock calibration.
- The PMT transit time calibration.
- The detector relative time offsets calibration with external light sources (Optical Beacons).

4.1.1 Internal clock calibration

This system aims to measure the relative offsets of every Local Control Module internal clock signal. The signal of the Master Clock generated on shore is sent by optical path to each LCM. This signal is returned to the shore station and the propagation delay between the Master Clock and every LCM is measured. The accuracy of the delay measurement has to be better than 0.5 ns. The jitter in the difference of the propagation delays between the shore and the detector has to be less than 0.5 ns. Each LCM clock calibration should take ~ 1 min or less. The internal clock calibration can be performed in parallel to physics data acquisition. The delay between the LCM clock card and each ARS motherboard will not be measured *in situ* but in previous laboratory tests [53].

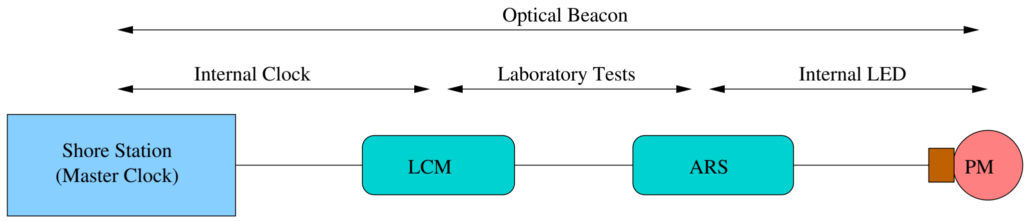

Figure 4.1: Sources of time offsets.

4.1.2 PMT transit time calibration

As it has been mentioned in the description of the Optical Modules, a LED will be included in order to monitor the transit time of every PMT. The arrival time of the photons will be measured with the ARS time-stamping. It is important to limit the light intensity in the PMT to a few photons to avoid saturation problems and the dependence of the transit time on the number of photons. The jitter of the LED trigger signal has to be lower than 0.5 ns, with a maximum emission delay drift of 0.25 ns/year.

4.1.3 Detector relative time offsets calibration

The aim of this system is to measure the relative time offsets integrating *all the delays*. A number of light sources (OBs) will produce short duration flashes which will illuminate several Optical Modules of the detector. An accuracy of $\sigma = 0.5$ ns is required to allow an angular resolution of $0.2°$.

Apart from being useful for the calibration, the Optical Beacons can also be used to perform event reconstruction tests and to monitor the water optical properties.

To be reliable, this calibration has to be done *in situ*. Because of the importance of this measurement, a high level of redundancy is necessary. It is also important to use a source which emits near the optimal wavelength to avoid absorption ($\lambda \sim 470$ nm). The candidate light sources are discussed in Section 4.2.

Concerning the layout of the OB, four configurations have been proposed, as it is explained in Section 4.3.

- A single LED in each Optical Module (*single LEDs*).
- Several LED cylinders along each line of the detector (*LED beacons*).
- A laser in the instrumentation line (*laser beacon*).
- Lasers in the detector.

The results of the simulation with these four configurations are presented and discussed in Chapter 5.

4.2 Characteristics of the sources

Several options have been studied for the Optical Beacon calibration. The original idea was to use a few, very intense sources to illuminate most of the detector, being lasers the natural candidates.

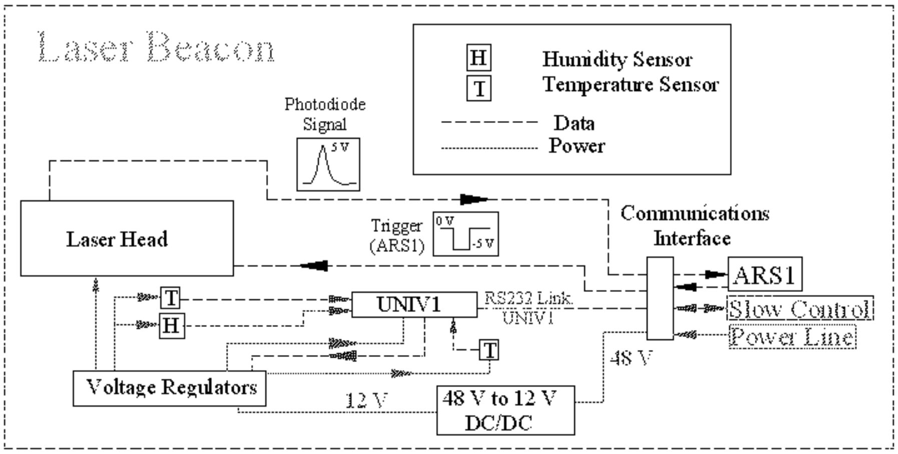

Figure 4.2: Scheme of the laser setup.

However, absorption is a major problem in this concept, since, as it will be shown in Chapter 5, very different amounts of light will arrive at different distances. Moreover, the optimal light wavelength for propagation in water is 470 nm, i.e. blue light, but only green Nd-YAG lasers are at present suitable from an operational point of view. Other possibilities, such as dyed nitrogen lasers, are too complex and have several major drawbacks. It is not straighforward either to regulate the amount of light emitted by a laser.

Therefore, due to absorption and scattering, a configuration with many more sources, but less intense, illuminating only small parts of the detector seems to be the adequate solution. Blue LEDs are the best candidate sources in this configuration. They emit in the optimal wavelength and their intensity can be adjusted. Most of the pulses coming from muon tracks are expected to be single photoelectron events. Depending on the pulse height, the ARS will work in the *single photoelectron mode* or in the *waveform mode*. Therefore, light sources adjustable in intensity are also convenient from this point of view.

In this study, both the green laser and the blue LEDs have been simulated. Their main characteristics are presented here:

4.2.1 Green laser

The characteristics of the green Nd-YAG laser were described in Section 2.3.2. Figure 4.2 shows a scheme of the setup that will be used to trigger the laser in the beacon.

The pulse frequency can be tuned with a special circuit from 10 Hz to 10 kHz. There will be a photodiode to measure the exact time of emission of the light pulse. The time jitter between the photodiode and the light flash is smaller than 50 ps [48].

4.2.2 Blue LED

The light source in the second and third configurations is a blue LED. The emission peak is at λ= 470 nm (FWHM=15 nm), which is the wavelength with the smaller absorption in water. The rise-time (10%-90%) is around 1.8 ns (independently of the feed voltage) and the FWHM is 6.5 and 4.5 ns, at –7 V and –24 V respectively.

The LEDs will be pulsed with the so-called "Sheffield" fast timing pulser [54], based on the Kapustinsky circuit [55], which can operate up to 10 kHz. The light output level can be adjusted by changing the voltage. The number of photons emitted per pulse by each LED is between 5×10^6 (2 pJ) and 8×10^7 (30 pJ) when working at –7 V and –24 V respectively.

4.3 Configurations for the Optical Beacon

4.3.1 Laser in the instrumentation line

The instrumentation line is an additional string foreseen to obtain complementary information about environmental quantities, such as sound velocity, water current, temperature, salinity, etc. This string would need only low power and small data bandwidth provided by the slow control network. Figure 4.3 is a scheme of the proposed prototype [56], still under discussion.

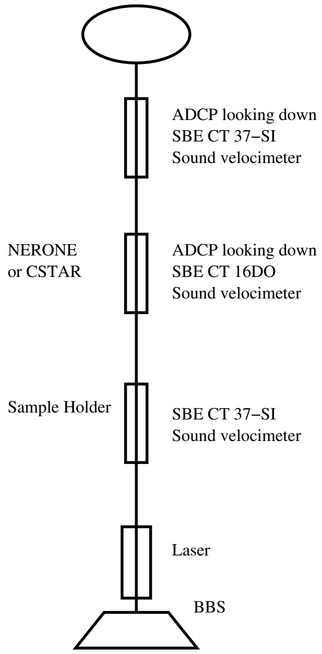

Figure 4.3: Instrumentation line scheme.

A laser will be located at the bottom of the string so as to have a high power light source available for calibration purposes at a fixed position in the detector.

The laser will be housed in a cylindrical titanium container located in the upper part of the Bottom String Socket (BSS). A drawing of the laser container can be seen in Figure 4.4. Both the electronics and the laser head will be installed inside the cylinder. The laser will be pointing upwards and the beam directed to a Lambertian diffuser located at the centre of the cover. In order to prevent any damage due to the reflected beam, the laser will be slightly tilted. This does not affect the angular distribution of the outgoing light, as it has been checked in the laboratory. The mechanical structure to fix the optics (laser and diffuser) will be isolated in a hermetically closed box.

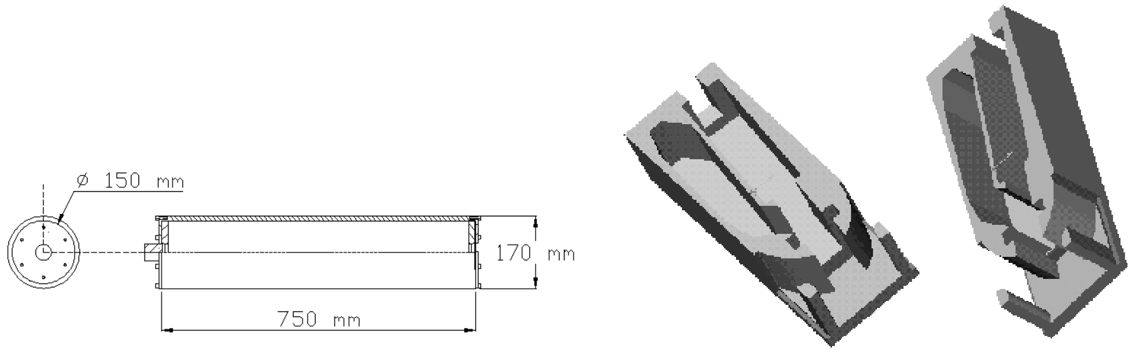

Figure 4.4: Scheme of the laser container and its internal structure.

To avoid the sedimentation on the diffuser, a glass cylinder is put on top of it, as it is shown in Figure 4.5. In this setup, the light leaves the cylinder through the vertical walls, where the sedimentation is negligible [57].

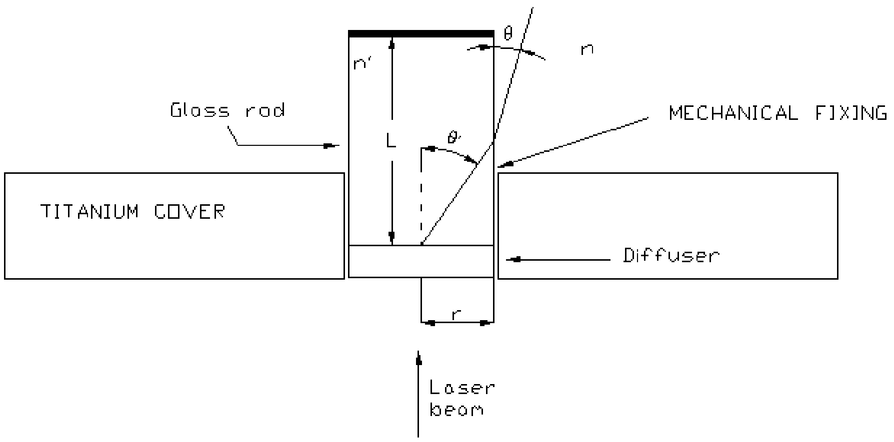

Figure 4.5: Scheme of borosilicate glass cylinder position.

4.3.2 LED beacons

Although the laser can illuminate a large fraction of the detector, due to the exponential effect of absorption, there will be large differences in the illumination level of the OMs as will be seen in Chapter 5. Scattering will also degrade the time distribution of the pulses for those OMs far away from the laser. Therefore, less powerful sources distributed evenly throughout the detector will be needed. These sources will be the LED beacons, which are planned to be mounted above the LCMs of some of the storeys and supported by the Optical Module Frame. The number of LED beacons has to be high enough so as to ensure a complete light coverage of the detector with a good level of redundancy. In this work five optical beacons along each line have been simulated. The frequency of the light flashes will be 10-100 Hz, so that it will take less than 20 minutes to generate 10^4 flashes.

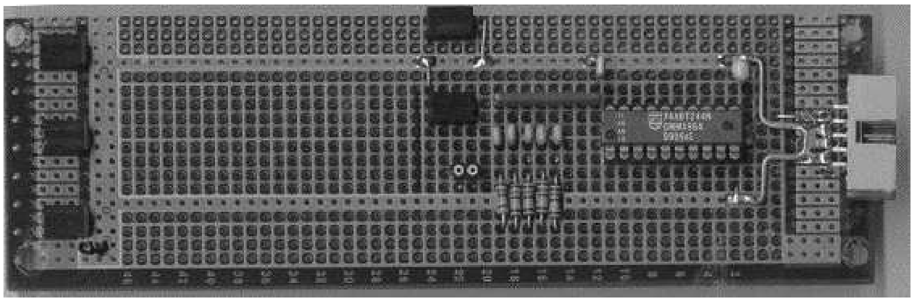

Figure 4.6: Picture of the LED beacon face.

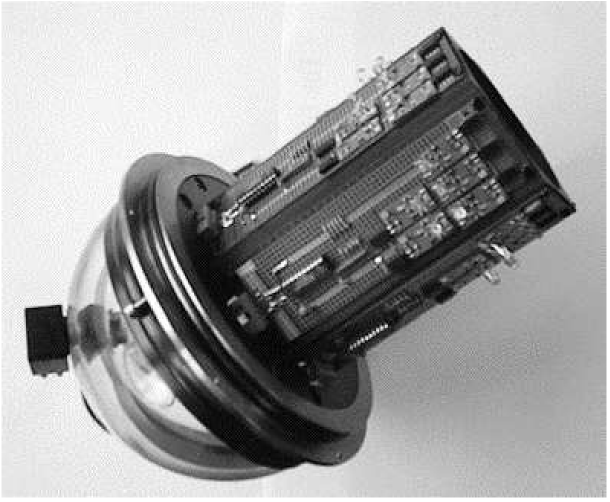

Figure 4.7: Picture of the LED beacon mounting.

Each beacon consists of six faces arranged on a hexagonal configuration inside a pressure-resistant cylinder. There are five LEDs in each face. Figures 4.6 and 4.7 show a picture of one beacon face and of the beacon mounting. The logic chip on each beacon face allows to pulse one, four or five LEDs simultaneously. This gives a factor ~80 in the total light yield (a factor 16 from the voltage tuning and a factor 5 from the number of LEDs pulsed).

It would be also desirable to include a PMT in the beacon to give a time of emission independent of the electronics between the LCM and the LED pulser. This PMT would be also useful for the amplitude calibration.

4.3.3 Single LED beacons

Another calibration system has been proposed [58] in order to get a higher level of redundancy. It consists in a single LED inside each Optical Module. The LED has to be situated as close as possible to the horizontal equator plane of the pressure-resistant sphere to avoid fouling. It would be mechanically attached to the μ-metal cage and buried inside the gel. One of the advantages of this system with respect to the LED beacons is that no new elements (specific connectors, cables or mechanical supports) are required in the string.

The angular distribution of light emitted by the single LED beacon has been measured [59] in

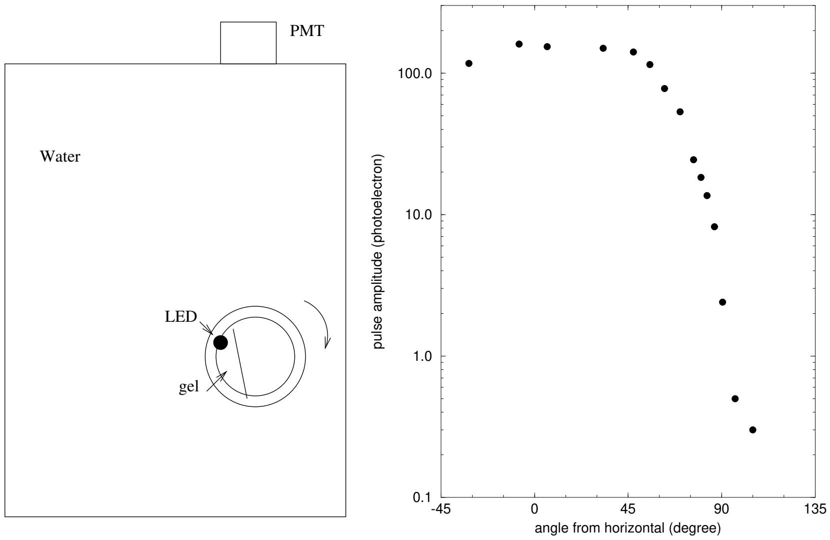

Figure 4.8: Left: experimental setup used to measure the angular distribution of light emitted by the single LED beacon. Right: results of the angular distribution of the single LED beacon. The maximum amplitude corresponds to the case of the LED pointing to the PMT.

a water tank using the experimental setup presented in Figure 4.8 (left). The results are presented in Figure 4.8 (right).

Our Monte Carlo simulation simplifies this distribution and assumes that the light from the LED is isotropically distributed in a cone with half angle θ_{LED}=63° whose axis points 27° over the horizontal, as it is explained in Chapter 5.

4.3.4 Lasers in the detector

In this configuration, several detector strings will be equipped with a laser. It is similar to the case of a laser in the instrumentation line. The higher the number of lines equipped with a laser, the higher the level of redundancy.

4.4 Description of the simulation code

The Monte Carlo program used for the simulation is `Calibob` [60], a modified version of the `KM3` package [61] to simulate optical beacon sources located in the 0.1 km^2 detector. In this section, the three components of `KM3` (`GEN`, `HIT` and `KM3MC`) are described together with the relevant features of `Calibob`.

4.4.1 GEN

`GEN` is the first stage in the complete simulation chain. Photons are generated either isotropically (LED) or with a Lambertian angular distribution (laser) from a pointlike source. Photon propagation is made including the effects of absorption and scattering of light in water, according to different models that will be explained in Section 4.6.1. The water volume is divided in spherical shells of different radii, r_i, centred at the source. Every time a photon hits one of these shells, `GEN`

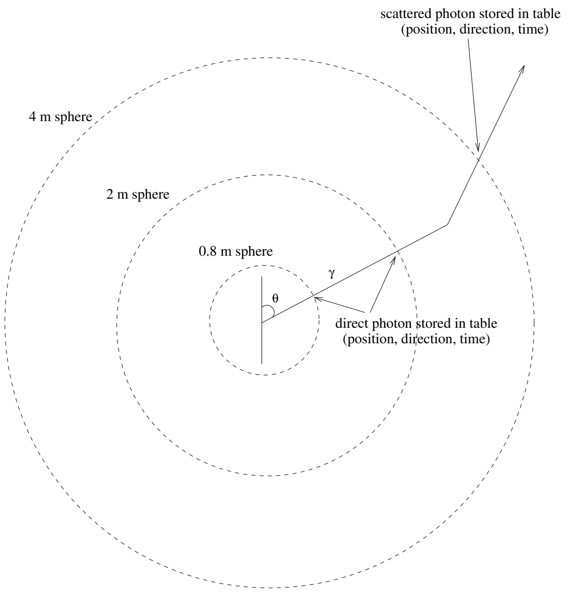

Figure 4.9: Scheme of the spherical shells defined in GEN.

records its position, direction and arrival time (see Figure 4.9). Photons are propagated up to a distance of 350 m from the source.

4.4.2 HIT

Once all the photons have been generated, the information stored by GEN is converted into photoelectron probabilities and arrival time distributions. This is done by HIT. In HIT every shell is divided in 20 parallel bands of equal area at different polar angles θ_j, (see Figure 4.10). Then, the probability that any photon hitting the j-th band of the i-th shell produces a photoelectron in the photomultiplier is computed according to:

$$p^k_{r_i,\theta_j} = \frac{\epsilon_{PMT} \cdot A_{PMT}}{A_{band}|\vec{u}_\gamma \cdot \vec{u}_{band}|} \tag{4.1}$$

where A_{PMT} is the PMT area, $A_{band}|\vec{n}_\gamma \cdot \vec{n}_{band}|$ is the band area seen by the k-th photon, and ϵ_{PMT} is the detection efficiency which takes into account the PMT quantum and collection efficiencies, the transmissivity through the optical module and its angular dependence. Figure 4.11 shows the distributions which have been used [62]. The addition of all these probabilities gives the average number of photoelectrons $\langle \#pe \rangle_{r_i,\theta_j}$ produced in a photomultiplier located in the j-th band at a distance r_i:

$$\langle \#pe \rangle_{r_i,\theta_j} = \sum_k p^k_{r_i,\theta_j} \tag{4.2}$$

These average values are computed for different orientations of the optical module θ^{OM}_l and ϕ^{OM}_m, and stored in 'OM hit tables' which will be used in the next program, KM3MC, to compute the $\langle \#pe \rangle$ for any value of the variables r, θ, θ^{OM} and ϕ^{OM} by multiple linear interpolation. The program treats separately direct and scattered photons.

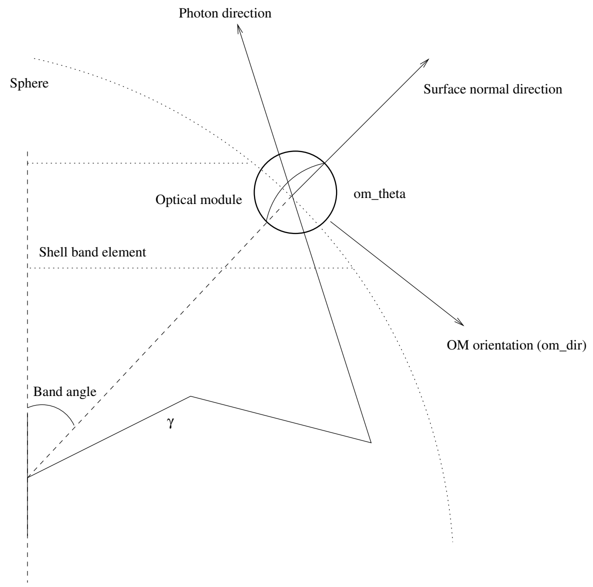

Figure 4.10: Variables used in `HIT`.

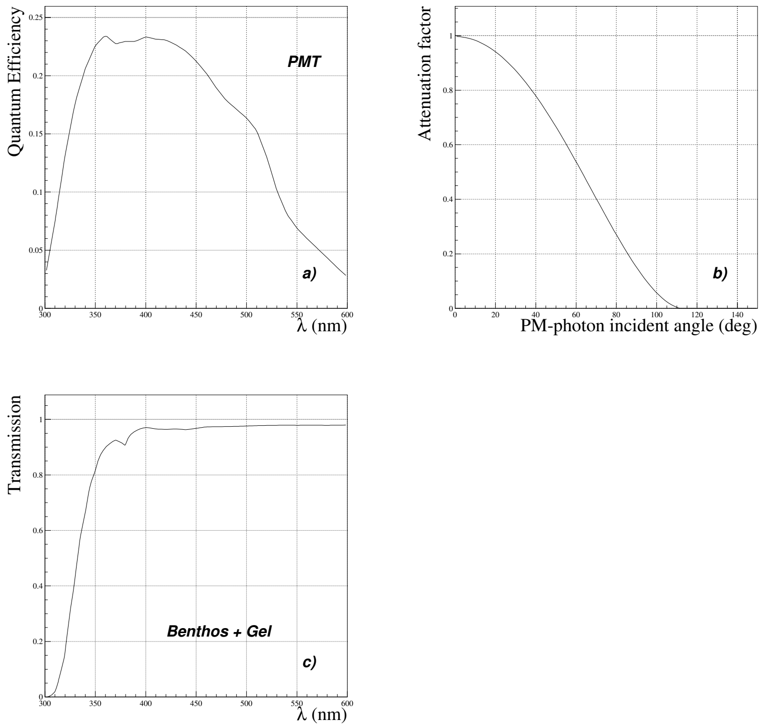

Figure 4.11: Experimental results of OM parameters included in the simulation: a) Quantum efficiency of the photomultiplier, b) Light attenuation factor in the pressure-resistant sphere, c) Transmission.

A similar procedure is applied for time distributions. For every shell, band and OM orientation, an arrival time distribution is built from the photon hit times stored by GEN. This distribution is converted into an inverse cumulative time function and stored as a reference in 'OM time tables'. Once in KM3MC, the arrival time of any photon is obtained interpolating between these reference distributions.

4.4.3 KM3MC

The last stage of the simulation is the program KM3MC. It takes as input the 'OM hit and time tables' computed by HIT, the detector description file with the location and orientation of all the OM clusters (see next section) and the user input card file describing the source (LED or laser) to be simulated. For every light shot from the source, the number of photoelectrons produced in each OM and the arrival time of photons are computed. For this purpose the following assumptions were made:

- The number of photoelectrons produced in a OM (hits) is obtained by sampling a Poisson distribution whose mean value is the average number of photoelectrons obtained from the HIT tables, $\langle \#pe \rangle$. A random amplification gives the output charge for each photon. Photons arriving at the same PMT within the same 0.2 ns time window are merged together and their charge added.
- The transit time spread (TTS) of the photomultiplier is taken into account adding a time delay given by:

$$\Delta t = \frac{R \cdot \sigma_{TTS}}{\sqrt{Q}} \tag{4.3}$$

  where R is a Gaussian distributed random number (with μ=0 and $\sigma = 1$), $\sigma_{TTS} = 1.3$ ns is the TTS of the photomultiplier and Q is the charge of the hit in terms of single photoelectrons.
- The electronics beyond the photomultiplier has not been simulated (ARS, pile-up, noise, etc.).
- The background from ^{40}K has not been included either since it is expected to be negligible at this level of lighting in the time window used in the calibration ($< 10^{-3}$ hits in a 10 ns window).
- Shadow effects due to mechanical structures have been ignored. However, the limited angular coverage of the Optical Beacons is taken into account.
- The time spread of the source is simulated assuming a Gaussian distribution for the light pulse. The light sources have been assumed to be pointlike.

4.5 Detector generator: GENDET

An important part in the simulation is the generation of the detector. GENDET [63] aims to produce spiral detectors, since this is the standard geometry, as it has been mentioned in Chapter 1. The positions of all the elements of a typical line (OM, LCM, PMT, tiltmeter, hydrophone, etc.) can be generated from the input cards.

In order to build a detector as realistic as possible, GENDET can simulate the misalignment due to the action of horizontal currents. In addition, it is possible to introduce other types of offsets:

- Positioning of the strings, which displaces the strings out of a perfect configuration. This offset can be horizontal and vertical to take into account both the irregularities of the bed sea and the displacement in the deployment process.
- Time offset of the strings and the LCMs.
- Twist rate and twist offset of the strings to simulate the effect of water currents.
- Time offset, efficiency offset and amplitude offset of the OMs.

To simulate not spiral detectors, the output files from GENDET can be modified by hand changing the position of the elements which are relevant in our simulation, i.e. the horizontal position of the strings and the clusters.

4.6 Optical water properties

The study of the propagation of light in water involves two phenomena: absorption and scattering. Such processes can be described by the following parameters:

- The absorption coefficient $a(\lambda)$ or the absorption length: $\lambda_{abs} = 1/a(\lambda)$.
- The scattering coefficient $b(\lambda)$ or the scattering length: $\lambda_{scat} = 1/b(\lambda)$.
- The volume scattering function $\beta(\theta, \lambda)$ which represents the probability that photons are scattered out of a beam through an angle θ.

Integrating the volume scattering function $\beta(\theta, \lambda)$ over all directions (solid angles), the scattering coefficient $b(\lambda)$ is obtained:

$$b(\lambda) = \int_{\Omega} \beta(\theta, \lambda) d\Omega \tag{4.4}$$

The scattering phase function $\tilde{\beta}(\theta, \lambda)$ is defined as:

$$\tilde{\beta}(\theta, \lambda) = \beta(\theta, \lambda)/b(\lambda) \tag{4.5}$$

which gives the angular distribution of the scattered photons regardless of the strength of the scattering.

Figuree 4.12 shows the absorption and scattering length spectra in the simulation. The absorption spectrum was built using the data obtained by the NESTOR collaboration from direct measurements in the Mediterranean sea [64]. For the scattering length dependence on wavelength, the Kopelevich parametrisation for clear water is used ([65] p.124):

$$\lambda_{scat} = 0.0017 \left(\frac{550}{\lambda}\right)^{4.3} + 1.34\nu_s \left(\frac{550}{\lambda}\right)^{1.7} + 0.312\nu_l \left(\frac{550}{\lambda}\right)^{0.3} \quad (m)^{-1} \tag{4.6}$$

where ν_s and ν_l are the volume concentrations of small and large particles (in ppm), respectively.

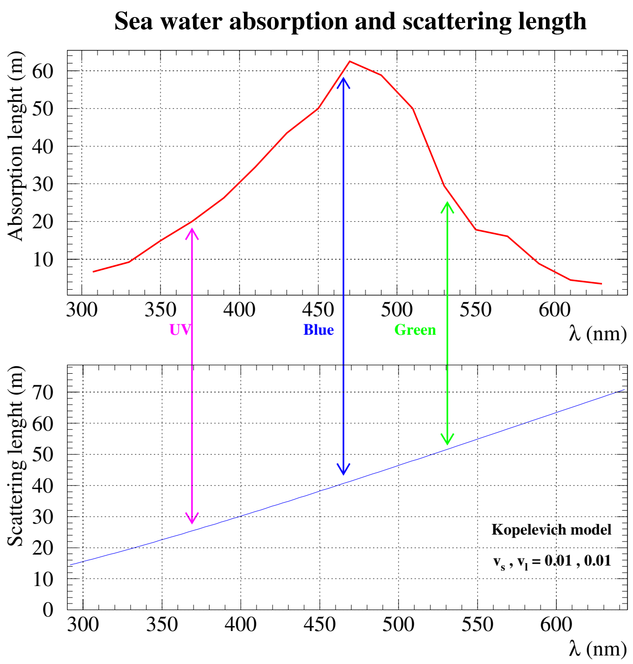

Figure 4.12: Absorption and scattering spectra [64, 65] used in the simultion.

Scattering of light takes place when randomly distributed optical inhomogeneities in the medium (scattering centres) produce random changes in the direction of light. In seawater, the scattering centres are density fluctuations originated by random molecular motion (molecular scattering), and organic and inorganic suspended particles (scattering by particles). In the first case, the resulting angular distribution can be parametrized as::

$$\tilde{\beta}_{mol}(\theta) = 0.06225(1 + 0.835\ \cos^2\theta) \tag{4.7}$$

which looks like the well-known "Rayleigh" scattering. The factor 0.835 comes from the anisotropy of water molecules and the distribution is forward-backward symmetric.

On the other hand, suspended particles which are large in comparison with the wavelength scatter light forward most strongly through small angles with respect to the direction of the incident light. Therefore, the phase function from particle scattering is strongly peaked in the forward direction.

4.6.1 Water models

The optical water properties are an important input in the simulation, but they are not completely established, because of the scarcity of data applicable to the ANTARES site. Two models have been used to describe the water optical properties, called thereafter "Medsea" and "Global".

4.6.1.1 Mediterranean sea model: Medsea

The analytical formula most commonly used to describe the asymmetric scattering is the Henyey-Greenstein (HG) function [66]:

$$\tilde{\beta}_{HG}(g,\theta) = \frac{1}{4\pi}\frac{1-g^2}{(1+g^2-2g\cos\theta)^{3/2}} \tag{4.8}$$

where g is the average of the cosine of the scattering angle, $\langle\cos\theta\rangle$:

$$g = 2\pi\int_{-1}^{1}\tilde{\beta}(g,\theta)\cos\theta\; d(\cos\theta) \tag{4.9}$$

Measurements made in the Mediterranean sea (Ref. [65] p.106) can be well approximated by the linear combination of two Henyey-Greenstein phase functions [67]:

$$\tilde{\beta}_{med}(g_1,g_2,\theta) = \alpha\tilde{\beta}_{HG}(g_1,\theta) + (1-\alpha)\tilde{\beta}_{HG}(g_2,\theta) \tag{4.10}$$

The parameters $g_1 > 0$ and $g_2 < 0$ enhance scattering at small and large angle, respectively. In Figure 4.13 it is shown how well data collected *in situ* is fitted to this new function. The parameter values defining the **Medsea** model are $\alpha = 0.985$, $g_1 = 0.92$ and $g_2 = -0.6$.

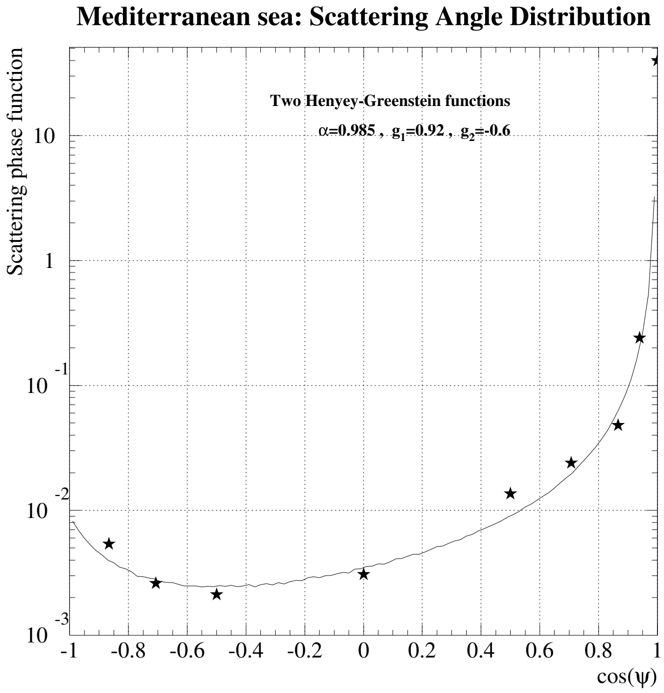

Figure 4.13: Scattering phase function resulting from the fit to the experimental data taken *in situ* in the Mediterranean sea (stars).

4.6.1.2 Global

Instead of using an analytical approximation, this model is based on a linear combination of two terms depending on the population of scattering centres [68]. The first term is related to the molecular scattering whose phase function $\tilde{\beta}_{mol}(\theta)$ is given by expresion (4.7). The second term takes into account scattering by particles. In this case, following the approach of Mobley (Ref [65] p.111), the phase function is obtained as the average of three particle phase functions measured by Petzold [69] in different waters: turbid, coastal and clear water. The uniform shape of the angular dependence for different kind of waters makes the definition of a typical particle phase function, $\tilde{\beta}_{part}(g,\theta)$, reasonable. Therefore, the **Global** phase function is given by:

$$\tilde{\beta}_{glob}(g,\theta) = \eta\tilde{\beta}_{mol}(\theta) + (1-\eta)\tilde{\beta}_{part}(g,\theta) \tag{4.11}$$

where η is the probability of molecular scattering and $1-\eta$ is the probability of particle scattering. In the ANTARES site, the parameter η, which weights the contribution of each term, is expected to be $0.1 < \eta < 0.2$ for media with a low chlorophyll concentration and for blue light. The final value used in the simulation is $\eta = 0.17$, since this is the value which is deduced from the measurements performed by the ANTARES collaboration. In Figure 4.14, a comparison between models is presented.

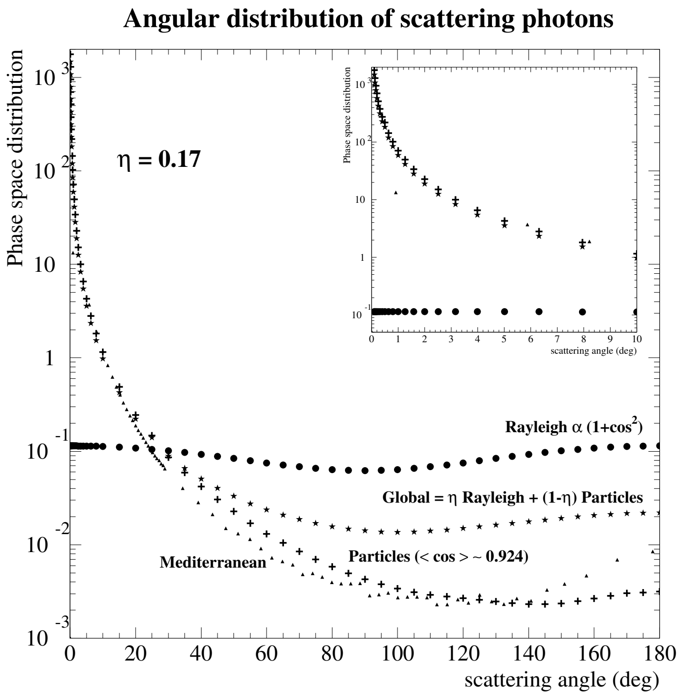

Figure 4.14: Comparison between the scattering phase function of the models **Medsea** and **Global**. **Rayleigh** and **Particle** distributions are also shown.

In Table 4.1, the parameters of **Medsea** and **Global** are compared.

λ	λ_{abs}	λ_{scatt}	Scattering phase function
466 nm	60.0 m	40.8 m	$\tilde{\beta}_{med}(\theta) = 0.985 \cdot \tilde{\beta}_{HG}(0.92, \theta) + 0.015 \cdot \tilde{\beta}_{HG}(-0.6, \theta)$
532 nm	28.3 m	51.8 m	
466 nm	60.0 m	52.0 m	$\tilde{\beta}_{glob}(\theta) = 0.17 \cdot \tilde{\beta}_{mol}(\theta) + 0.83 \cdot \tilde{\beta}_{part}(0.924, \theta)$
532 nm	28.3 m	66.8 m	

Table 4.1: Absorption length, scattering length and scattering phase functions of **Medsea** and **Global**. Differences in λ_{scat} arise from the different values used in Eq. 4.6: $\nu_s = \nu_l = 0.01$ in **Medsea** and $\nu_s = \nu_l = 0.0075$ in **Global**.

Chapter 5

Results of the Simulation

In this chapter, the results of the simulation of the proposed configurations are presented. In Section 5.1, the timing calibration analysis is explained in detail. The results for the different simulated configurations are presented in the following sections. These results have been also published in [70–72].

5.1 Analysis

The output of the program `Calibob` is an ntuple with the distributions of $t = t_{arrival} - t_{direct}$ for the hits of each OB-PMT pair (see Figure 5.1). $t_{arrival}$ is the total time since the photon is emitted until it is detected and $t_{direct} = dn/c$, where d is the OB-PMT distance; c, the speed of light in vacuum and n, the refractive index of water. In principle, the entries are expected to cluster around zero. However, both the time width of the source pulse and the TTS of the PMT tend to spread the distribution of t. This spread has been simulated by Gaussian distributions for both effects. On the other hand, scattering induces time delays which produce the tail observed in the right part of the distribution and can also move the position of the peak to larger values of t.

The aim of the simulation is to reconstruct the true position of this peak in order to measure the relative time offsets of the Optical Modules. To estimate this position the left part of the distribution, which is less affected by scattering, is fitted to a Gaussian, as shown in Figure 5.1. All the bins up to the third after the maximum are employed. Once the distribution is fitted, two parameters are used to determine the position of the peak before scattering: the value of t at which the fitted distribution has its maximum, T^{100}, and the lowest value of t at which the fitted distribution reaches half the maximum, T^{50} (see Figure 5.2). These two parameters are affected differently by the different effects. T^{100} is expected to be more sensitive to scattering, so the dependence on the OB-PMT distance will be stronger, while T^{50} should be more affected by the uncertainties in the knowledge of the FWHM of the source.

To have unbiased estimates of the true T_0, the values of T^{100} and T^{50} have to be corrected by the dependence on the distance and, in the case of T^{50}, by the analytical offset, FWHM/2, introduced by its definition. This is discussed in detail in the following sections.

We say that a PMT has been "illuminated" when there are more than 30 entries in the most populated bin of the arrival time distribution, after 10^4 light shots.

Additional information, such as the total charge in the PMT, the number of flashes emitted by the source, the OB-PMT distance and the position and the orientation of the PMT have also been recorded.

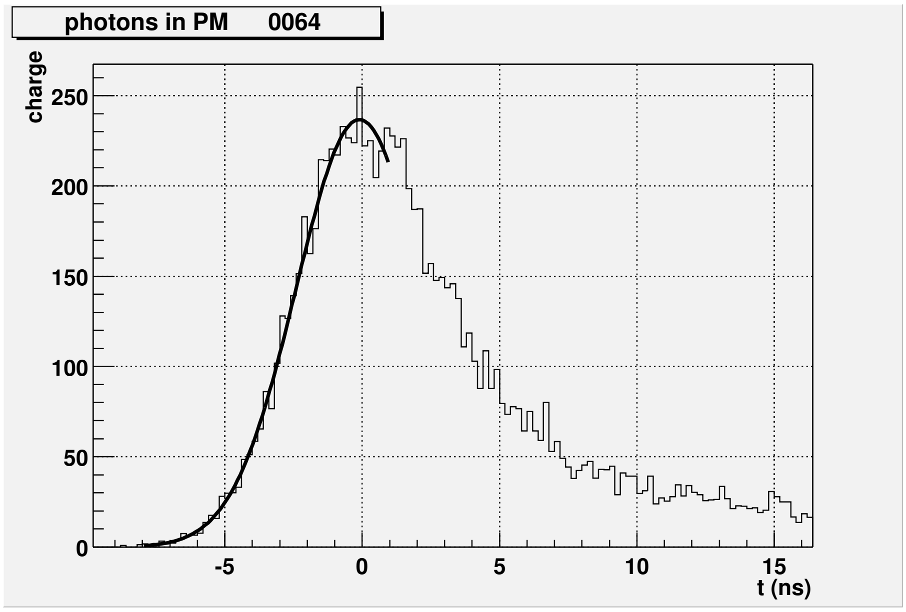

Figure 5.1: Example of time distribution output from `Calibob`. The curve is the result of a Gaussian fit up to the third bin after the maximum.

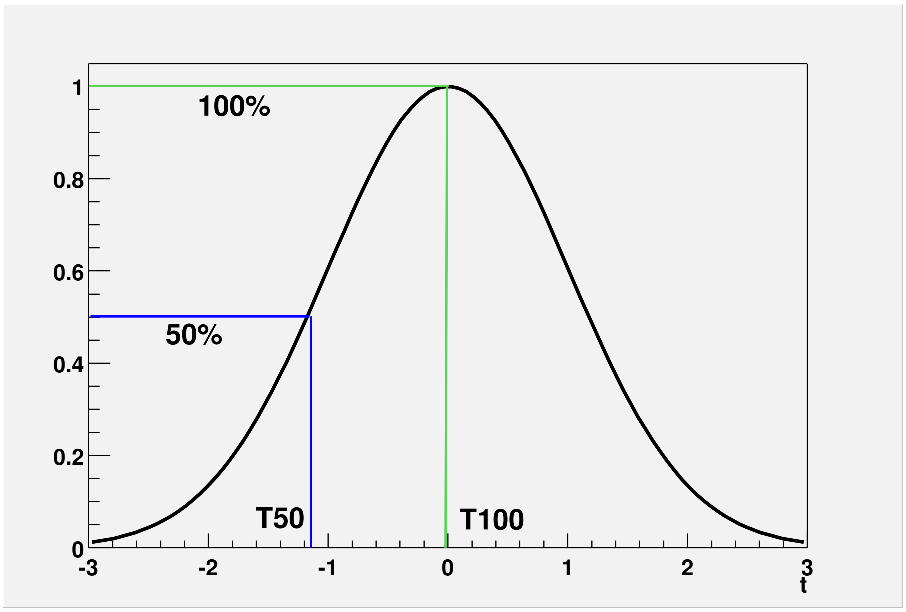

Figure 5.2: Definitions of T^{50} and T^{100}.

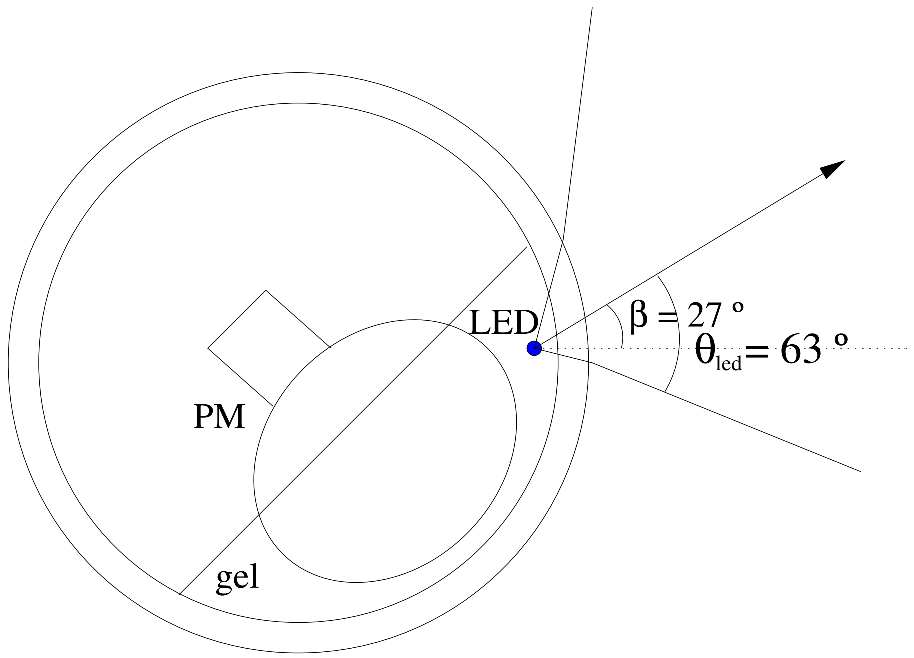

Figure 5.3: Simulated LED location in the Optical Module.

5.2 Single LEDs

In this section, the results of the simulation of the timing calibration with a single LED in each Optical Module are presented. In Figure 5.3, the location of the LED in the Optical Module is shown. Light emitted from the LED is isotropically distributed in a cone with a half angle $\theta_{LED} = 63°$. We have assumed that the time distribution of the pulse is Gaussian. The LED is pointing 27° over the horizontal.

In Table 5.1, a summary of the main features of this simulation is shown. The main characteristics of the detector can be seen in Table 5.2. It has the usual spiral geometry (Figure 5.4), but in order to save CPU time, the number of storeys has been reduced to ten. Without these redundant intermediate storeys the analysis becomes faster.

The left part of the arrival time distributions after 10^4 flashes is fitted to a Gaussian to obtain T^{100} and T^{50} (see Section 5.1). The excellent level of redundancy expected in this configuration is confirmed by our simulation, as seen in Figure 5.5. The upper plot gives the number of LEDs illuminating each PMT, the average being larger than 50. In addition, every PMT is illuminated by at least two LEDs. A hint of the 13-line structure of the detector can be seen in the plot. Most of the photons arrive at the PMTs located in the top storeys, as expected since they are pointing below the horizontal plane. Moreover, a substructure corresponding to the three PMTs in each cluster is visible.

The bottom plot shows the number of PMTs illuminated by each LED. It can be seen that in average a LED illuminates more than 50 PMTs. As in the previous case, this number depends on the position. It is higher for the LEDs located in the bottom storeys, since the LEDs are pointing

Light source	**LED**
Wavelength	466 nm
Pulse width (FWHM)	4 ns
Angular distribution	uniform $\theta_{LED} < 63°$
Flux per flash	$5 \cdot 10^7\ \gamma$
Number of flashes	10^4
Water Model	**Medsea**
λ_{abs}	60 m
λ_{scat}	40.8 m
$\langle cos\theta \rangle$	0.8972

Table 5.1: Characteristics of the simulation of the calibration with single LEDs.

Geometry	Spiral
Number of strings	13
Distance between closest strings	~60 m
Number of storeys	10
Distance between storeys	12 m
Twist	1 deg/m

Table 5.2: Characteristics of the detector simulated in the single LED configuration.

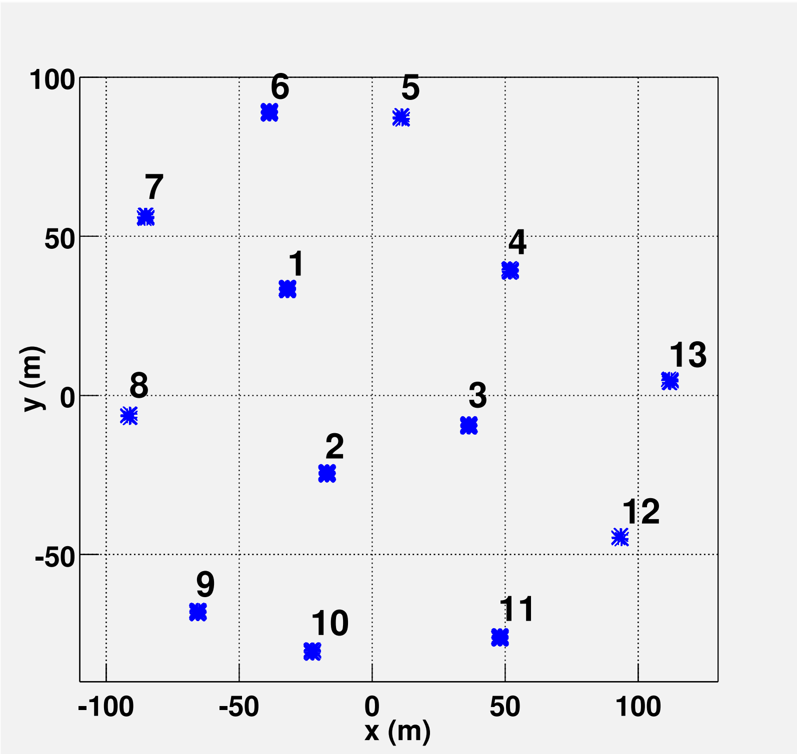

Figure 5.4: Top view of the detector with spiral geometry.

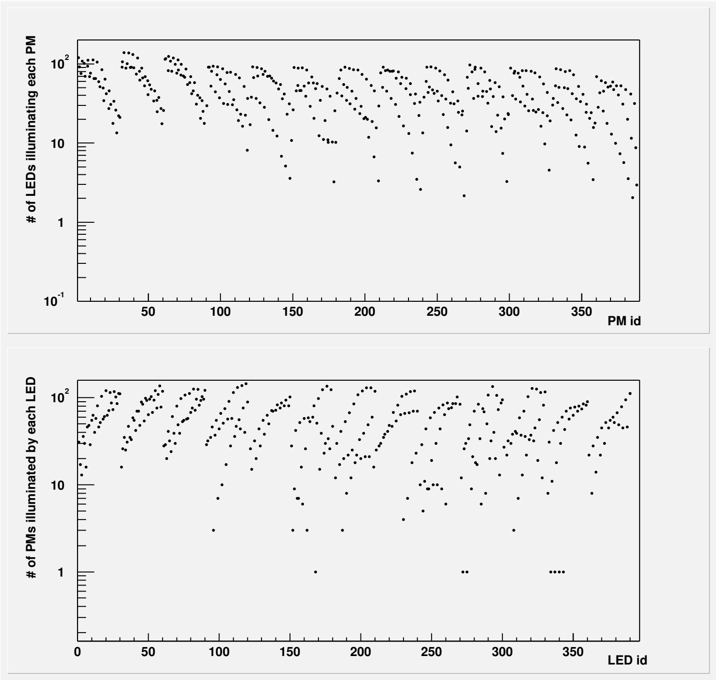

Figure 5.5: Upper plot: number of single LEDs illuminating each PMT. Lower plot: number of PMTs illuminated by each single LED.

above the horizontal plane. Furthermore, the structure of 13 lines is also visible here.

The relationship between redundancy and position can be better seen in Figure 5.6. In this plot, PMTs illuminated by three or more LEDs are marked with a white box. Dark marks indicate PMTs illuminated by only two LEDs, which amount to 1% of the total number of PMTs (4 over 390, corresponding to PMTs in the external lines pointing outside the detector).

If there was no scattering, the relationship between T^{100} and T^{50} would be $T^{100} = T^{50} +$ FWHM/2. The presence of scattering introduces a shift in these values which depends on the distance. Moreover, this shift is different for T^{100} and T^{50} ($T^{100} > T^{50} + \text{FWHM}/2$), since T^{100} is more sensitive to scattering. In Figure 5.7, T^{100} and T^{50} for all the illuminated PMT-LED pairs are plotted versus the LED-PMT distance. The data are fitted to a parabola and this correction is subtracted from T^{100} and T^{50} to calculate T_0^{100} and T_0^{50}. In the case of T_0^{50} the offset FWHM/2 due to its definition is included in the correction. This plot shows that at low distances, the distance correction is not very strong.

This distance correction depends on the source spread and the water optical properties. These dependencies are studied in detail in Subsection 5.2.1 and 5.2.2.

Due to the high level of redundancy, several values of T_0^{100} and T_0^{50} can be obtained, since a number of LEDs can illuminate each PMT. For instance, PMT 151 is illuminated by 90 LEDs. The distribution of the T_0^{50} values given by each of them is plotted in Figure 5.8.

Most of the points are in a narrow peak around zero. There are some values of T_0^{50} larger than 1 ns, corresponding to the time distributions with a small number of entries. To treat this problem, we weight each T_0^{50} by the number of entries in the arrival time distribution. The average of the mean values of T_0^{50} weighted by the number of entries are plotted in Figure 5.9 for each PMT. Only in a few cases the deviation from the expected value (T_0^{50}=0 ns) is larger than 0.2 ns.

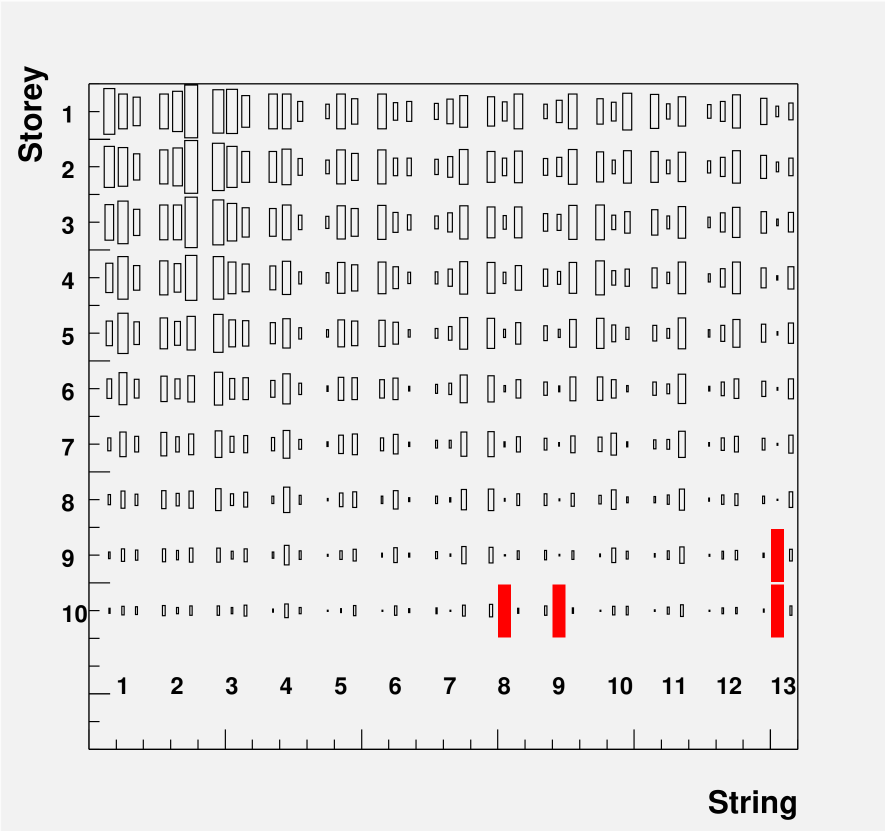

Figure 5.6: Calibrated PMTs. White boxes indicate that the PMT can be illuminated by more than two LEDs. PMTs illuminated by only two LEDs are marked with a dark box.

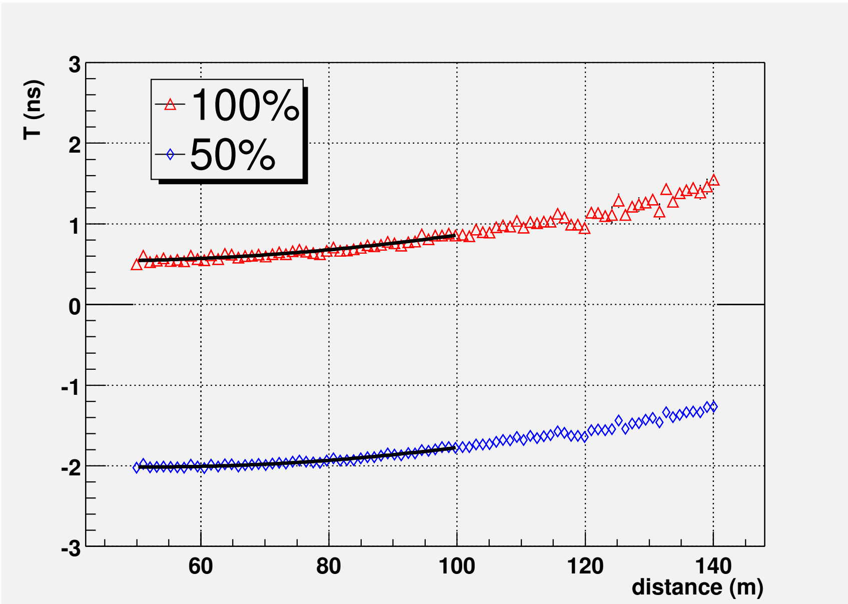

Figure 5.7: Dependence on the distance of the correction in T^{100} and T^{50}.

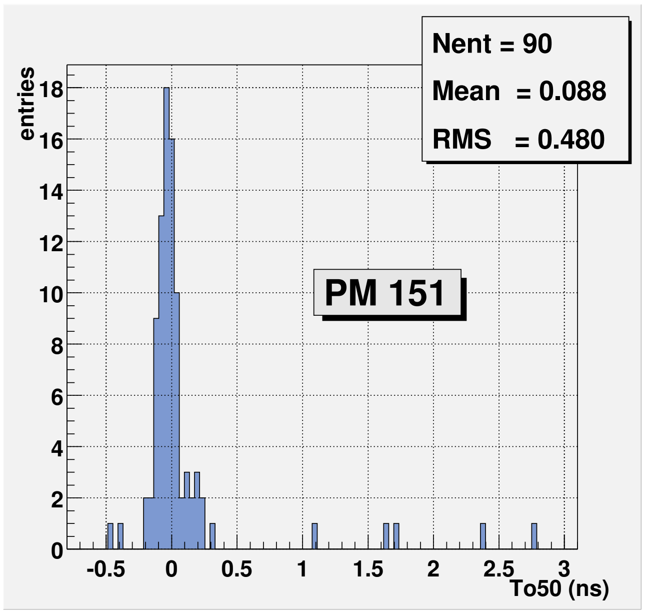

Figure 5.8: Distribution of T_0^{50} for PMT=151.

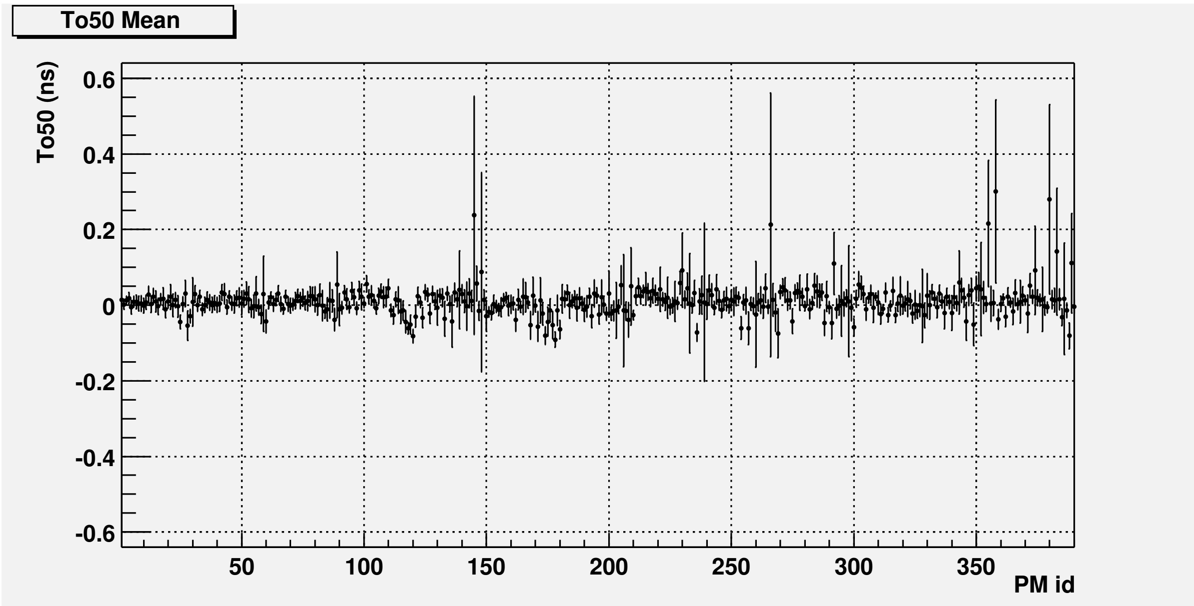

Figure 5.9: Average value of T_0^{50} for each PMT. Error bars are the error in the mean.

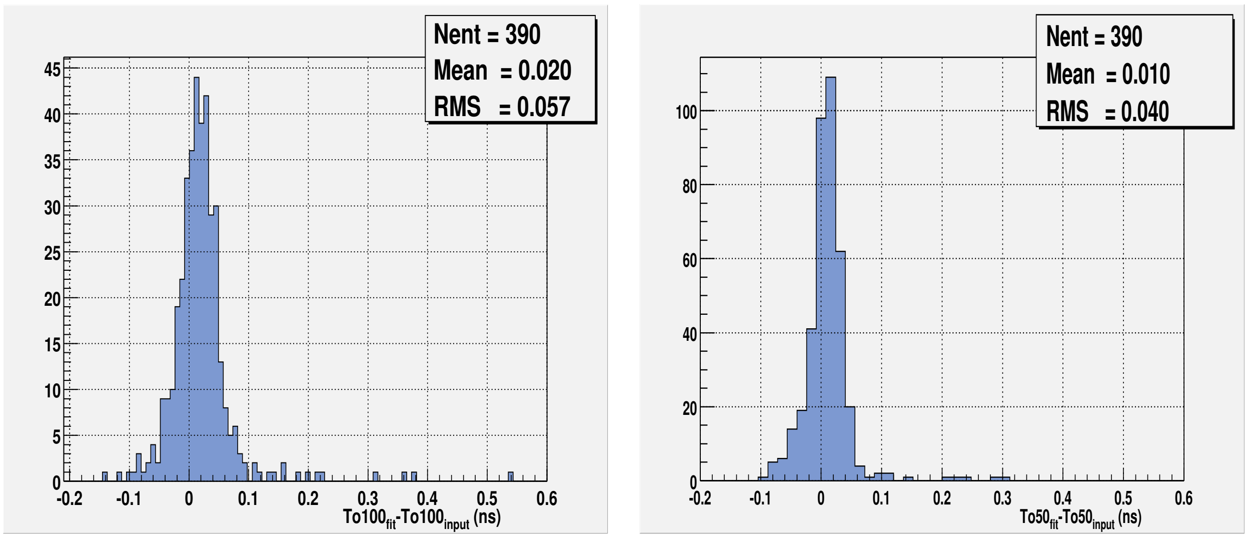

Figure 5.10: Distribution of the estimated T_0^{100} (left) and T_0^{50} (right).

The quality of the reconstruction can be seen in Figure 5.10, where the difference between the corrected T_0 and the real T_0 (equal to zero by construction) is plotted, showing that 98% of photomultipliers are within ±0.2 ns.

5.2.1 Systematics from FWHM$_{LED}$

The distance correction curves depend on the FWHM of the LED and the scattering. In the previous analysis, perfect knowledge of these two factors was assumed. In this subsection the effect of the uncertainty in FWHM$_{LED}$ is studied.

Figure 5.11 shows the correction curves for several values of FWHM$_{LED}$. The effect on T^{100} is small as it is expected, since T^{100} gives the position of the peak which should not depend on FWHM$_{LED}$. The differences are a residual effect from scattering. However, the differences among the correction curves in the case of T^{50} are larger, since there is a direct relationship between the spread of the source and T^{50}.

From the previous plot, it is possible to estimate that an uncertainty in the spread of the source of 10% gives an error ∼0.2 ns in T_0^{50}, while the systematic in T_0^{100} is negligible, both at a distance of 80 m.

5.2.2 Systematics from the water optical properties

A study of the systematics due to the water optical properties has been made. Three different water models have been used. In Table 5.3, the parameters of each model are shown. The first one is **Medsea**, which is the model used in the previous analysis.

The model **Med301** has been built to have a shorter scattering length but with the same effective scattering length (see Eq. 1.12) than **Medsea**. The last model, **Med302**, is similar to **Med301**, but with a lower value of $\langle \cos\theta \rangle$, and hence, more diffusive. The relationship between the scattering length and the average cosine is plotted in Figure 5.12.

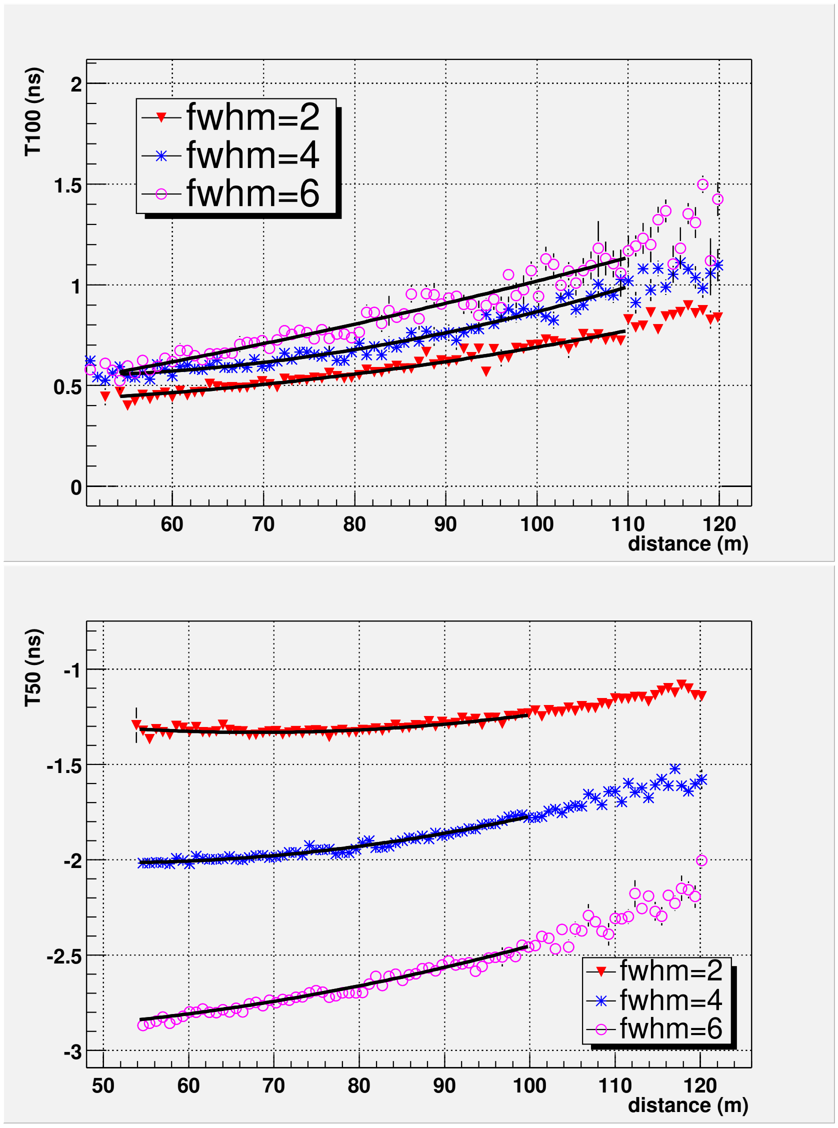

Figure 5.11: Correction curves as a function of distance for T^{100} (top) and T^{50} (bottom) for FWHM$_{\text{LED}}$=2, 4 and 6 ns.

Model	λ_{abs} **(m)**	λ_{scat} **(m)**	$\langle cos\theta \rangle$	λ_{eff} **(m)**
Medsea	60	40.8	0.8972	396.8
Med301	60	30	0.9244	396.8
Med302	60	30	0.87	230.7

Table 5.3: Parameters of the studied water models.

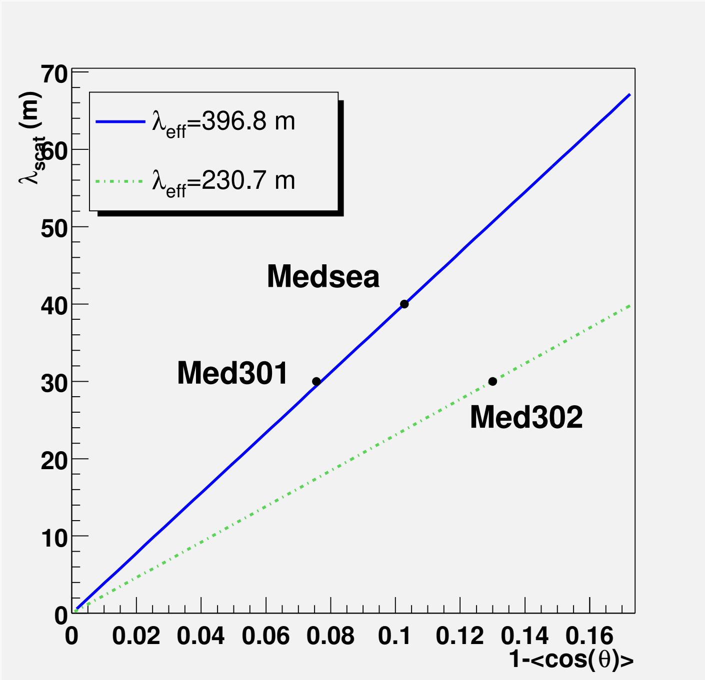

Figure 5.12: Relationship between the scattering length and $1-\langle cos\theta \rangle$ for the different models studied. Straight lines are drawn to indicate models with the same λ_{eff}.

	ΔT_0^{100} (ns)	ΔT_0^{50} (ns)
FWHM of the source $\Delta FWHM = 0.4\ ns$	∼0	∼0.2
Water model medsea→med302	∼0.5	∼0.3

Table 5.4: Estimation of the systematics due to the uncertainty in the FWHM of the source and in the water model at a distance of 80 m.

The different distance correction curves obtained with these models can be seen in Figure 5.13. There are two important conclusions that can be drawn from these results. Firstly, it is clear that T_0^{50} is less affected by the water optical properties than T_0^{100}. This was expected since the earlier photons have been less affected by scattering. Secondly, it becomes clear that, even for the two models with the same effective length, **Medsea** and **Med301**, there is a difference in the correction curves.

From the differences among the previous curves, the uncertainty due to the water model can be estimated. For instance, a pessimistic case would be to assume **Medsea** as water model, being **Med302** the correct model. At a distance of 80 m, the error in T_0^{50} would be ∼0.3 ns and in T_0^{100} would be ∼0.5 ns.

In Table 5.4 a summary of the estimation of the systematics due to the uncertainty in the FWHM of the source and in the water model is presented.

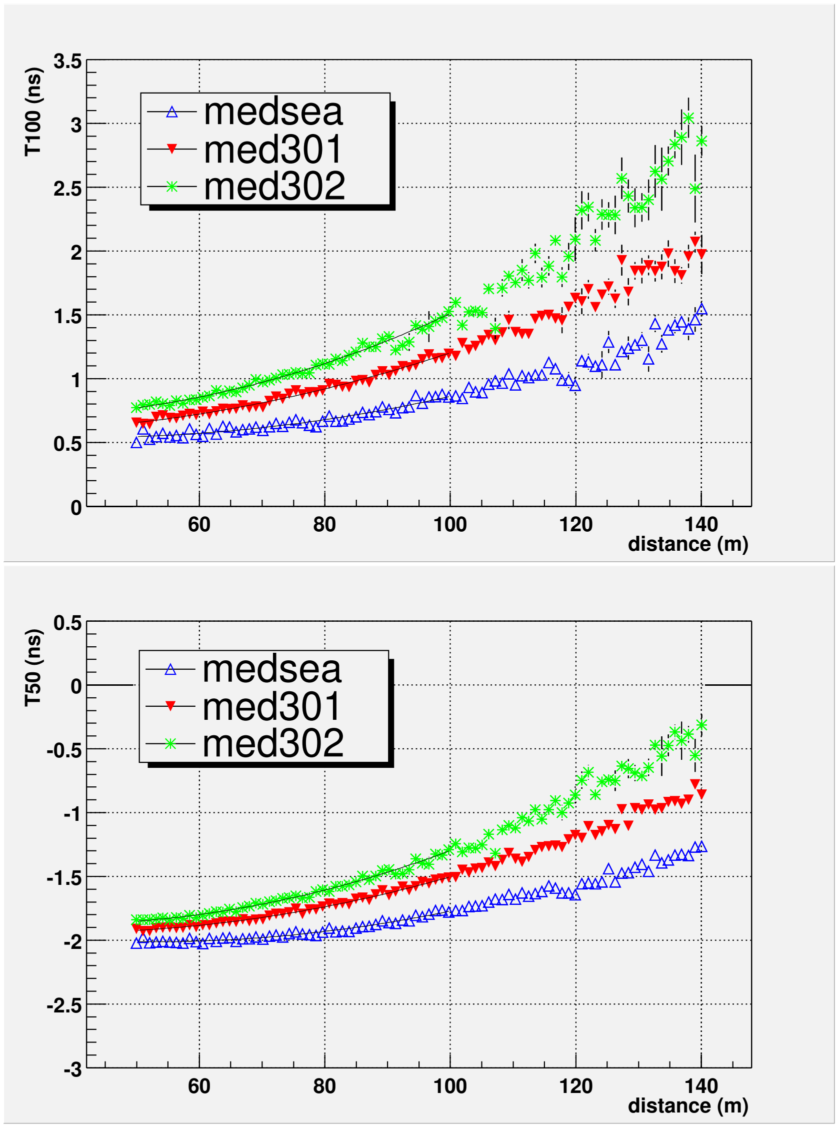

Figure 5.13: Correction curves as a function of distance for T^{100} (top) and T^{50} (bottom) for the three water models considered.

5.2.3 Estimation of $\sigma_{LED} \otimes \sigma_{TTS}$

In Figure 5.10, a comparison between the T_0 obtained from the Gaussian fit and the real T_0 was presented. A similar comparison can be made between the σ of that fit and the convolution of σ_{LED} and σ_{TTS}. The difference between σ_{fit} and $\sigma_{input} = \sqrt{\sigma^2_{LED} + \sigma^2_{TTS}}$ can be seen in Figure 5.14.

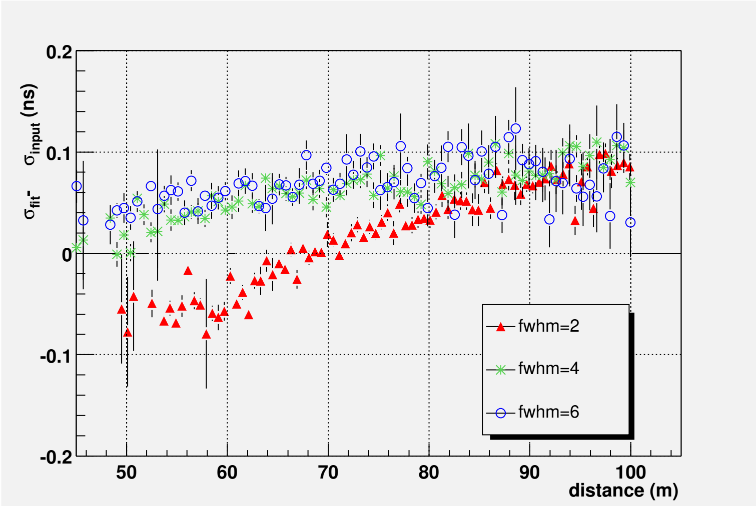

Figure 5.14: Difference between σ_{fit} and σ_{input} for **Medsea** as a function of distance.

As it can be seen, scattering introduces a positive shift (the difference would be zero without scattering) since it not only moves the peak of the time distribution, but also makes it wider. As in the case of displacement of the peak, the effect increases with the distance.

On the other hand, it has to be noted that we have assumed to be at the one photoelectron level. This is not true at low distances and therefore, σ_{fit} is overestimated, since the contribution from the photomultiplier is in fact $\sigma_{TTS}/\sqrt{Q}$, being Q the number of photoelectrons. This effect is larger for FWHM$_{LED}$=2 ns, i.e. when the response of the photomultiplier has more influence.

5.3 LED beacons

Although the system presented in the previous section allows an excellent level of redundancy, the more intense light pulse required may not be compatible with the monitoring of the transit time of the photomultiplier described in Section 4.1.

An alternative to this calibration system is the configuration with several LED beacons in each independent string. This system would allow to calibrate all the detector at the level of one photoelectron. Figure 5.15 shows a side view of two lines of the detector with this configuration.

The main characteristics of the simulation are shown in Table 5.5. The most relevant differences with respect to the study of the single LED beacons are the angular distribution and the location of the sources.

The complete version of the detector, i.e. with 30 storeys, has been used, as it can be seen in Table 5.6. No twist has been considered.

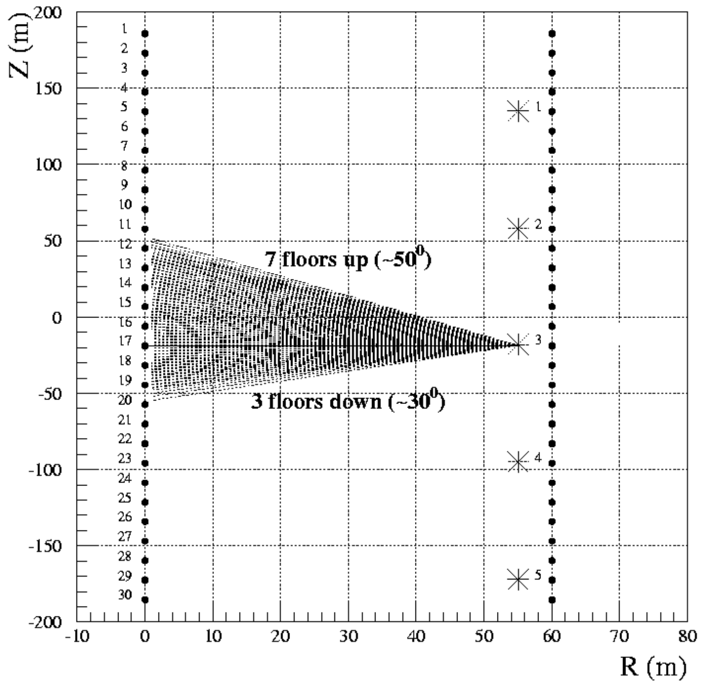

Figure 5.15: Side view of two lines of the detector to illustrate the calibration configuration with LED beacons.

Light source	**LED**
Wavelength	466 nm
Pulse width (FWHM)	4 ns
Angular distribution	uniform $50° < \theta < 120°$
Flux per flash	$7 \cdot 10^7\ \gamma$
Number of flashes	10^4
Location	along the string
Water Model	**Medsea**
λ_{abs}	60 m
λ_{scat}	40.8 m
$\langle cos\theta \rangle$	0.8972

Table 5.5: Characteristics of the simulation of the calibration with LED beacons.

Geometry	Spiral
Number of strings	13
Distance between closest strings	~60 m
Number of storeys	30
Distance between storeys	12 m
Twist	0 deg/m

Table 5.6: Characteristics of the detector simulated in the LED beacons configuration.

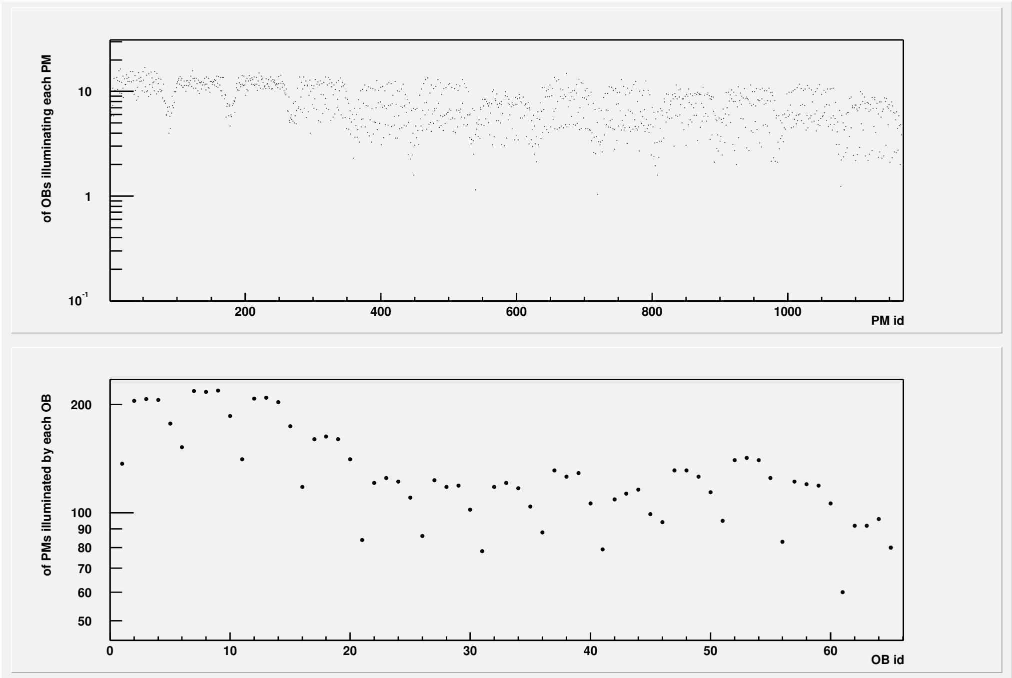

Figure 5.16: Top: Number of LED beacons illuminating each PMT. Bottom: Number of PMTs illuminated by each LED beacon.

As in the previous case, the first point to study is the level of redundancy achieved with this configuration. The results are shown in Figure 5.16. In the upper plot, the number of LED beacons illuminating each PMT can be seen. Again, a structure of 13 bumps appears corresponding to the 13 lines of the detector. The PMTs placed in its centre are illuminated by more LED beacons than those which are in the external strings. Within each string, those PMTs placed in the middle are best calibrated. However, the situation is not symmetric because the Optical Modules are oriented 45° downwards. Furthermore, PMTs located at the bottom storeys see less LED beacons than those in the upper storeys.

Concerning the bottom plot, similar remarks can be made. On one hand, the LED beacons in the central lines illuminate more PMTs, as it is expected. In addition, the LED beacons located in the centre of each line illuminate more PMTs. Finally, the beacons in the lowest storeys illuminate a larger number of PMTs than those in the upper storeys, a fact related to the orientation of the Optical Modules.

This can be better seen in Figure 5.17. A good level of redundancy is obtained, only some PMTs

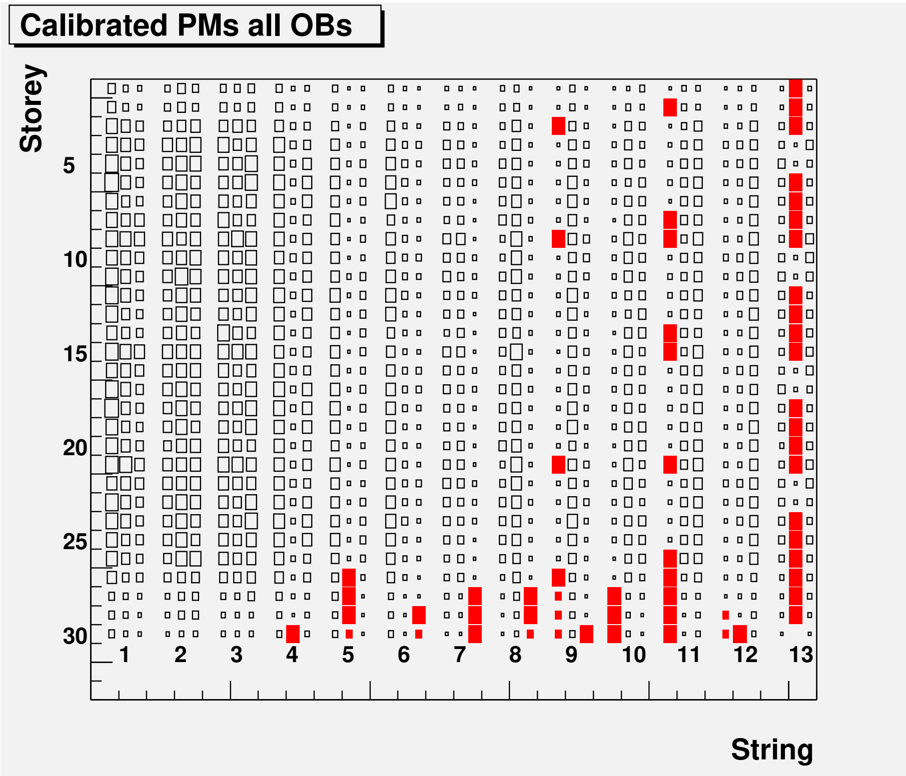

Figure 5.17: Calibrated PMTs. White boxes indicate that the PMT can be illuminated by more than two LED beacons. PMTs illuminated by only one or two LED beacons are marked with a dark box.

in the external lines and in the lowest storeys are illuminated by less than three LED beacons (dark boxes). However, when comparing with the results for the configuration with single LED beacons, it can be seen that the number of PMTs illuminated by a low number of LED beacons is larger.

The distance correction curve should be similar to the case of the single LED beacons, since it corresponds to the same wavelength. This is indeed what is obtained as it can be seen in Figure 5.18. Notice that, in this analysis, T^{90} was used instead of T^{100}.

The results of the calibration are shown in Figure 5.19. In both cases, the peaks are narrow and centred at zero, as it is expected. The mean and the RMS of these distributions are slightly worse than those corresponding to the single LED configuration, but the differences are small.

The effect of the water model in the arrival time distributions has also been studied. In addition to those with the **Medsea** model, used in the previous results, time distributions with **Global** model have also been obtained (see Figure 5.20). These results show that **Medsea** is a more diffusive model, but the differences in the rise time are small since the OB-PMT distance is of the order of λ_{scat}.

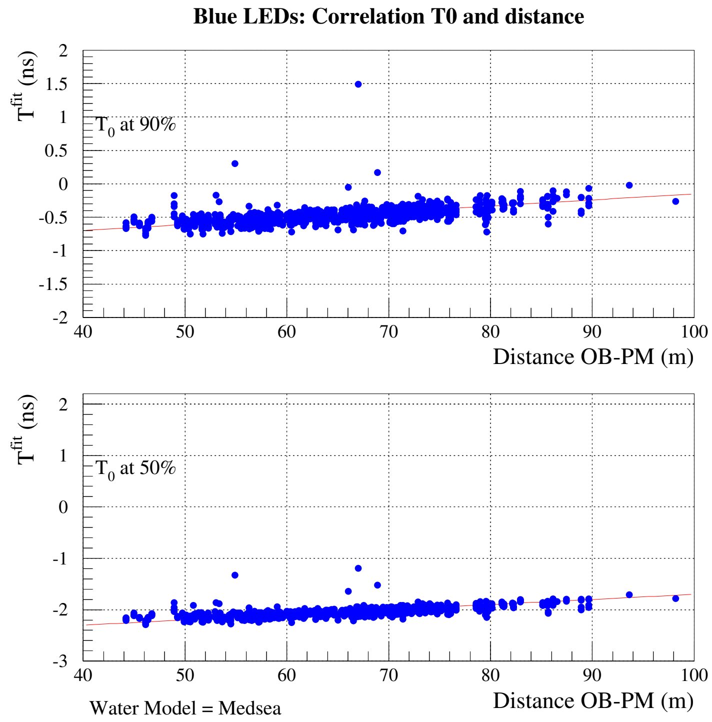

Figure 5.18: Dependence on distance of the correction in T^{90} and T^{50}.

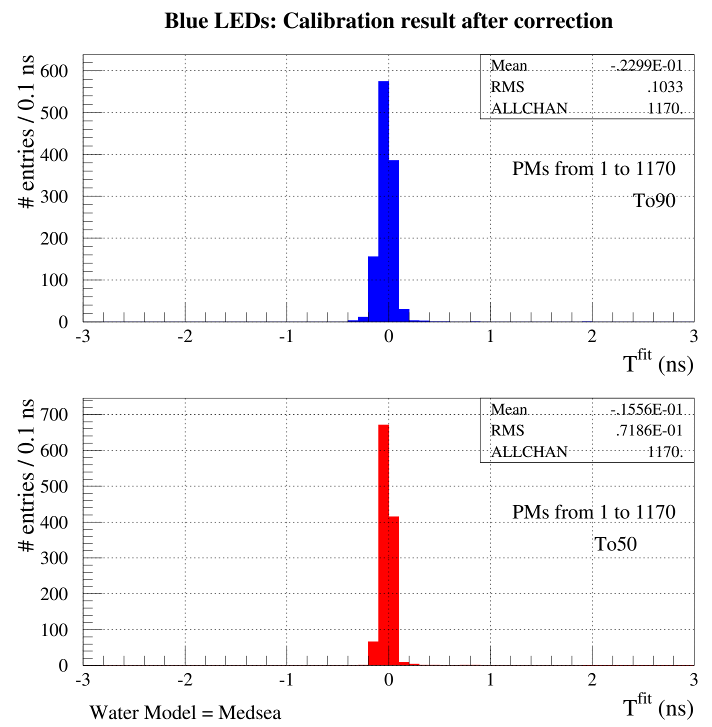

Figure 5.19: Distribution of T_0^{90} (top) and T_0^{50} (bottom).

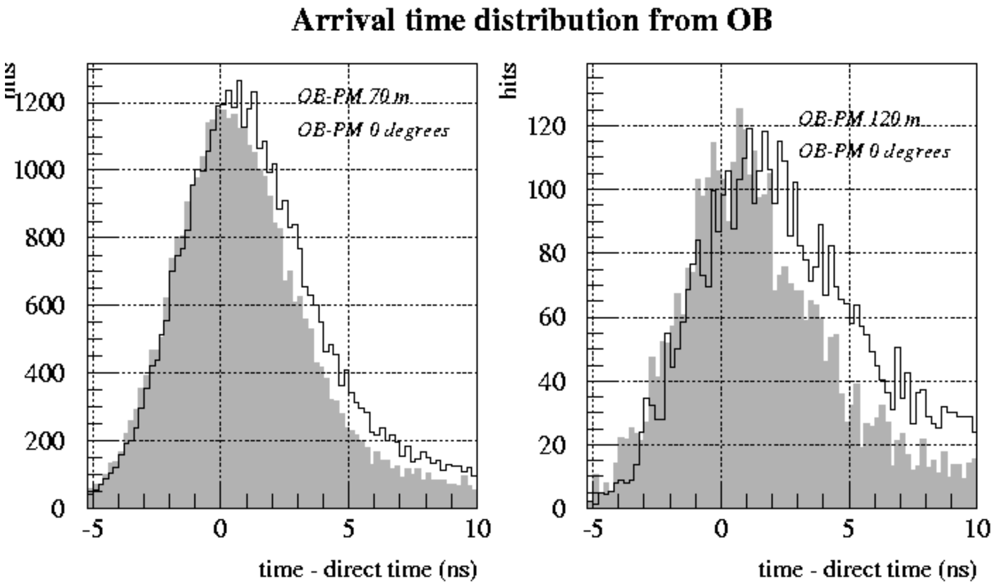

Figure 5.20: Arrival time distributions for two different OB-PMT distances: 70 m (left) and 120 m (right). Open histograms correspond to the **Medsea** model and the full histograms to the **Global** model.

5.4 Laser in the instrumentation line

The results presented in this section have been obtained using the configuration with the laser beacon in the instrumentation line. Table 5.7 shows the main features of this simulation. Note that the number of photons per flash is much higher than for the LEDs. Other advantages of the laser are its FWHM, which is of the order of 1 ns and its scattering length (longer than for the LEDs). However, since λ_{abs} is shorter for green light than for blue light, the range is limited. Two major advantages are expected with this configuration. Firstly, it would be useful to calibrate the bottom storeys, that cannot be easily reached with the LED beacons and, secondly, there will be no uncertainty in the position of the beacon, since it is at a fixed location.

The simulated detector presents an octagonal geometry with 13 strings. The main characteristics are summarized in Table 5.8. In Figure 5.21, a top view of this configuration including the instrumentation line is shown. As it can be seen, the distance from this line to the nearest one is $\sim$60 m. Two laser positions have been simulated: 30 m and 200 m above the sea bed.

The following assumptions have been made:

- The angular distribution of the source is assumed to be Lambertian ($\sim cos\theta$) to simulate the diffuser.
- Only photons emitted upwards have been considered.
- The water model simulated is the so-called **Medsea** for a wavelength of 532 nm (λ_{abs}=28.3 m and λ_{scat}=51.8 m).

Light source	**Laser**
Wavelength	532 nm
Pulse width (FWHM)	1 ns
Angular distribution	Lambertian ($\sim cos\theta$)
Flux per flash	10^{12} γ
Number of flashes	10^4
Location	instrumentation line
Water Model	**Medsea**
λ_{abs}	28.3 m
λ_{scat}	51.8 m
$\langle cos\theta \rangle$	0.8972

Table 5.7: Characteristics of the simulation of the calibration with a laser in the instrumentation line.

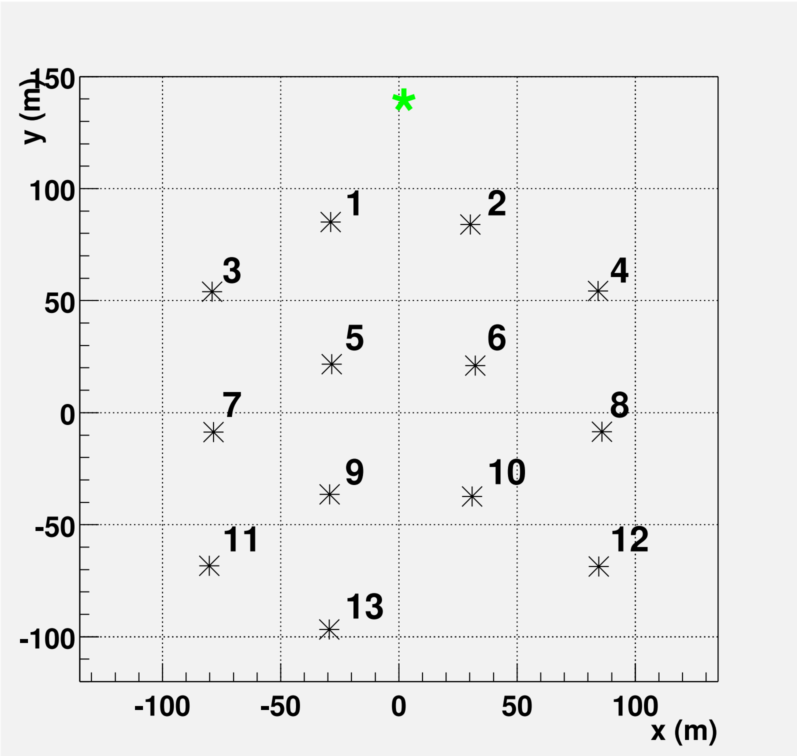

Figure 5.21: Top view of the detector and the instrumentation line. With this configuration, the distance between the detector lines and the instrumentation line goes from 60 m up to 230 m. Two laser locations have been studied: at 30 m and at 200 m from the sea bed. A star indicates the horizontal location of the instrumentation line.

Geometry	Octagonal
Number of strings	13
Distance between closest strings	~60 m
Number of storeys	30
Distance between storeys	12 m
Twist	1 deg/m

Table 5.8: Characteristics of the detector simulated in the configuration with a laser in the instrumentation line.

5.4.1 Detector calibration

The number of PMTs illuminated by the laser beacon is shown in Figure 5.22. As it can be seen, only a fraction of the detector is calibrated. Therefore, a second laser could be placed in the middle of the instrumentation line. This could allow to illuminate the upper half of the detector (see Figure 5.23) and would give some redundancy.

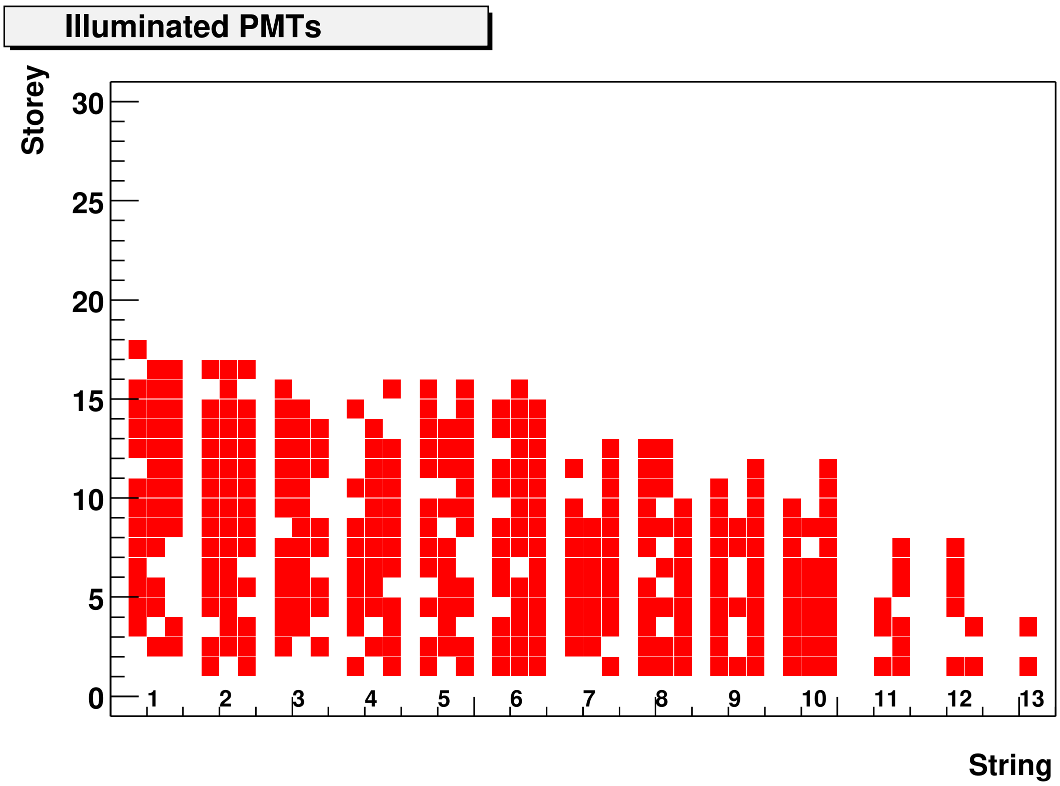

Figure 5.22: Illuminated PMTs with the instrumentation line when the laser is at 30 m from the sea bed.

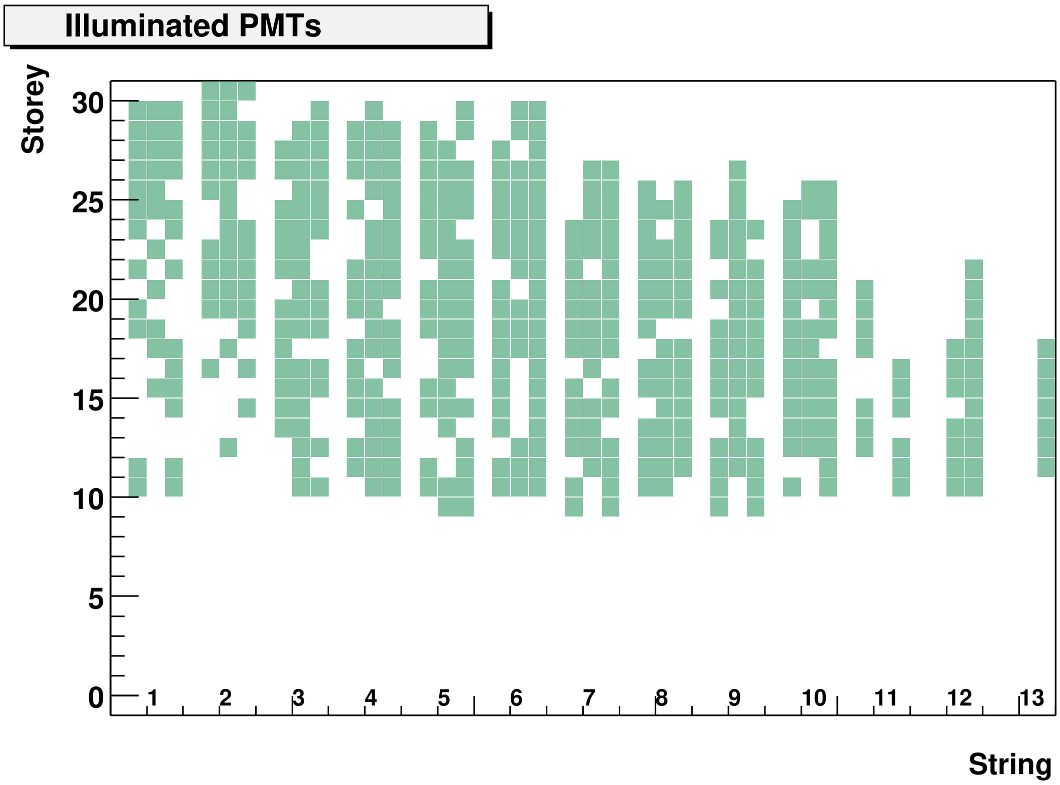

Figure 5.23: Illuminated PMTs with the instrumentation line when the laser beacon is at 200 m over the sea bed.

With this configuration, the distance correction has to be applied for larger distances than in the cases where there are more LED beacons. These curves can be seen in Figure 5.24. Comparing with Figures 5.7 and 5.18, it is clear that now the fluctuations are larger, especially in T^{100}, because the effect of the scattering increases with distance. The results can be seen in Figure 5.25. Both distributions are wider than those obtained with the single LEDs and the LED beacons.

5.4.2 Expected number of photoelectrons

It is important to study the average number of photoelectrons $\langle \#pe \rangle$ seen by each PMT.

In Figure 5.26, the dependence of $\langle \#pe \rangle$ on the distance between the Optical Module and the laser is plotted. Photoelectrons coming both from scattered and direct (not scattered) photons are included. It can be seen that the behaviour of this curve is exponential, as it is expected from absorption.

In Figure 5.27, it is compared the average number of photoelectrons coming from scattered and direct photons. In can be seen that there are much more scattered photons than direct ones.

As it can be seen in Figure 5.26, the distance between the PMT and the laser is not the only relevant variable: relative orientations are also important. For a given distance several levels of light are reached. In Table 5.9 an example is given: for three Optical Modules in the same cluster (hence, at a similar distance), different values are obtained. The higher values correspond to the best orientation, i.e. those for which the PMT is pointing to the laser.

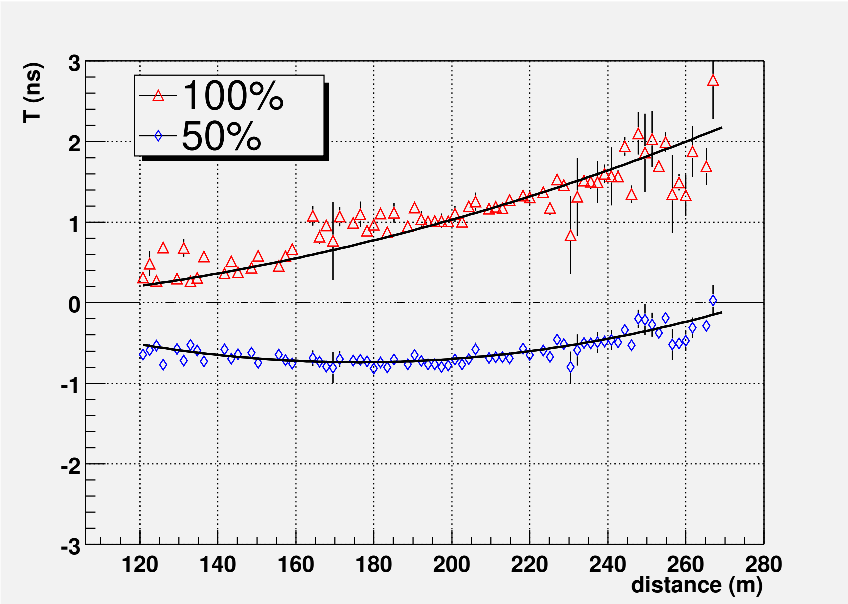

Figure 5.24: Dependence on distance of the correction in T^{100} and T^{50} for the instrumentation line configuration.

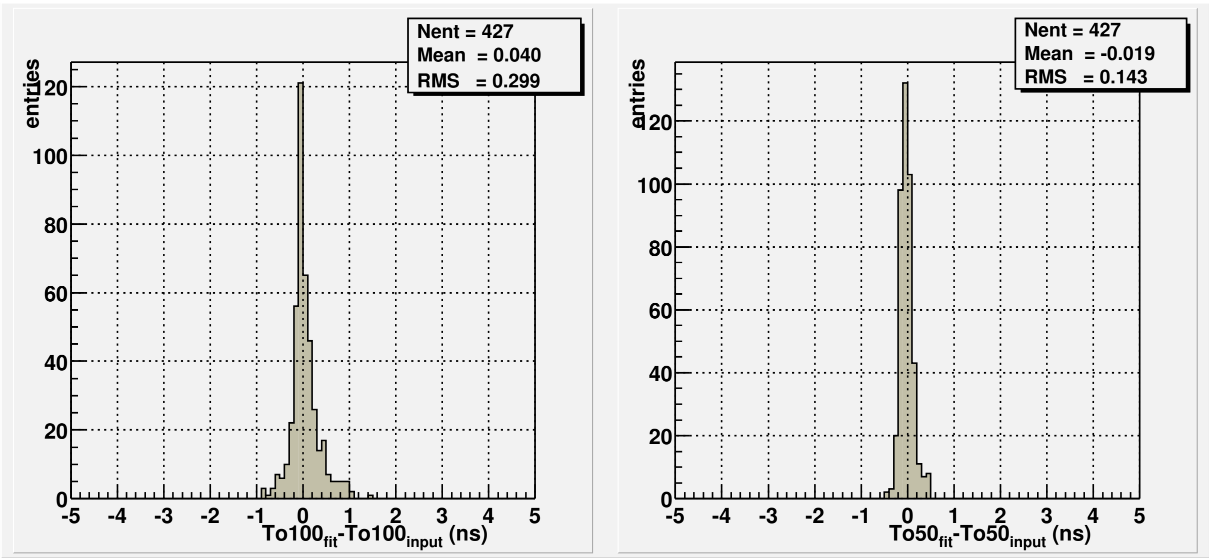

Figure 5.25: Distribution of T_0^{100} (left) and T_0^{50} (right) for the instrumentation line.

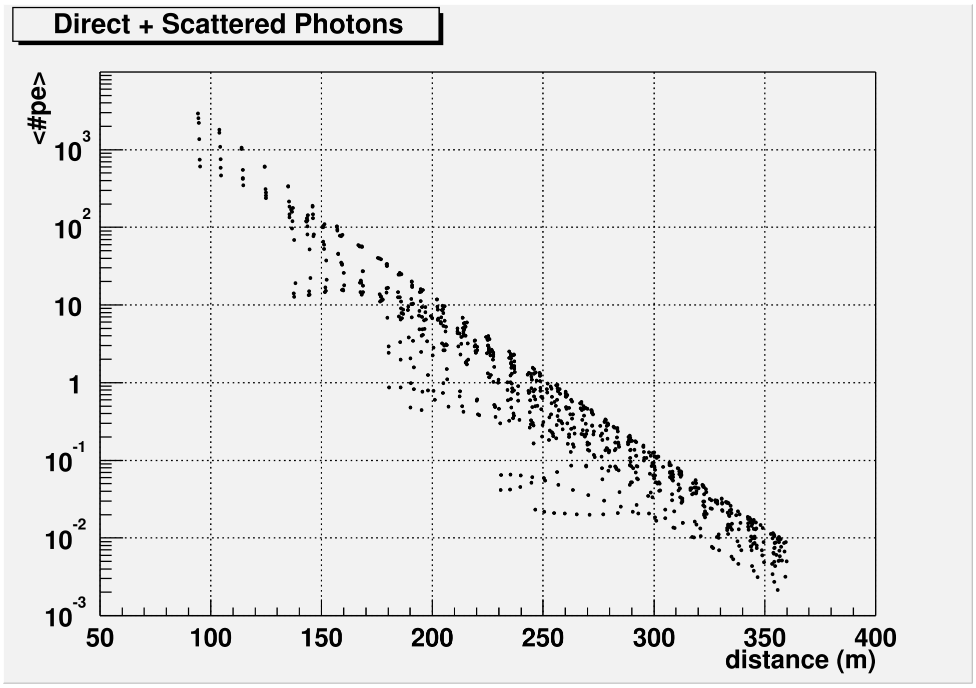

Figure 5.26: Dependence of the average number of photoelectrons on the distance between the source and the PMT. For the best orientations, the single photoelectron level is reached at 250 m.

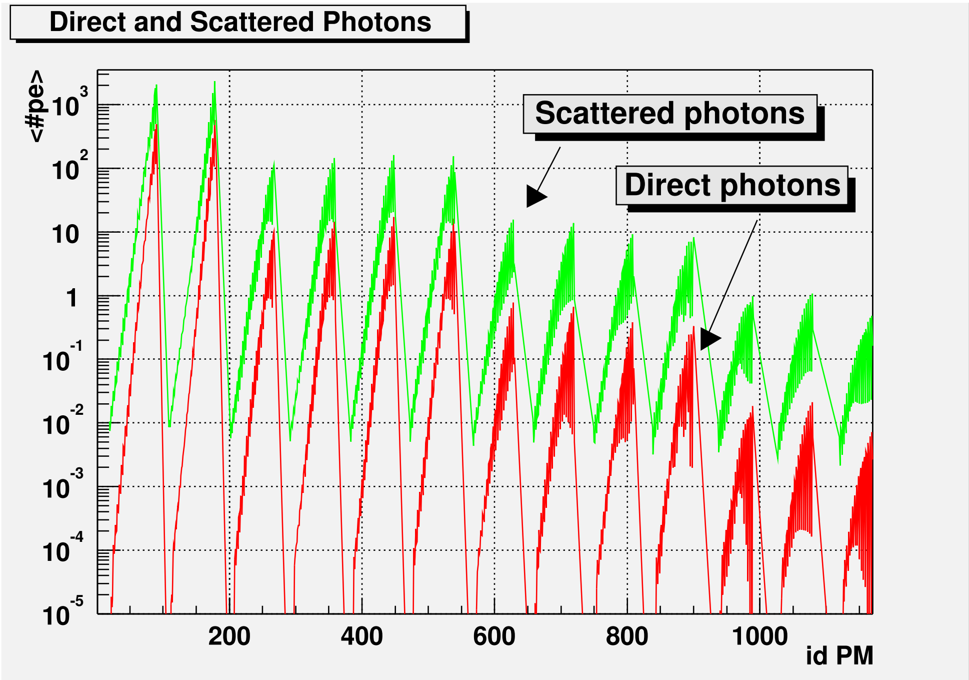

Figure 5.27: Comparison between the average number of photoelectrons coming from scattered and direct photons. The number of scattered photons is an order of magnitude larger than direct photons.

PMT id	$\langle \#pe \rangle$ **direct**	$\langle \#pe \rangle$ **scattered**	Distance laser-OM (m)	θ_{OM}
88	405.4	1795.9	94.56	133°
89	116.3	494.2	95.23	96°
90	490.5	2053.3	94.40	147°

Table 5.9: Comparison of the value of $\langle \#pe \rangle$ for three different orientations. These PMTs are in the same cluster, so the OM-laser distance is similar, as it is indicated.

In Figure 5.28, the average number of photoelectrons as a function of the band angle (defined in Figure 4.10) is shown. Figure 5.29, where the different photon yields are plotted, shows these results in a clearer way.

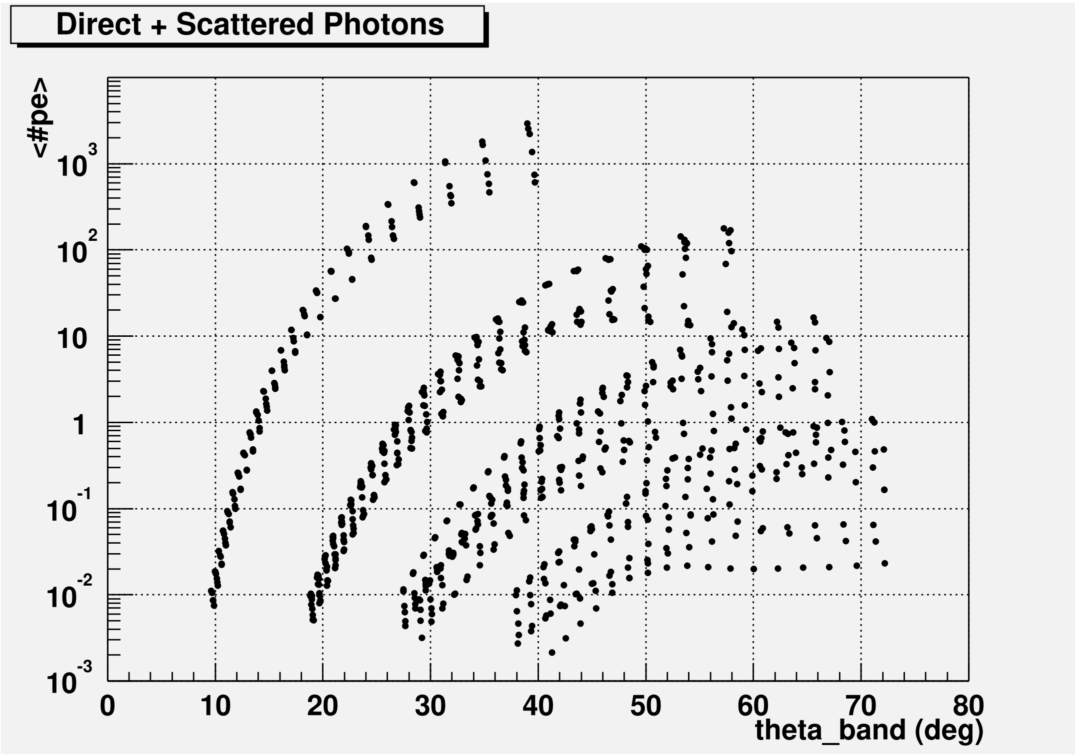

Figure 5.28: Dependence of the average number of photoelectrons on the band angle.

An important result from this plot is that only the lowest half of the detector can be properly calibrated. Due to the absorption, Optical Modules farther than 300 m are under the 0.1 photoelectron level. It may be interesting, for this reason, to add a second laser in order to illuminate the whole detector. In Figure 5.30, the illumination levels when the laser is at 200 m above the sea bed are shown. Since the light distribution covers only the upper hemisphere, the 10 lowest storeys are not illuminated. Due to string oscillations, the position of this laser would not be fixed.

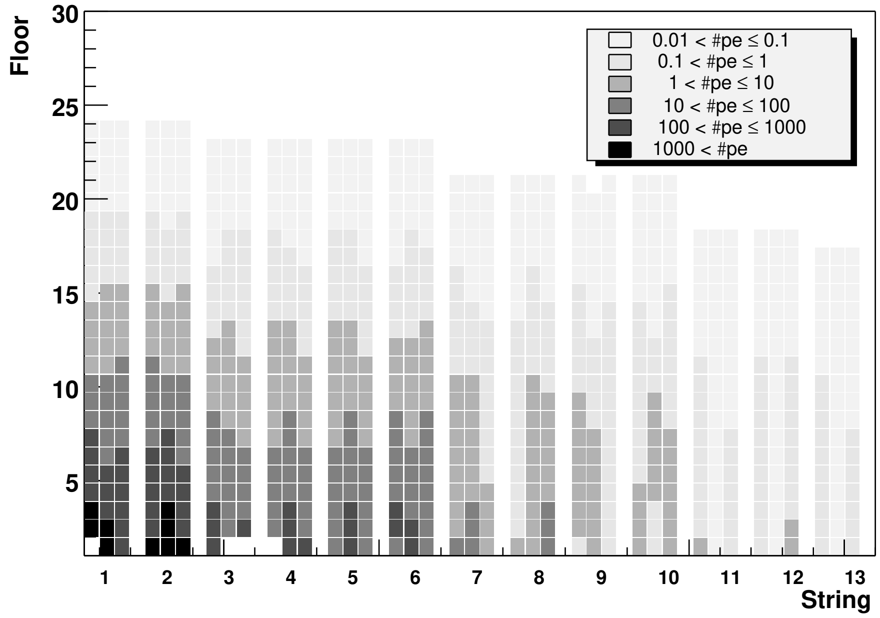

Figure 5.29: Level of lighting in each photomultiplier when the laser is at 30 m from the sea bed.

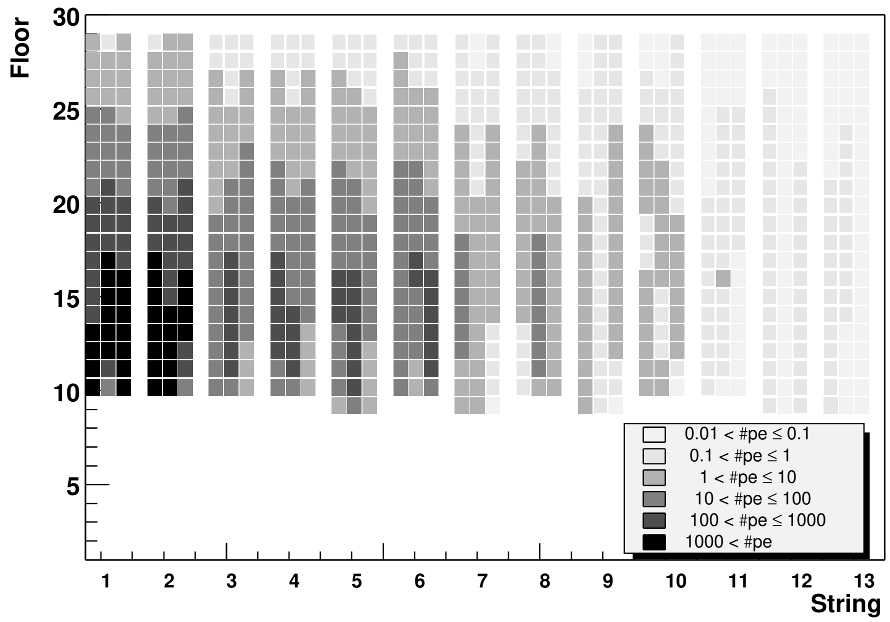

Figure 5.30: Level of lighting in each photomultiplier when the laser is at 200 m above the sea bed. The 10 lowest storeys cannot be illuminated, since the light distribution covers only the upper hemisphere.

From these plots, the distribution of the light yields can be obtained. In Figure 5.31, all the photomultipliers are classified by the average number of photoelectrons collected. With the bottom laser, roughly 70% of the PMTs collect more than 0.01 photoelectrons from a single flash. The second laser at 200 m allows all PMTs to be over 0.01 pe.

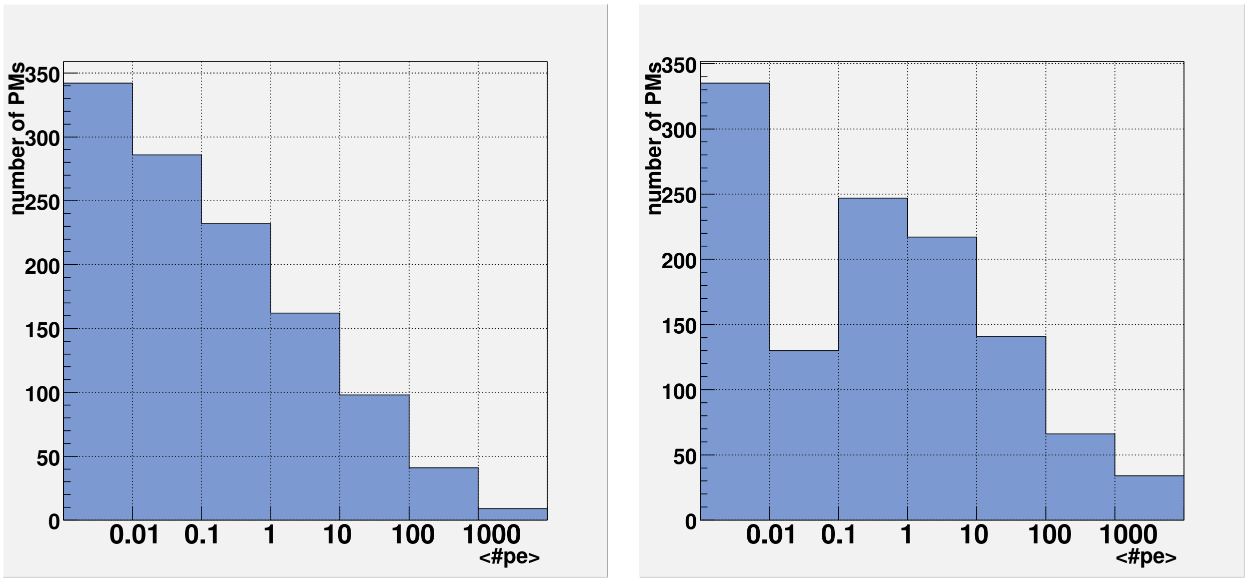

Figure 5.31: Number of the PMTs as a function of the average number of photoelectrons collected when the laser is at 30 m (left) and at 200 m (right). The first bin contains all the PMTs with $\langle \#pe \rangle$ lower than 0.01; the last bin, those with $\langle \#pe \rangle$ larger than 1000.

5.5 Summary

In Table 5.10 the results of the different calibration configuration are shown. Table 5.11 shows a summary of the advantages and drawbacks of the three studied calibration configurations. The conclusion from these results is that in order to calibrate all the detector, one of the configurations with LEDs has to be used. In addition, it is advisable to include a laser in one or more lines to calibrate the bottom storeys.

	T_0^{100} (ns)	T_0^{50} (ns)	Configuration
	0.020	0.010	Single LEDs
Mean	–0.023*	–0.016	LED beacons
	0.040	–0.019	Laser beacon
	0.06	0.04	Single LEDs
RMS	0.10*	0.07	LED beacons
	0.30	0.14	Laser beacons

Table 5.10: Summary of the results of each configuration. * These values correspond to T_0^{90}

Configuration	**Advantages**	**Drawbacks**
Single LEDs	Excellent redundancy Small scattering effect Adjustable intensity	Incompatibility with the LED used to monitor the PMT transit time Additional elements in the OM
LED beacon	Good redundancy Small scattering effect Adjustable intensity	Additional elements on the string
Laser beacon	Calibration of bottom storeys Fixed location Intense source	Large absorption effect Fixed amount of light

Table 5.11: Summary of the advantages and drawbacks of the three studied calibration configurations.

Conclusions

The work presented in this report has been developed within the context of the ANTARES project, whose aim is the deployment of a 0.1 km^2 high energy neutrino telescope in the Mediterranean sea. Two distinct topics have been tackled in this work. In the first part, two photomultiplier candidates for the ANTARES detector have been studied. The models under consideration were Photonis XP1804/D2 (10.6" photocathode diameter) and Hamamatsu R8055 (13" photocathode diameter). In the second part, several layouts proposed for a time calibration system with external light sources (Optical Beacons) have been studied by Monte Carlo simulation. Different advantages and drawbacks of each configuration have been obtained from the results of this simulation.

The main results concerning the photomultiplier characterization are the following:

- The charge spectra are well reproduced and good fits are obtained with the assumed functional dependence (Section 3.1).
- All the PMTs are able to reach a gain of $5 \cdot 10^7$. The *nominal voltage*, i.e. the voltage at which this gain is obtained, is lower for the Photonis model (1600–1750 V) than for the Hamamatsu model (1750–2000 V) (Section 3.2).
- The amplitude at the nominal voltage is higher than 50 mV only for the Photonis PMTs. The Hamamatsu *nominal amplitude* is lower than 40 mV, the value of 50 mV being reached at somewhat higher voltages, $\sim 7\%$ above the HV_{nom} (Section 3.3).
- The relationship between amplitude and gain is the same for all the tubes of the same model. In the case of the Photonis PMTs, there is a small difference between the curves (Section 3.3).
- The value of the peak to valley ratio is roughly between 3 and 4, i.e. above the specifications (P/V>2), for all the tubes except for one from Photonis (Section 3.4).
- The energy resolution is around 30% and 35% for the Photonis and Hamamatsu PMTs, respectively (Section 3.5).
- The results of TTS are good for both models. The Photonis PMTs have a TTS around 2 ns, whereas the value for the Hamamatsu PMTs is $\sim$2.6 ns. The ANTARES specifications establish a maximum value of 3 ns (Section 3.6).
- The results on dark noise show a higher rate for Hamamatsu (5–10 kHz) than for Photonis ($\sim$4 kHz), but both models are within the specifications (Section 3.7).
- The prepulse rate is very small for all the PMTs (only one of them reaches 2%). The delayed pulse rate is around 5% in all cases. The afterpulse-1 and afterpulse-2 rates are roughly 2% and 18%, respectively, i.e. twice the maximum required value (Section 3.8).

Concerning the Optical Beacon simulation, the main conclusions are:

- The Single LED configuration provides an excellent level of redundancy. This is due to the large number of sources used, which in addition allows to calibrate all the PMTs at not too large distances. Furthermore, since LEDs emit in the blue ($\lambda \sim 470$ nm), absorption effects are minimized. The reconstruction simulation shows that 98% of the photomultipliers are calibrated within ± 0.2 ns around the true value (Section 5.2).

- The LED beacons provide also good redundancy. As in the previous case, this is due to the number of sources and the emission wavelength. Only some PMTs in the external lines and in the bottom storeys could have problems to be calibrated (Section 5.3).

- The laser beacon will be a useful complementary calibration system since it will be able to illuminate bottom storeys. Moreover, if it is located at the bottom of the line, it will provide a fixed reference source. However, absorption is a major problem for the laser beacon, which precludes a global calibration of the detector (Section 5.4).

- T_0^{100} and T_0^{50}, i.e. the position of the maximum and half maximum of the arrival time distributions, have been successfully used as estimates in the reconstruction simulation. The effect of scattering on these two estimators has been corrected for (Section 5.1).

- An uncertainty in the FWHM of the source of 10% gives a systematic error ~ 0.2 ns in T_0^{50} at 80 m and does not affect T_0^{100} (Subsection 5.2.1).

- The systematics due to the uncertainty in the water model are ~ 0.3 ns for T_0^{50} and ~ 0.5 ns for T_0^{100} at 80 m (Subsection 5.2.2).

Bibliography

[1] M. A. Markov. In *Proceedings of the Rochester Conference, New York (1960).*

[2] ANTARES Collaboration. "A deep sea telescope for high energy neutrinos". *astro-ph/9907432*, 1999.

[3] E. Carmona. "Estudio de fotomultiplicadores de gran fotocátodo para el teslescopio submarino de neutrinos ANTARES". *Trabajo de Investigación (1999), Universidad de Valencia.*

[4] The high resolution Fly's Eye ultra high energy cosmic ray observatory. *http://hires.physics.utah.edu/.*

[5] D.C. Ellison et al. *ApJ 487 (1997) 197.*

[6] E.G. Berezhko et al. *JETP 82 (1996) 1.*

[7] D.J. Bird et al. *Phys. Rev. Lett. 71 (1993) 3401.*

[8] M. Takeda et al. *Phys. Rev. Lett. 81 (1998) 1163.*

[9] K. Greisen. *Phys. Rev. Lett. 16 (1966) 748.*

[10] V.A. Kuzmin G.T. Ztseptim. *JETP Lett. 4 (1966) 78.*

[11] EGRET Collaboration. "The second EGRET catalog of high energy gamma ray sources". *http://cossc.gsfc.nasa.gov/cossc/egret/.*

[12] T.Kifune. "CANGAROO experiment". In *Very High Energy Phenomena in the Universe, XXXVIth Rencontres de Moriond, Les Arcs (France).*

[13] HEGRA Collaboration. "The energy spectrum of TeV gamma-rays from the Crab Nebula as measured by the HEGRA system of imaging air Cherenkov telescopes". *The Astroph. J., Volume 539 (2000), Issue 1, pp. 317.*

[14] M. Punch et al. *Nature 358 (1992) 477.*

[15] D. Petry et al. *Astron. Astrophys. 311 (1996) L13.*

[16] F. Halzen. "The case for a kilometer-scale high energy neutrino detector". In *16th International Conference on Neutrino Physics ad Astrophysics (Neutrino 94), Eilat, Israel (1994).*

[17] W. Berezinsky et al. *Astropysics of Cosmics Rays.* North-Holland, 1990.

[18] J.F.C. Wardle et al. *Nature 395 (1998) 457.*

[19] M.C. Begelman et. *Ap. J. 362 (1990) 38.*

[20] INTEGRAL Science Data Center. *http://obswww.unige.ch/isdc/.*

[21] E. Waxman and J. Bachall. High energy neutrino from cosmological gamma ray burst fireballs. *Phys. Rev. Lett. 78 (1997) 2292.*

[22] A. Dar and A. De Rújula. "The cannonball model of gamma ray bursts: spectral and temporal properties of the gamma rays". *astro-ph/0012227.*

[23] P. Bhattacharjee and G. Sigl. *astro-ph/9811011.*

[24] D. Casper et al. *Phys. Rev. Lett. 66 (1991) 2561.*

[25] W.W.M. Allison et al. *Phys. Lett. B391 (1997) 491.*

[26] Y. Fukuda et al. *Phys. Rev. Lett. 81 (1998) 1562.*

[27] F. Halzen and D. Saltzberg. *Phys. Rev. Lett. 81 (1998) 4305.*

[28] G. Mignola A. Bottino, N. Farnengo and L. Moscoso. *Astropart. Phys. 3 (1995) 65.*

[29] P. Gondolo and J. Silk. "Dark matter annihilation of the galactic center". *MPI-PhT/99-10; OUAST/99/9, March 1999.*

[30] R. Ghandi et al. *Astropart. Phys. 5 (1996) 81.*

[31] L. V. Volkova. "Energy spectra and angular distributions of atmospheric neutrinos". *Sov.J.Nucl.Phys.31:784-790,1980, Yad.Fiz.31:1510-1521*, 1980.

[32] F.W. Stecker, C. Done, M.H. Salamon and P. Sommers. "High energy neutrinos from active galactic nuclei". *Phys. Rev. Lett. 66 (1991) 2697.*

[33] L. Nellen, K. Mannheim, and P.L. Biermann. *Phys. Rev. D477 (1993) 5270.*

[34] K. Mannheim. "High energy neutrinos from extragalactic jets". *Astropart. Phys. 3 (1995), 295.*

[35] R.J. Protheroe. "High energy neutrinos from blazards". *astro-ph/9607165*, 1996.

[36] P. Bhattacharjee. "Ultra high energy cosmic rays from topological defects (cosmic strings, monopoles, necklaces and all that)". *hep-ph/9803029*, 1998.

[37] G. Sigl. "Topological defect models of ultrahigh energy cosmic rays". *astro-ph/9610221*, 1996.

[38] ANTARES Collaboration. "Conceptual design report of the 0.1 km^2 detector". *1 C00 01 02 A, ANTARES internal document*, 1999.

[39] P. Amrarm et al. ANTARES collaboration. "Background light in potential sites for the ANTARES undersea neutrino telescope". *Astropart. Phys. 13 (2000) 127-136.*

[40] E. Aslanides et al. ANTARES Collaboration. "The fouling of optical surfaces in the ANTARES site". *ANTARES-Site/2001-003, ANTARES internal note.*

[41] DUMAND Collaboration. "DUMAND experiment". *http://dumand.phys.washington.edu/.*

[42] G.V. Domogatsky. The baikal project: status report. In *XIX International Conference on Neutrino Physics ad Astrophysics, Sudbury Canada, June 2000.*

[43] S. Barwick. Results from amanda. In *XIX International Conference on Neutrino Physics ad Astrophysics, Sudbury Canada, June 2000.*

[44] L.K. Resvanis. Nestor. In *TAUP 99, Nucl. Phys. B 87 (2000) 448.*

[45] C. De Marzo. Feasability studies for a Mediterranean neutrino obsevatory. The NEMO.RD project. In *TAUP 99, Nucl. Phys. B 87 (2000) 433.*

[46] Hamamatsu Photonics K. K. *Photomultiplier Tube.* 1994.

[47] Phillips Photonics. *Photomultiplicateurs.* Phillips, 1994.

[48] E. Carmona and S. Basa. "Study of two Nd-YAG lasers as potential light sources for the ANTARES test 3' and optical beacon". *ANTARES-Cali-/2000-001, ANTARES internal note.*

[49] S. Basa and H. Lafoux. "Photomultiplier specifications for the ANTARES Project". *ANTARES-Opmo/1999-002, ANTARES internal note.*

[50] J.D. Zornoza and E. Carmona. "Results of the tests performed in Valencia on four 13" Hamamatsu and two 10.6" photomultipliers". *ANTARES-Opmo/2000-13, ANTARES internal note.*

[51] *MINUIT, Function Minimization and Error Analysis. F. James. CERN Lybrary.*

[52] V. Bertin et al. "Conclusions of the Time Calibration Committee: The time calibration systems in ANTARES". *ANTARES-Cali/2000-007, ANTARES internal note.*

[53] C. Olivetto and F. Réthoré. "Numerical clock distribution for ANTARES (Proposal)". *3 LCM 03-01 C, ANTARES internal document.*

[54] J.E. McMillan, L.F. Thompson, R.A. Brook. "Specifications and performance of the optical module LED pulser". *3INS-0301-A, ANTARES internal note.*

[55] J.S. Kapustinsky et al. *NIM A241 (1985) 612-613.*

[56] A. Capone and V. Valente. "A proposal for the ANTARES instrumentation line". *3 INS 05 02 A, ANTARES internal note.*

[57] V. Roca et al. "Specifications and design of the laser beacon". *3 INS 04 01 A, ANTARES internal note.*

[58] N. de Botton and F. Feinstein. "Another calibration system". *ANTARES-Opmo/2000-5, ANTARES internal note.*

[59] N. de Botton and P.H. Carton. "Measurement of the light output from the optical module LED in the ANTARES test water tank". *ANTARES-Opmo/2000-14, ANTARES internal note.*

[60] S. Navas. *Calibob Package, ANTARES Software.*

[61] S. Navas and L. Thompson. "KM3 user guide and reference manual". *ANTARES-Soft/1999-011, ANTARES internal note.*

[62] A. Cade et al. H. Lafoux. "Late(st) Gamelle results". *ANTARES-Opmo/1998-001, ANTARES internal note.*

[63] F. Cassol. "GENDET 1.0: a program to generate detector files". *ANTARES-Soft/1999-007, ANTARES internal note.*

[64] S.A. Khanaev and A.F. Kuleshov. Measurement of water transparency South-West of Greece. In *Proc. 2nd NESTOR Inter. Workshop.*

[65] C.D. Mobley. *Light and water (Radiative transfer in natural water.* Academic Press, 1994.

[66] L.C. Henyey and J.L. Greenstein. "Diffuse radiation in the galaxy". *Astrphys. J. Vol.93, 70-83 (1941).*

[67] N. Palanque-Delabrouille. "Light transmission in the ANTARES site. Measurement in blue light". *ANTARES-Site/1999-003, ANTARES internal note.*

[68] A. Morel and H. Loisel. "Apparent optical properties of oceanic water: dependence on the molecular scattering contribution". *Applied Optics, Vol.38, No.21 (1998).*

[69] T.J. Petzold. "Volume scattering functions for selected ocean waters". *Scripps Inst. Oceanogr. La Jolla, 79 pp.*

[70] S. Navas. "Timing calibration with an Optical Beacon". *ANTARES-Cali/1999-001, ANTARES internal note.*

[71] S. Navas, J.D. Zornoza and J. Zúñiga. "More about timing calibration with an Optical Beacon". *ANTARES-Cali/2000-006, ANTARES internal note.*

[72] J.D. Zornoza, J. Zúñiga and S. Navas. "Timing calibration with Single LEDs". *ANTARES-Cali/2000-009, ANTARES internal note.*